Old Dominion University

ODU Digital Commons

Mechanical & Aerospace Engineering Theses & Dissertations

Mechanical & Aerospace Engineering

Summer 8-2023

Experimental and Computational Aerodynamic Studies of Axially-Oriented Low-Fineness-Ratio Cylinders

Forrest Miller
Old Dominion University, forrestmiller757@gmail.com

Follow this and additional works at: https://digitalcommons.odu.edu/mae_etds

 Part of the Aerodynamics and Fluid Mechanics Commons, Engineering Physics Commons, and the Statistical, Nonlinear, and Soft Matter Physics Commons

Recommended Citation

Miller, Forrest. "Experimental and Computational Aerodynamic Studies of Axially-Oriented Low-Fineness-Ratio Cylinders" (2023). Master of Science (MS), Thesis, Mechanical & Aerospace Engineering, Old Dominion University, DOI: 10.25777/r4f6-ta04
https://digitalcommons.odu.edu/mae_etds/369

This Thesis is brought to you for free and open access by the Mechanical & Aerospace Engineering at ODU Digital Commons. It has been accepted for inclusion in Mechanical & Aerospace Engineering Theses & Dissertations by an authorized administrator of ODU Digital Commons. For more information, please contact digitalcommons@odu.edu.

EXPERIMENTAL AND COMPUTATIONAL AERODYNAMIC STUDIES OF AXIALLY-ORIENTED LOW-FINENESS-RATIO CYLINDERS

by

Forrest Miller
B.S. Physics August 2018, Old Dominion University
B.S. Mechanical Engineering August 2018, Old Dominion University

A Thesis Submitted to the Faculty of
Old Dominion University in Partial Fulfillment of the
Requirements for the Degree of

MASTER OF SCIENCE

AEROSPACE ENGINEERING

OLD DOMINION UNIVERSITY
August 2023

Approved by:

Colin P Britcher (Director)

Orlando Ayala (Member)

Drew Landman (Member)

ABSTRACT

EXPERIMENTAL AND COMPUTATIONAL AERODYNAMIC STUDIES OF AXIALLY-ORIENTED LOW-FINENESS-RATIO CYLINDERS

Forrest Miller
Old Dominion University, 2023
Director: Dr. Colin P Britcher

For the successful completion of atmospheric entry, descent, and landing (EDL) missions, a body geometry must be selected which provides favorable dynamic aerodynamic properties. The types of experimental facilities capable of collecting information on these properties are limited; however, their numbers are growing thanks to the continued work by the aerodynamics community. NASA Langley Research Center (LaRC) is conducting dynamic aerodynamic testing using a subsonic magnetic suspension and balance system (MSBS), with the end goal of implementing a supersonic MSBS facility at NASA Glenn Research Center. MSBSs are also currently used at the Institute of Fluid Science (IFS) at Tohoku University in Japan for blunt body testing. With the MSBS community growing, there is an opportunity for collaboration in overlapping areas of interests, particularly in expanding general blunt body theory and estimating EDL vehicle performance using these modern facilities.

The work encompassed in this thesis is a product of such a collaboration, with the specific subject of examination being an axially-oriented low-fineness-ratio cylinder. This geometry which has been previously tested at the IFS facility in Japan, was used as the basis for a multi-faceted campaign at the NASA LaRC MSBS, the Old Dominion University (ODU) low-speed wind tunnel, and computational fluid dynamic (CFD) simulations on the ODU high-performance computing cluster (HPC). Static tests were performed at the ODU wind tunnel on a $6''$ diameter model and were accompanied by static CFD simulations. Dynamic testing was performed at the NASA LaRC MSBS facilities on two $1.75''$ diameter models with varied gravitational centers and were accompanied by a dynamic CFD simulation.

The experimental and computational goals were met, with results for static and dynamic aerodynamic forces as well as flow visualization being compared and contrasted. There was reasonable agreement between the static results with empirical data as well as the dynamic results. In particular, the agreements with empirical results for pitch angles from 0° to 90° stand as a significant validation to the scarce data that exists in this region.

Copyright, 2023, by Forrest Miller, All Rights Reserved.

Dedicated to rubber ducks, without whom the majority of this thesis would remain in my head.

ACKNOWLEDGMENTS

I am sincerely lucky to have been surrounded by supporting friends, family, peers, and mentors who have facilitated the culmination of work in this thesis. I would like to thank Dr. Colin Britcher, to whom I owe a great many teachings of science, patience, and perspective. Without your unwavering guidance, this work would not be possible. I would also like to thank the NASA MSBS team of Mark Schoenenberger, David Cox, and Timothy Schott who have continued to provide insight and knowledge which have helped me significantly, both with this work and with outside growth as an engineer. I want to give my thanks to my committee, Dr. Orlando Ayala and Dr. Drew Landman, for their time spent reviewing and providing critical improvements to this manuscript. I would also like to thank my sister LeAynne for giving me courage in times of doubt, and being my biggest fan from the day I was born. The person who deserves the most thanks would be Natalie Pham. Your kindness, truthfulness, support, and love have served as a continued reminder as to why I push forward. I will never be able to fully repay you for the amount of wonderful help you've given me, I can only hope to support you to the level of which you have supported me. Thank you all so very much.

NOMENCLATURE

α	Generalized Diffusive Coefficient
δ_{ij}	Kronecker Delta
$\dot{d}$	Diffusive Species Generation Term
$\dot{q}$	Heat Generation Term
$\frac{\partial}{\partial t}$	Partial Derivative with Respect to Time
$\frac{\partial}{\partial x_i}$	Partial Derivative with Respect to Distance in the i Direction
λ	Eigenvalue
μ	Viscosity
$\overrightarrow{\omega}$	Vorticity
Φ	Roll Rotational Axis
ϕ	Generalized Objective Function
Ψ	Yaw Rotational Axis
ρ	Air Density
σ_{ij}	Cauchy Stress Tensor
Θ	Pitch Rotational Axis
C	Diffusive Concentration
c	Chord
C_D	Aerodynamic Drag Coefficient
C_g	Center of Gravity
C_L	Aerodynamic Lift Coefficient
C_P	Coefficient of Pressure

C_p	Specific Heat at Constant Pressure
C_S	Aerodynamic Side Force Coefficient
D_{fr}	Fluid Region Diameter
D_m	Mass Diffusivity Coefficient
e_{ij}	Rate-of-Strain Tensor
e_{kk}	Trace of Rate-of-Strain Tensor
f	Fineness Ratio
g_i	Gravitational Acceleration
H	Enthalpy
K	Thermal Conductivity Coefficient
L_d	Fluid Region Length - Downstream from Model
L_u	Fluid Region Length - Upstream from Model
p	Air Pressure
S	Generalized Source Term
T	Temperature
u_i	Fluid Velocity in the i Direction
u_x	Axial Fluid Velocity
x	Drag Coordinate Axis
y	Side Coordinate Axis
$Y+$	Non-Dimensional Wall Distance
z	Lift Coordinate Axis

TABLE OF CONTENTS

LIST OF TABLES

LIST OF FIGURES

CHAPTER 1

INTRODUCTION

1.1 MOTIVATION

Every space mission which involves entry into a planetary body's atmosphere (including re-entering Earth's atmosphere) requires careful consideration of the geometry that will be used for this entry process. Whether the craft is manned or unmanned, safe entry, descent, and landing (EDL) is paramount for mission success. From aerodynamic stability to thermal dissipation, the study of all technical aspects of EDL vehicles has long been of interest by space agencies from around the world. A blunt body geometry was quickly determined to be the best for the entry process due to the large frontal surface area which slows the craft down quickly, and also counter-intuitively provided better heat dissipation than the spike geometries that were being examined at the time [2]. In the half-century since this discovery, blunt body craft have safely returned astronauts from orbit, landed rovers on Mars, and become a finely tuned tool for the space industry.

Even with countless instances of successful implementation, blunt body geometries inherently create aerodynamic complexities in the wake that make testing and theorizing flow structure problematic. This combined with the need for dynamic test data to properly characterize entry vehicle performance makes the search for improved testing, database development, and computational studies of blunt body geometry imperative. Experimentally, these geometries have been dynamically tested through ballistic range testing, forced and

free oscillation rigs in conventional wind tunnels, and spin tunnel testing in the past. Recently, there has been a push to develop a magnetic suspension and balance system (MSBS) for testing dynamic stability at low subsonic fluid velocities by NASA Langley Research Center (LaRC) in Hampton, Virginia [3]. This type of system allows for stingless force and moment measurement by levitating the model in a test section using high-powered electromagnets. MSBS facilities have been operated and explored in the subsonic flight regime at Princeton, the University of Virginia, and the Massachusetts Institute of Technology (MIT), as well as other universities and research centers, since the early 1960s [4, 5, 6]. At the Institute of Fluid Science (IFS) at Tohoku University in Japan, multiple state of the art MSBSs are currently being used to study the connection of aerodynamic forces and wake structure for axially-oriented cylinders [7]. The MSBS team at NASA LaRC is performing research and development using a subsonic MSBS tunnel, the end goal of which is to provide an improved test facility for which dynamic EDL vehicle data can be captured. The work discussed in this thesis is a result of a collaboration between the IFS team and the NASA LaRC team, to use the advanced MSBS test facilities available to bridge gaps in the connection of aerodynamic forces and wake structure interactions of blunt bodies.

1.2 OBJECTIVES

The work encompassed in this thesis revolves around a model that Tohoku University is examining in depth, a low-fineness-ratio cylinder. This geometry is being studied as an archetype of blunt bodies and as a highly simplified representation of EDL vehicles. By gaining insight into the flow structure and dynamics of this simplified model, it is hoped that knowledge can be gained of blunt body dynamics as a whole. The IFS's work has

primarily focused on studying fineness-ratio effects of these models on their aerodynamics [7, 8, 9], whereas this work is aimed at a specific fineness-ratio model at a wide range of angle of attack. It was hypothesized that there would be four distinct flow regimes that the model experiences in pitch from 0° to 90°. These regimes are displayed in Fig. 1, and are defined as follows.

1. 0° Pitch Angle. Full separation of flow symmetrically surrounding the cylinder.
2. ≈10° Pitch Angle. Local reattachment occurs on the windward side at the trailing edge.
3. ≈45° Pitch Angle. Full loss of windward separation region.
4. 90° Pitch Angle. Return of separation symmetry with flow becoming fully separated from the flat faces of the cylinder.

The goals of this thesis were to obtain empirical results for a cylinder model at both the ODU low speed wind tunnel, as well as the NASA 6″ MSBS wind tunnel. This effort was then to be accompanied by steady state and transient computational fluid dynamic (CFD) simulations of free-stream conditions, providing supplemental data points to the experimental data, increasing angle resolution across the quarter-rotation of pitch being studied. Initial CFD studies were also planned on tumbling models to correlate to levitated results from the MSBS at NASA LaRC.

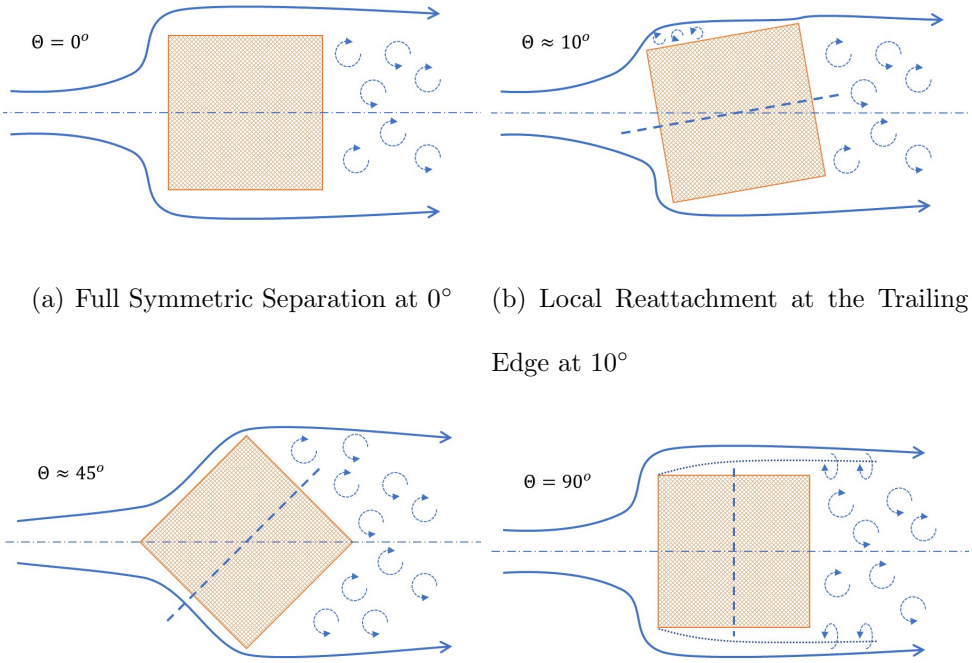

(a) Full Symmetric Separation at 0°

(b) Local Reattachment at the Trailing Edge at 10°

(c) No Separation on Windward Faces at 45°

(d) Full Symmetric Separation of Flat Faces at 90°

Fig. 1: Hypothesized Flow Regimes of a Pitching, $f = 1$ Cylinder

1.3 SCOPE AND ORGANIZATION OF THESIS

This thesis covers both experimental and computational theory, methodology, and results for the cylinder model. A background is discussed on aerodynamic conditions that define the problem of study, current MSBS technology, a brief discussion on turbulent CFD theory, and an explanation of the previous testing that has been performed on axially-oriented cylinders. Experimental and computational methodology are presented followed by the static and dynamic results. Lastly, the computational and experimental results are compared together and with empirical studies and then discussed at length.

CHAPTER 2

BACKGROUND

2.1 UNSTEADY AERODYNAMICS OF BLUNT BODIES

Reentry vehicles are required to safely traverse the atmosphere slowing from hypersonic speeds to low supersonic or subsonic prior to parachute deployment. The blunt body shape has been used as a reliable way to perform this atmospheric entry as well as to handle loads from drag and heating. The aerodynamics governing blunt bodies are quite different than that of streamline bodies. Drag forces are dominated by viscous components for streamlined bodies whereas blunt bodies are dominated by forces from pressures. Figure 2 shows conceptual subsonic flow regimes over a streamlined body at low angle of attack, a pitching streamlined body, and a Stardust capsule. The blunt body of the Stardust capsule creates a wake of separated flow leading to low pressure regions on the leeward (backshell) side of the vehicle producing drag. This phenomenon is one of the main reasons blunt bodies are used for atmospheric entry.

Even with blunt bodies' superior heat dissipation and high drag, they are subject to dynamic instabilities which need to be closely monitored throughout the design process. From empirical results, the effects of dynamic instabilities on mission performance are moderately well known; however, the underlying flow phenomena that causes these instabilities is still an area of interest in research. Connecting the dots between the base Newtonian mechanics

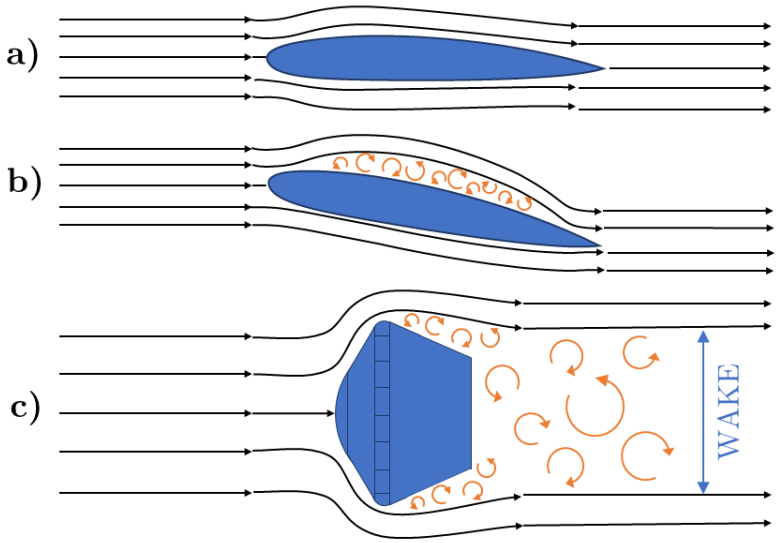

Fig. 2: Aerodynamic Flow and Separation of a) Streamlined Body, b) Pitching Streamlined Body, c) Blunt Body

that govern body motion and the fluid mechanics that dictate the flow changes in reaction to the blunt bodies presence remains an actively researched subject to this day.

The physical flow is governed by the Navier-Stokes equations which were developed in the mid-19th century. The most generalized form is shown below in Eq. 1.

$$\underbrace{\rho\frac{D\vec{v}}{Dt}}_{\mathbf{A}} = \underbrace{-\bigtriangledown p}_{\mathbf{B}} + \underbrace{\bigtriangledown \cdot T}_{\mathbf{C}} + \underbrace{\vec{F}}_{\mathbf{D}} \tag{1}$$

The partial differential equation defines the inertial forces (A) as equal to the summation of the volumetric stress tensor (B), stress deviator tensor (C), and external forces (D). The difficulty of this problem has led to an array of methods in approximating solutions to the equations, which is the basis for CFD. The more turbulent a particular CFD problem

the more difficult these approximations become to compute. The turbulence inherent in reentry vehicle aerodynamics, which span from hypersonic to subsonic flow in a single flight path, along with the dynamic requirements add to the problem's complexity. Reliable computationally-inexpensive solutions to these problems have been unachievable until quite recently.

Experimentally acquiring dynamic supersonic data has been no simple feat either. Six degree-of-freedom (DOF) simulations combined with ballistic range and spin tunnel testing have been used to validate dynamic stability of entry vehicle designs in the past; however, there are two areas of interest being pursued by NASA, MSBSs and 6-DOF CFD simulations.

2.2 MAGNETIC SUSPENSION AND BALANCE SYSTEMS

In order to experimentally test the dynamic stability of a new reentry vehicle design experimentally, the model cannot be supported in a traditional wind tunnel sting mounted setup. Ballistic range and spin tunnel testing allow for model motion to be obtained; however, provide limited data points in terms of flow speed. Magnetic suspension and balance systems allow for dynamic testing in ranges of flow conditions with cost effective repeatability of tests.

MSBSs use electromagnet fields to counteract gravitational and flow forces on the model, levitating it in the test section. This allows stingless data and motion to be captured during wind tunnel tests. MSBSs can be broken down into 4 main components; the electromagnet coil configuration, the position feedback system, the data acquisition system, and the wind tunnel.

The schematics for the joint ODU/NASA LaRC 6″ MSBS and wind tunnel are shown

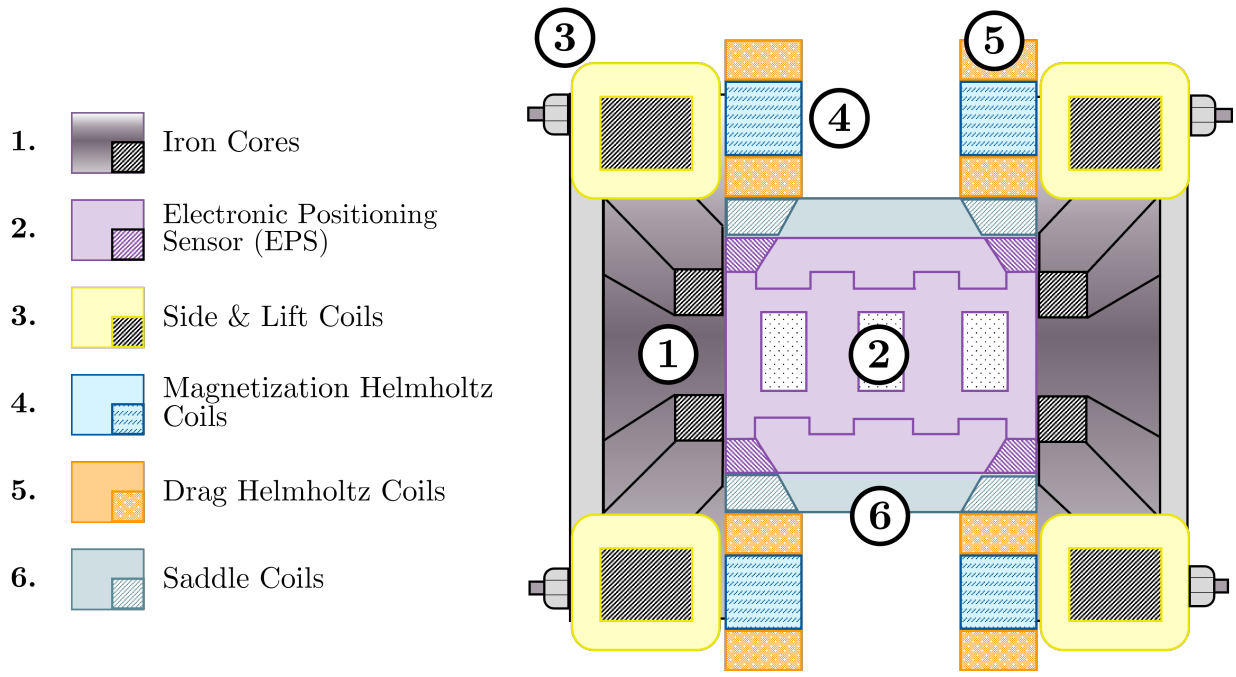

Fig. 3: Schematic of ODU/NASA LaRC 6″ MSBS

in Fig. 3 & Fig. 4 respectively. This MSBS was designed and built in the 1960s by MIT for use in the subsonic and supersonic flow regime. Currently, the coil configuration has been reconfigured as a proof of concept for a supersonic version to be built and implemented at NASA Glenn Research Center [3]. One of the most modern MSBSs in the world is the 1-m MSBS at the Institute of Fluid Science, Tohoku University which has a 1-m wide octagonal test section. Comparisons between the design of this system and the NASA LaRC system will be examined in the following sections which define the 3 main subsystems of a MSBS.

2.2.1 ELECTROMAGNET COIL SYSTEM

Around the outside of the wind tunnel test section, an electromagnet coil system creates a magnetic field that levitates the model being tested. The orientation of coils is designed

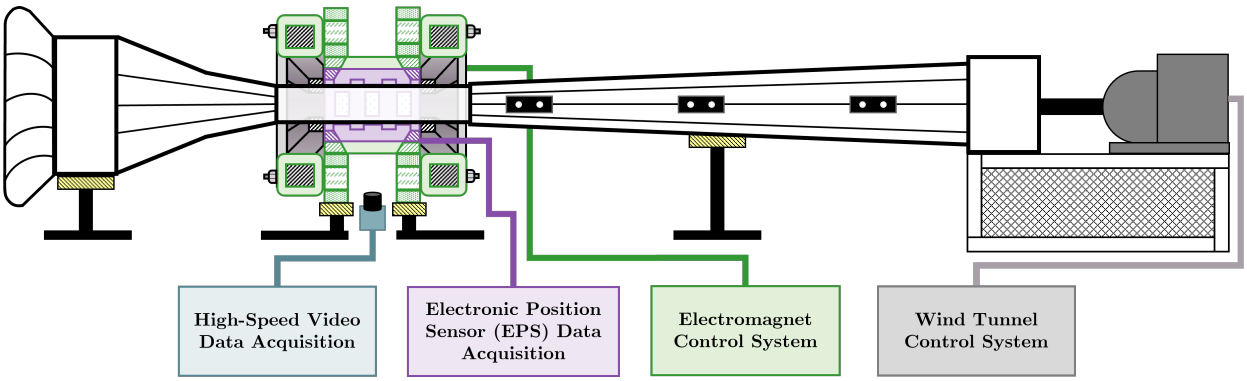

Fig. 4: Schematic of Wind Tunnel Accompanying ODU/NASA LaRC 6″ MSBS

differently for each MSBS setup; however, they all have similar goals, to create a magnetic field around a magnetic or magnetically cored model that can counteract aerodynamic and gravitational forces. Which of these forces are controlled versus left free to effect the motion of the model dictates what dynamic motion can be studied by that particular MSBS. Too many constraints would leave no dynamic information to be pulled from the tests and if there are too few or loosely constrained motions then the model will lose control and be forced down the tunnel. It is for this reason that MSBS designs are usually collaborative efforts between control, aerospace, and electrical engineers.

The NASA LaRC 6″ MSBS system incorporates 3 pairs of coils; Side & Lift coils, Helmholtz coils, and Saddle coils as shown in Fig. 3. An added benefit of the MSBS design is that by controlling 1-DOF via magnetic field, one can calculate the force being exerted on the model in that direction.

2.2.2 POSITION FEEDBACK SYSTEM

In order to control the forces on the model, the system must be able to obtain instantaneous information regarding the position and angle of the model. This is a challenging problem, as with no sting to provide access for computer connections and sensors all data most be measured externally. The NASA LaRC MSBS uses an electronic positioning sensor (EPS) which was designed and built with the system by MIT in the 1960s. The EPS, labeled in the original schematics (Fig. 3) "Position Sensor Coil", sits between the electromagnet coils and the test section and works similarly to a linear variable differential transformer (LVDT).

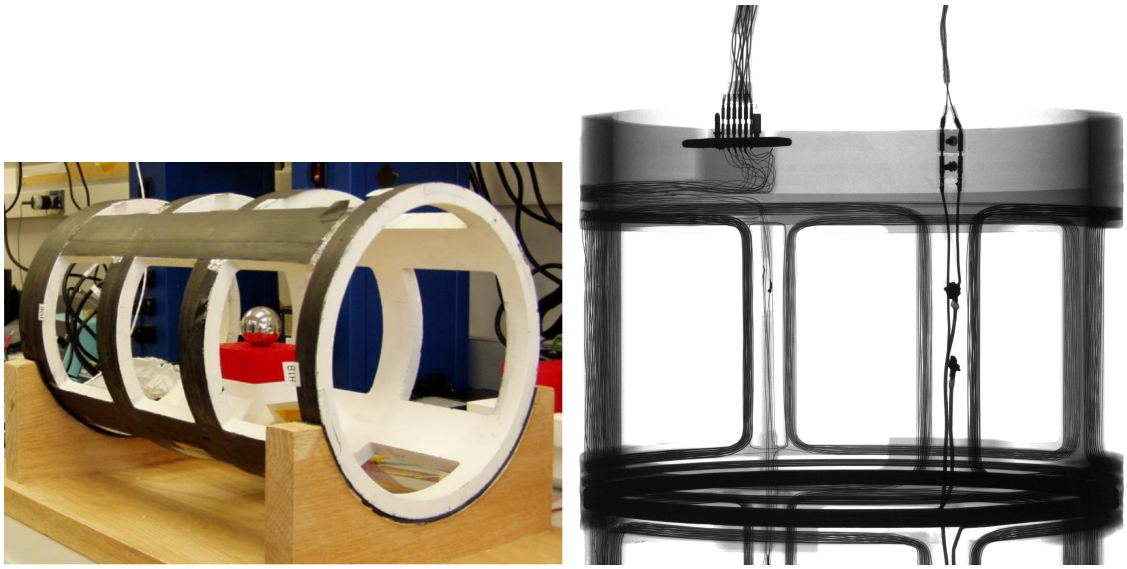

(a) Exterior View of EPS (b) X-Ray View of EPS

Fig. 5: NASA LaRC MSBS EPS, External and X-Ray Views

The EPS is a cylindrical phenolic tube with machined channels for coil windings. These windings were epoxied in place during fabrication and are not visible in an external view.

An external and X-ray view of the sensor "cage" is shown in Fig. 5. The EPS internal wiring consists of excitation, pitch, axial, vertical position, yaw, and lateral position coils which originally allowed for 5-DOF operation. When a magnetic object, either a metal object magnetized by the MSBS or a permanent magnet, is placed inside the EPS, the object's magnetic flux is coupled to the coils within the sensor cage. Despite being constructed and designed over 50 years ago, the EPS is still in use, albeit with updated signal conditioning electronics, due to its ingenious design and functionality when paired with the MSBS at NASA LaRC [10].

There are other options for position feedback for controlling the levitating model with a good example of an alternative coming from the Tohoku University 1-m MSBS. Tohoku uses an optical approach, with charge-coupled device (CCD) line sensors and red and blue LEDs that illuminate the side and top of the model respectively. Utilizing 5 CCD cameras, the 1-m MSBS can support 5-DOF levitation and control [7]. The CCD cameras are configured at Tohoku with a 1.25kHz scan rate, and while the NASA LaRC EPS has a carrier frequency of 20kHz, it is closer to 1kHz once filtering takes place.

2.2.3 DATA ACQUISITION SYSTEM

Position and angle, force and moment, as well as tunnel speed and pressure are all essential to piecing together the aerodynamic results from a wind tunnel experiment. For a static wind tunnel test some of these measurements might be considered simple to obtain; however, for MSBSs this information is derived through a complex combination of systems and components.

At the NASA LaRC MSBS tunnel force and moment data is calculated directly from the

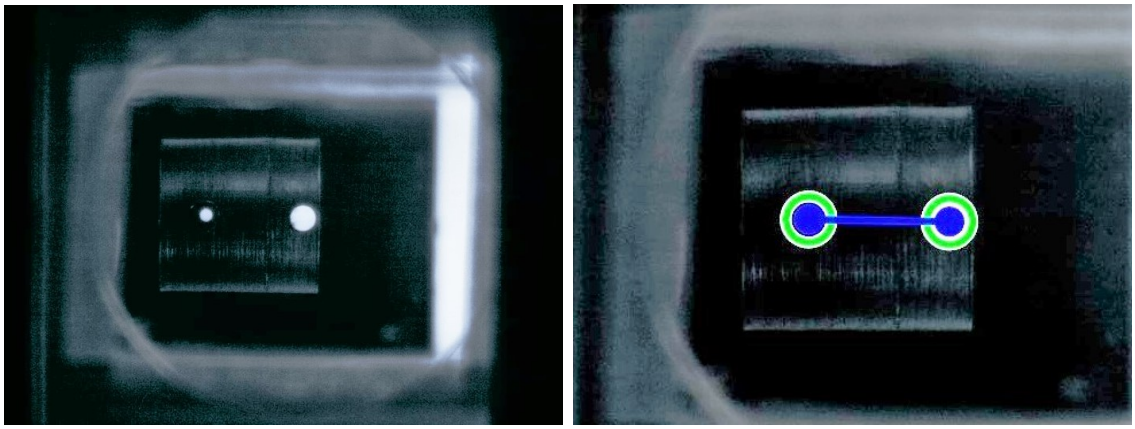

(a) Live View of Model Tracking Camera (b) Postprocessed Dot Tracking Performed in MATLAB

Fig. 6: NASA LaRC Camera System Demonstrated on Axially-Oriented Cylinder

raw coil currents required to keep the model in position. Wind tunnel speed and pressure are collected through a National Instruments (NI) LabVIEW program that controls the speed of the wind tunnel motor and reads tunnel conditions from pressure transducers and a thermocouple. Angle of attack could be measured through the EPS with a specifically cored model; however, the free-to-pitch setup of the system at the time of testing negated this possibility. Instead, an externally mounted Edgertronic camera system is used to track dots placed forward and aft of the models center as shown in Fig. 6. The camera is mounted below the MSBS facing upwards and captures rotation in the aerodynamic pitch direction of the model. The Edgertronic camera is setup for 180 frames per second allowing for up to 90Hz oscillatory frequency of the model. Data from the electromagnet, wind tunnel, and camera subsystems are synchronized in MATLAB to ensure analysis time clarity of experiment runs.

Tohoku University MSBS tunnel's CCD line camera subsystem simultaneously measures position and angle of attack. This removes the need of an additional system to get a full data set during runs. The small test section size of the NASA LaRC MSBS which causes a small maximum model size also leads to another issue that the 1-m MSBS does not run into, which is the lack of model surface pressures. The Tohoku 1-m MSBS has models up to 8.9 inches in diameter for a blockage ratio of 10% whereas the NASA LaRC tunnel is maximum of 2.1 inches in diameter for a blockage ratio of 10%. These size limitations combined with the internal material limitations of LaRC's EPS remove the possibility of telemetry systems to transfer the pressure data from the model to the external system. The Tohoku tunnel can use telemetry systems in the levitating models to collect and transmit base pressure measurements from runs.

2.3 COMPUTATIONAL BLUNT BODY AERODYNAMICS

CFD codes have different abilities in what physical properties of a problem can be simulated. This disparity in computational ability originates from the limitations of the mathematical solver that the program encompasses. By making assumptions about the problem, the simulation becomes easier to run; however, it may lose physical accuracy. The balancing act of ensuring appropriateness of assumptions without losing realism is the heart of the numerical method selection. The general conservation equations that are used to model the fluid flow will be briefly discussed followed by the details of the two turbulence modeling methods chosen.

2.3.1 CONSERVATION EQUATIONS

The physical flow is simulated by solving a set of conservation equations that are standard across CFD programs; only varying by notation and discretization method. These equations are the the Navier-Stokes form of the momentum equation, the continuity equation, the conservation of energy equation, and the conservation of diffusive species equation. These conservation laws are altogether referred to as the Navier-Stokes equation system and each take the general form similar to the equation below.

$$\frac{\partial \phi}{\partial t} + \frac{\partial \phi u_j}{\partial x_j} = \frac{\partial}{\partial x_j} \alpha \frac{\partial \phi}{\partial x_j} + S \tag{2}$$

Here, ϕ is an unknown function that is being solved for and is related to a first-order advection term ($\partial \phi u_j / \partial x_j$), a second-order diffusion term ($\partial / \partial x_j \ \alpha \ \partial \phi / \partial x_j$), and a source term S. This general form is used to describe the Navier-Stokes equation system that is used by scFLOW's solver [11] starting with the continuity equation.

The continuity equation (or conservation of mass equation) defines the governing relation that any change in density in a fluid will result in a change in mass flow rate over that control volume. The general equation (Eq. 3a) defines that any change in density over time (term A) will have to be met with an equal and opposite change in mass flow over the volume (term B). For incompressible flow, density is assumed to be constant thereby simplifying the continuity equation into Eq. 3b.

$$\underbrace{\frac{\partial \rho}{\partial t}}_{\mathbf{A}} + \underbrace{\frac{\partial}{\partial x_i}\rho u_i}_{\mathbf{B}} = 0 \tag{3a}$$

$$\frac{\partial u_i}{\partial x_i} = 0 \tag{3b}$$

The general form of the conservation of energy equation is displayed in Eq. 4a. This equation is based on the balance of energy in a control volume with the application of Gauss's integration theorem and Fourier's law. Term A is the change in energy over the control volume per unit time and term B is the energy flowing into the control surfaces. These terms are represented in their enthalpy form here in accordance with scFLOW notation. Terms C and D are byproducts of the relation of enthalpy to the internal energy of the fluid. Term D is the work done by stress acting on control surfaces. Term F is the thermal energy change over the control surface in relation to the thermal conductivity (assumed isotropic) and temperature gradient based on Fourier's Law. The final term in Eq. 4a is the heat generation term.

The incompressibility assumption dictates that the problem is of low-Mach number. At low-Mach number the magnitude of terms C, D, and E are negligible when compared to the remaining terms. This assumption results in Eq. 4b.

$$\underbrace{\frac{\partial \rho H}{\partial t}}_{\mathbf{A}} + \underbrace{\frac{\partial u_j \rho H}{\partial x_j}}_{\mathbf{B}} = \underbrace{\frac{\partial p}{\partial t}}_{\mathbf{C}} + \underbrace{\frac{\partial u_j p}{\partial x_j}}_{\mathbf{D}} + \underbrace{\sigma_{ij}\frac{\partial u_i}{\partial x_j}}_{\mathbf{E}} + \underbrace{\frac{\partial}{\partial x_j}K\frac{\partial T}{\partial x_j}}_{\mathbf{F}} + \underbrace{\dot{q}}_{\mathbf{G}} \tag{4a}$$

$$\frac{\partial \rho C_p T}{\partial t} + \frac{\partial u_j \rho C_p T}{\partial x_j} = \frac{\partial}{\partial x_j}K\frac{\partial T}{\partial x_j} + \dot{q} \tag{4b}$$

The diffusive species conservation equation is a special case of the convection-diffusion equation with zero advective flux. The general form of this equation for a compressible flow is shown above in Eq. 5a. Here the increases of diffusive species (term A) and the diffusive species flowing into the control surface (term B) is equal to the sum of diffusive species flux due to a diffusive concentration gradient (term C) and any generation of diffusive species (term D). Incompressible flow eliminates the need for density considerations; however, does not remove any terms.

$$\underbrace{\frac{\partial \rho C}{\partial t}}_{\mathbf{A}} + \underbrace{\frac{\partial \rho u_j C}{\partial x_j}}_{\mathbf{B}} = \underbrace{\frac{\partial}{\partial x_j} \rho D_m \frac{\partial C}{\partial x_j}}_{\mathbf{C}} + \underbrace{\rho \dot{d}}_{\mathbf{D}} \tag{5a}$$

$$\frac{\partial C}{\partial t} + \frac{\partial u_j C}{\partial x_j} = \frac{\partial}{\partial x_j} D_m \frac{\partial C}{\partial x_j} + \dot{d} \tag{5b}$$

The Navier-Stokes momentum equation will be discussed in more detail than the other conservation laws as it is essential for context to the turbulence models that were chosen for this study. Equation 6a is the general compressible form of the Navier-Stokes equation. This equation relates the inertial forces (term A), the volumetric stress (term B), the stress deviator tensor (term C), and the external forces (term D).

$$\underbrace{\frac{\partial \rho u_i}{\partial t}}_{\mathbf{A}} + \underbrace{\frac{\partial u_j \rho u_i}{\partial x_j}}_{\mathbf{B}} = \underbrace{\frac{\partial \sigma_{ij}}{\partial x_j}}_{\mathbf{C}} + \underbrace{\rho g_i}_{\mathbf{D}} \tag{6a}$$

where

$$\sigma_{ij} = (-p + \lambda e_{kk})\delta_{ij} + 2\mu e_{ij} \tag{6b}$$

$$e_{ij} = \frac{1}{2}\left(\frac{\partial u_i}{\partial x_j} + \frac{\partial u_j}{\partial x_i}\right) \tag{6c}$$

The general Navier-Stokes momentum equation (Eq. 6a) along with the other Navier-Stoke equations require an appropriate turbulence model on a discretized grid for closure. Two methods of turbulence modeling were used in this work, Large-Eddy Simulation (LES) and the Reynold's Averaged Navier Stokes (RANS) k-ϵ model. Comparisons between the efficient RANS method and the generally more accurate but computationally expensive LES model have been made for blunt bodies in the past [12]. These turbulence modeling methods will be discussed in the following sections.

2.3.2 REYNOLDS-AVERAGED NAVIER-STOKES METHOD

Rather than try to resolve small eddies and vortices in the flow, the RANS method uses averaged values to increase process efficiency and solve for the mean flow field. This method is effective for calculating fluid problems where the mean flow is of interest or problems with low-temporal unsteadiness. The Reynolds equation is defined below by incorporating time-averaged values and fluctation measurements (denoted by $^{-}$ and $^{'}$ respectively and demonstrated in Eq. 7) into the general Navier-Stokes equation shown in Eq. 6a.

$$u_i = \bar{u_i} + u_i^{'} \tag{7}$$

$$\frac{\partial \bar{\rho}\bar{u_i}}{\partial t} + \frac{\partial \bar{u_j}\bar{\rho}\bar{u_i}}{\partial x_j} = \frac{\partial}{\partial x_j}(\overline{\sigma_{ij}} - \bar{\rho}\overline{u_i^{'}u_j^{'}}) + \bar{\rho}g_i \tag{8}$$

The temporal mean is incorporated into the velocity, density, and stress components from Eq.6a, and there is a new term introduced ($-\bar{\rho}\overline{u_i' u_j'}$) which is known as the Reynolds shear stress. This term is the stress produced by the turbulence of the flow and is the mean of the product of the x and y instantaneous velocity fluctuations multiplied by the time-averaged density. The other conservation equations follow a similar procedure of temporal averaging and isolation of the turbulent components of energy and diffusive species. These equations form the RANS equations and can be discretized and solved once a method of dealing with the Reynold's Stress term is chosen. The RANS solutions discussed in this work incorporated the shear-stress transport (SST) k-ϵ method of dealing with the Reynold's stress using standard coefficients in scFLOW [11].

2.3.3 LARGE EDDY SIMULATION

Unlike the RANS model, the LES model is required to be time-dependent in order to solve for turbulence. The LES method calculates eddies that the RANS solution would not be able to properly represent. In order to keep process times reasonable a filter is set when configuring the LES solver. The purpose of the filter is to decide what size eddies are resolved in the flow and which are estimated. A finer filter will take more computation time but provide a more accurate result. LES is typically applied to cases that have high unsteadiness such as blunt bodies or turbomachinery. The LES equations use a convolutional kernal spacial filter which will be denoted using a $\tilde{}$ to eliminate confusion with the time averaged RANS equations.

$$\widetilde{u+u} = \tilde{u} + \tilde{u} \tag{9a}$$

$$\widetilde{\frac{\partial u}{\partial x}} = \frac{\partial \tilde{u}}{\partial x} \tag{9b}$$

$$\widetilde{ux} = \tilde{u}\tilde{x} \tag{9c}$$

$$\frac{\partial \rho \tilde{u}_i}{\partial t} + \frac{\partial \tilde{u}_j \rho \tilde{u}_i}{\partial x_j} = \frac{\partial}{\partial x_j}[\mu(\frac{\partial \tilde{u}_i}{\partial x_j} + \frac{\partial \tilde{u}_j}{\partial x_i}) - \rho(\widetilde{u_i u_j} - \tilde{u}_i \tilde{u}_j)] \tag{10}$$

The nonlinear term ($\widetilde{u_i u_j}$) must be solved for using an approximation model (turbulence-model). ScFLOW uses subgrid-scaling (SGS) models to complete the LES calculations, the one of which was used in this work was the Wall-Adapting Local Eddy-viscosity model (WALE).

2.4 PREVIOUS STUDIES OF LOW-FINENESS-RATIO CYLINDERS

The motivation for this work's focus on the low-fineness-ratio cylinder was described in Section 1.1; however, there have been previous studies on similar geometries over the past century or more with a wide variety of motivations. Cylindrical geometries are some of the most classical when it comes to aerodynamic studies, particularly when oriented laterally. This is in part due to the ability to observe flow separation without the consideration of end effects (for large enough fineness ratio) [13]. Moving away from circular geometries to non-symmetric cylinders allowed the growth of flow separation knowledge and the verification of 2-D flow approximations to take place [14].

While the laterally-oriented cylinders were widely studied, experiments on axially-oriented

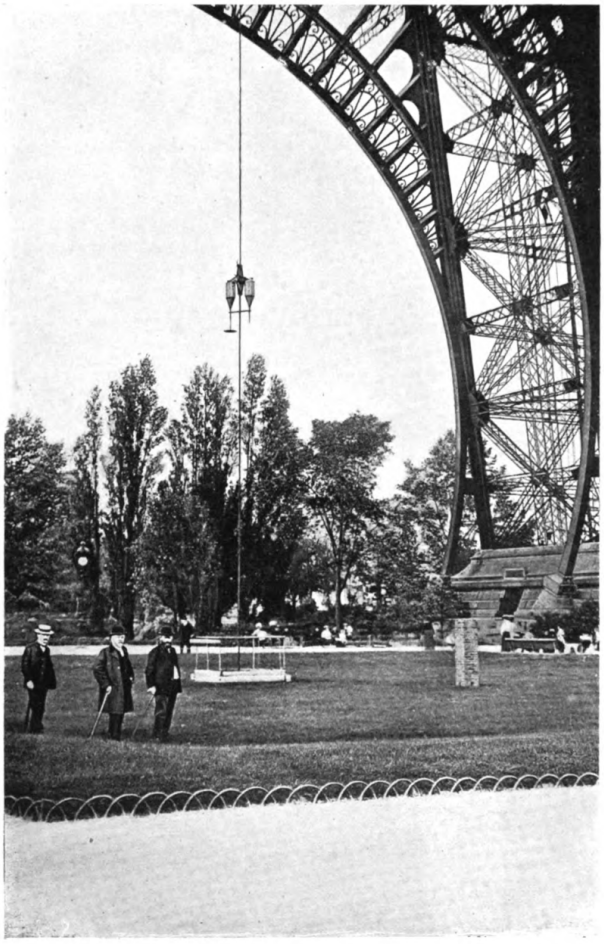

Fig. 7: Photo of Eiffel Tower Aerodynamic Drop Testing Apparatus Circa 1906 [1]

cylinders were not as common. The additional complexities of end-piece, fineness-ratio, and sting-support effects made these models less enticing to study. One of the first aerodynamic studies of many blunt body geometries, including the axially-oriented cylinder, was performed in the early 20th Century by Eiffel [1]. Drop testing was performed from the Eiffel Tower (shown in Fig. 7), the results of which are still referenced to this day.

The axially-oriented cylinder was not regularly explored until advances in test apparatus and viscous flow theory were made, with a resurgence in testing occurring in the late 1950s.

Dynamic stability of axially-oriented cylinders of fineness ratio 2.56 and 4.0 were tested at the Langley Pilotless Aircraft Research Station at Wallops Island, VA in 1957 [15]. In the mid 1960s, additional testing was performed on the reentry characteristics of these models, motivated by the necessity of determining aerodynamic effects on space nuclear power supplies [16, 17]. Starting in the late 1960s, interest in the complex flow surrounding axially-oriented circular cylinders started in support of energy harvesting optimization [18]. This study began the modern era of the cylinder studies, improving testing capabilities to classify the complex flow characteristics of these models [19]. This work is in support of adding useful aerodynamic data into this long history of the axially-oriented circular cylinder.

CHAPTER 3

EXPERIMENTAL METHODOLOGY

This chapter describes the experimental methods used to obtain static and dynamic results. The reference frame for all data and calculations is defined and described visually in Fig. 8. The axial (x), side (y), and lift (z) directions as well as the pitch (Θ), yaw (Ψ), and roll (Φ) rotational frames are explicitly defined in this figure.

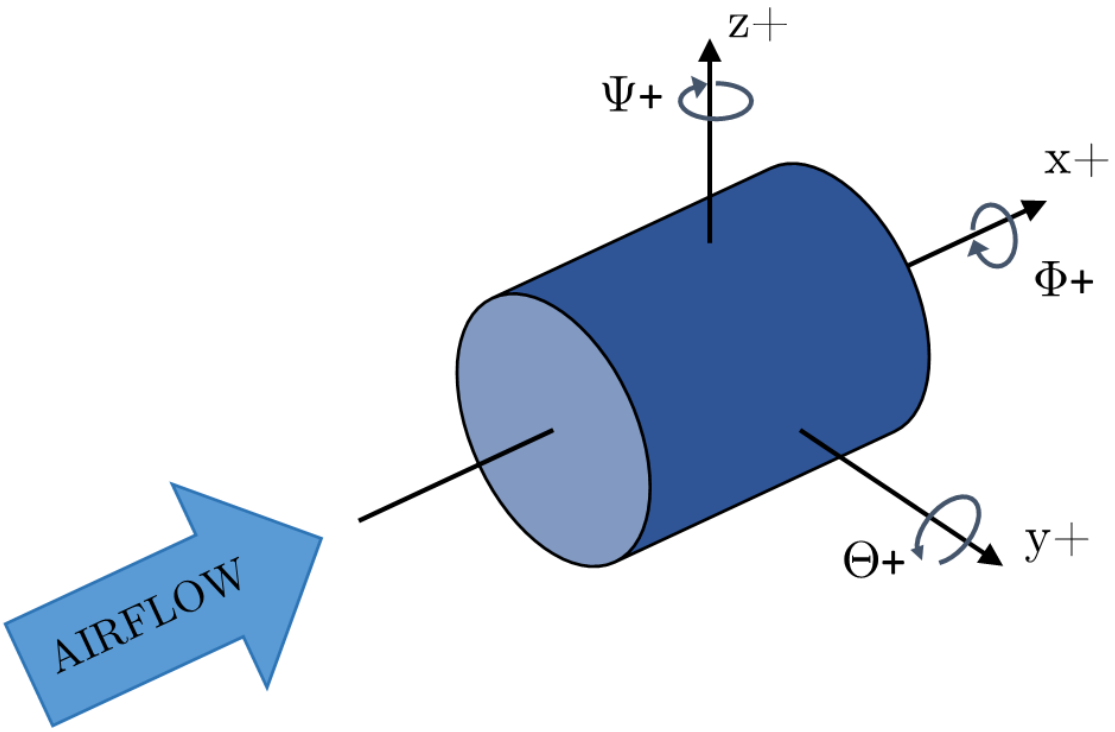

Fig. 8: Visual Definition of the Reference Frame for This Work

3.1 ODU LOW-SPEED WIND TUNNEL

Static aerodynamic tests were performed at the ODU subsonic wind tunnel to collect flow structure, force, moment, and pressure data. The acquisition of these data sets was completed in three phases.

1. Initial prototype design and testing with flow visualization.

2. Design iteration and improvements based on information gleaned from prototype tests.

3. Final testing with force, moment, pressure, and flow visualization data collection.

An initial prototype stand and cylinder body was designed, fabricated, and tested for exploratory flow visualization. The scope of this prototype testing was limited to quantitative velocity fields and flow visualization using PIV. The postulate that there are four distinct flow regimes at distinct pitch angles was challenged initially without the added complexities of surface pressure taps and free-coupling to a force sensor. This design as well as all subsequent computer-aided designs were created in Dassault Systèmes Catia V5 software. The body was made from 6″ diameter by 6″ long aluminum pipe, with end caps machined from aluminum plate. Internal cross supports secured the model closed and threaded into the stand's support rod, which fed through a streamlined tube to the stand base. This base was fixed below the wind tunnel to a through-pin pitch angle guide with discrete positions in increments of 5° from 0° to 30°. The concept would be to require minimal reassembly between pitch-angle changes and allow the focus of setup to be on the PIV operation. The computer generated model as well as the fabricated model are shown in Fig. 9.

The model was installed in the ODU wind tunnel and testing began at 15m/s. While the

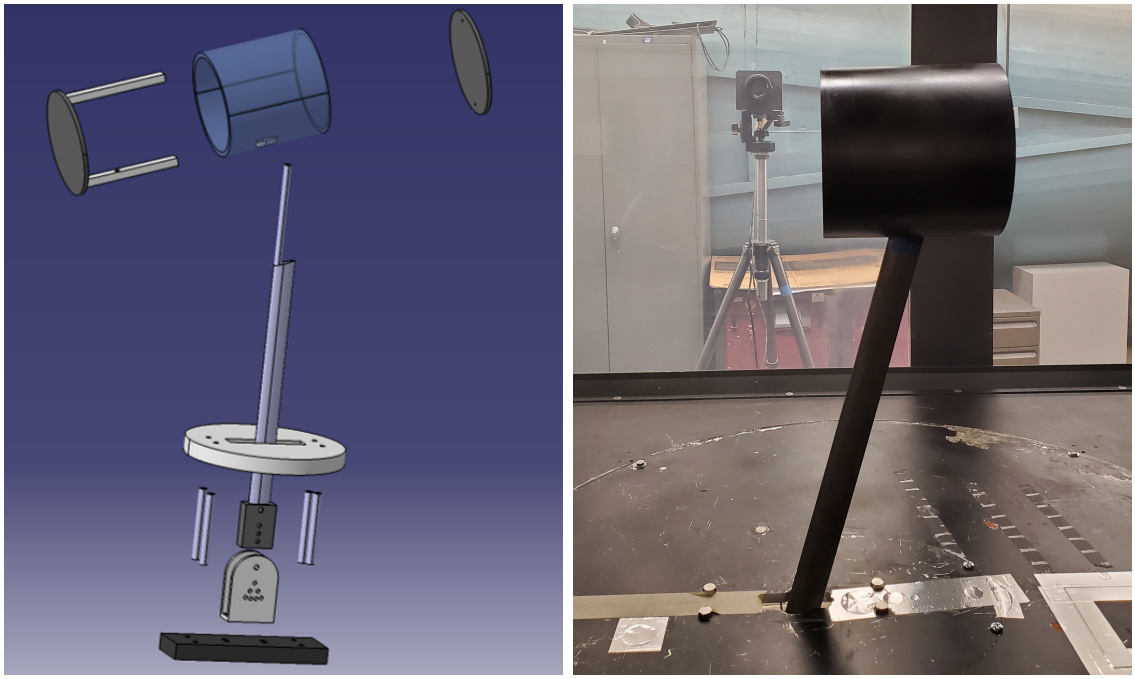

(a) Catia V5 Prototype Cylinder Model (b) Fabricated Cylinder Model

Fig. 9: Computer Aided Design (CAD) and Fabricated Prototype Cylinder Model and Stand

model required little reassembly between runs, there were some complications which limited the first batch of results. First, the matte paint chosen to coat the aluminum cylinder was glossier than anticipated, providing extra difficulties with laser alignment during the PIV calibration process. Second, while time was saved from assembly between pitch changes, by having the model move significantly in the tunnels height and flow axis the PIV camera alignment needed to be fully readjusted. If the model was kept relatively close to the same position in the tunnel only slight adjustments to the PIV camera's position would be required allowing a significant amount of troublesome fine-tuning to be avoided. Lastly, the through-hole discrete selection design of the stand functioned as designed but was not as stiff as expected. This combined with the weight of the aluminum shell resulted in non-trivial

amounts of vibrations occurring to the blunt body at speeds higher than 15m/s.

Time limitations for the exploratory runs combined with extra PIV calibration steps limited results with this model to 0° and 10° angle-of-attack. These results did provide confirmation of the separation region reattachment on the model's trailing edge occurring at approximately 10°, as well as useful insights into the proper priorities for the next design iteration.

The model underwent iterations of design to incorporate force and pressure data acquisition as well as the following insights from the prototype tests.

- Less-glossy finish to limit laser reflections.
- Minimizing the movement relative to the center-line of the tunnel to limit alignment time for PIV.
- Lower model weight and increase stand stiffness to reduce vibrations.

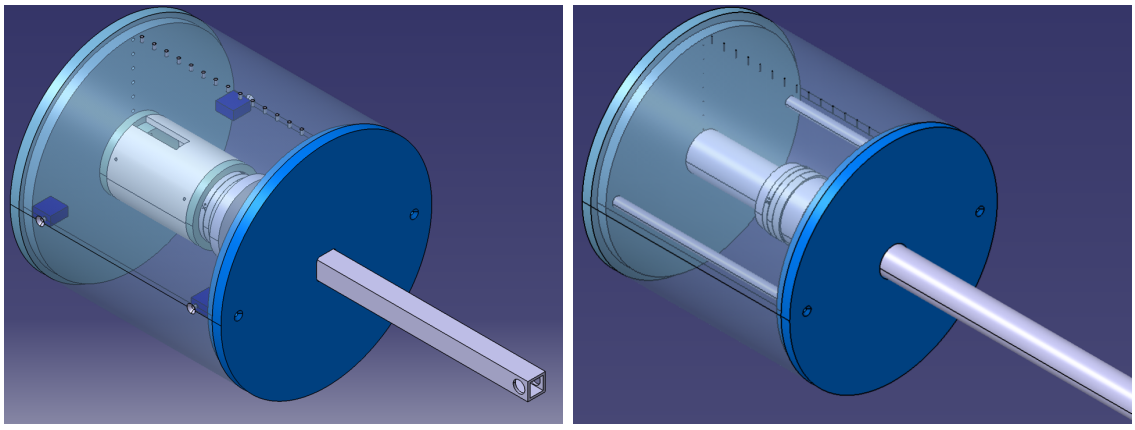

(a) Catia V5 Updated Model Concept (b) Catia V5 Updated Model Final Version

Fig. 10: Concept and Final CAD Cylinder Model Designs

The final design, shown in Fig. 10(b), incorporates mainly plastic or composite materials to lower the model's weight. A rear sting fits contact-free through the model-base allowing aerodynamic forces to be properly distributed onto the internal force and moment sensor. Pressure taps were incorporated onto the front and top surfaces of the model. The materials as well as components shape and size were designed to minimize manufacturing time and cost.

The stand and angle of attack selection mechanism were also redesigned to increase rigidity and improve angle variation. The updated stand attached to a Stewart platform which has been used for aerodynamic testing on drones in the tunnel [20]. The Stewart platform has fine-tuned angle and position capabilities, but lacks the range we needed in pitch that is desired to be observed. To combat this, a system of angled iron pipe connectors were configured and designed into the sting to allow the platform's fine angle adjustment to be centered around 0°, 45°, and 90°. These 3 fixture configurations are displayed in Fig. 11 along with the Stewart platform in Fig. 11(a). The pipe fitting connections not only provided the sturdy base for the model and a simple pitch changing mechanism, but also allowed for pressure tubing to be fed through the inside and out of the tunnel without being exposed to flow.

The test matrix outlining this set of subsonic tests at the ODU wind tunnel are shown in Table 1. In order to keep oil particles created for PIV from clogging the pressure taps, PIV runs were separated from force and pressure tests and the taps were covered when oil smoke was in the flow. A dummy-model of the force and moment sensor was also designed, fabricated, and installed to prevent limiting the availability of the sensor to other

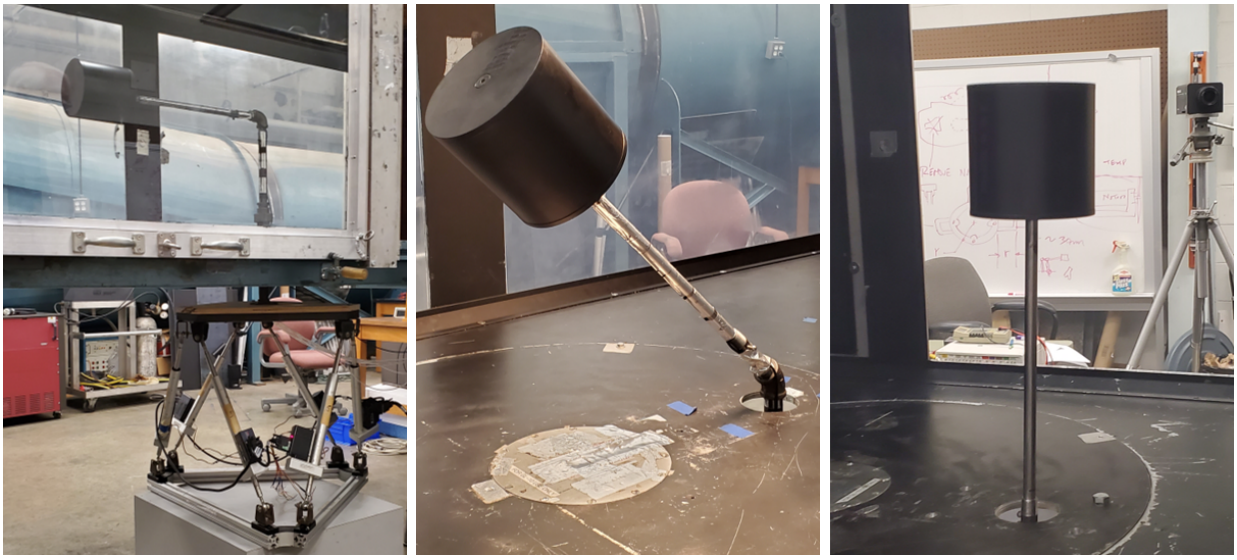

(a) 0° Pitch Angle Fixture with Stewart Platform

(b) 45° Pitch Angle Fixture

(c) 90° Pitch Angle Fixture

Fig. 11: Three Core Stand Configurations Mounted in the ODU Wind Tunnel

experimentalists. Considering the time intensive nature of the PIV calibration and data collection process, data points were strategically selected to ensure the capture of data points that would test the hypothesis while remaining mindful of time constraints. The force and pressure data sets had lower collection time costs thus allowing for a finer resolution of pitch angles around the loci of interest.

PIV tests were conducted first, starting with 0° and ascending in pitch angle to 90°. Each angle was intended to first be run at 15m/s and then 30m/s; however, at 10° pitch, vibrations perturbed the model significantly at velocities higher than 15m/s so this data point was omitted. For both the 0° and 10° pitch configurations, an additional data set of a detailed view in flow visualizations was acquired, the hope of which was to ensure capture

TABLE 1: Test Matrix for Subsonic Wind Tunnel Runs

	-10°	-5°	0°	5°	10°	35°	40°	45°	50°	55°	80°	85°	90°
0-30m/s Force	**X**	**X**	**X**	**X**	**X**	**X**	**X**	**X**	**X**	**X**	**X**	**X**	**X**
0-30m/s Pressure	**X**	**X**	**X**	**X**	**X**	**X**	**X**	**X**	**X**	**X**	**X**	**X**	**X**
15m/s PIV Wide			**X**		**X**			**X**					**X**
15m/s PIV Zoomed			**X**		**X**								
30m/s PIV Wide			**X**					**X**					**X**
30m/s PIV Zoomed			**X**										

of a fully separated flow and a trailing edge reattachment for 0° and 10° angle of attack respectively.

The PIV setup of the ODU subsonic wind tunnel is illustrated in Fig. 12. The model (Fig. 12-5) was mounted on the Stewart platform (Fig. 12-2) as previously described and aligned to the centerline of the tunnel. A New Wave Solo PIV Laser (Fig. 12-4) and power supply (Fig. 12-3) were mounted atop the tunnel and aligned so that the fan laser sheet is coincident with the model and tunnel's centerline. Perpendicular to this plane, outside of the tunnel a TSI PIVCAM 13-8 digital CCD camera (Fig. 12-6) was positioned for flow visualization capture. The tunnel's windows were covered to limit light interference and a MDG MAX 3000 fog generator (Fig. 12-1) pumped oil particles into the flow for illumination.

For each pitch angle investigated, the model needed to be re-aligned with both the tunnel and laser sheet. The camera was then finely focused into the plane of illumination using a

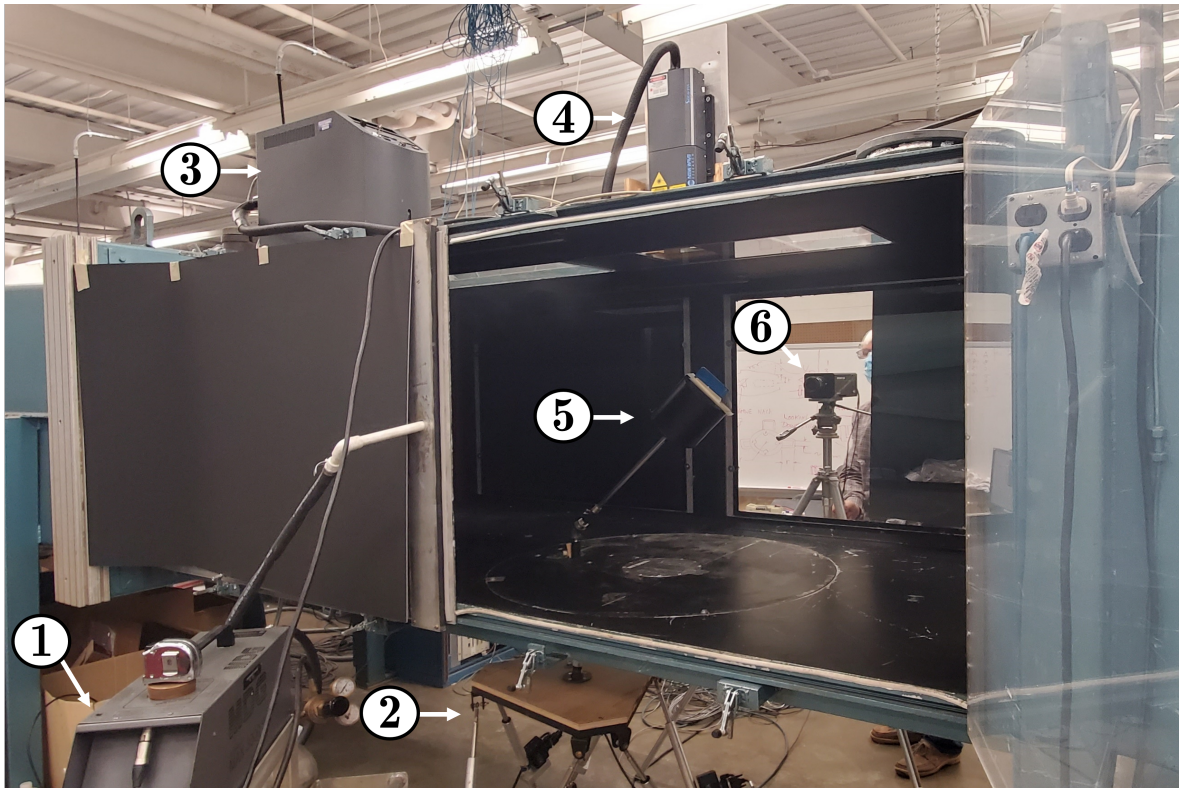

Fig. 12: Particle Image Velocimetry Setup at the ODU Subsonic Wind Tunnel

calibration card or meter stick mounted onto the model. The tunnel was then closed, powered up, and started using a NI LabVIEW virtual instrument. The flow speed was stepped up to the desired velocity and then fog was generated until the flow was appropriately saturated with oil particles. Once these factors were all coordinated, the laser and camera were triggered using the TSI Insight software to capture images of the illuminated oil particles in pairs at 3.75Hz. These pairs of images were used to correlate the location of oil particles across the small time interval in between frames, resulting in flow field velocity information. 100 pairs were collected and averaged to obtain an time-averaged flow field approximation. This process was repeated for each camera and angle setup described in Table 1.

Postprocessing of the PIV data was performed in MATLAB using the open-source add-on application PIVlab version 2.37 [21, 22]. This software allowed the calculation of flow-field velocities to be paired effortlessly with the industry-leading graphing capabilities of MATLAB. The postprocessing procedure was performed simultaneously for the full 100-image set of each angle configuration. This process started with a calibration image being loaded into the software, allowing the conversion of each pixel to a spatial distance in meters. Then a mask was created to prevent any attempt at correlating pixels outside the region of interest. This mask was applied to all image pairs for the data set. In accordance with recommended procedure from PIVlab creators [21], a multi-pass direct fast-Fourier transform correlation method was used for the data sets. The multi-pass procedure started with square interrogation windows 128 pixels wide, followed by a factor of 2 reduction in size to windows of 64 pixel side length. The third pass was once again reduced by a factor of 2 to an area of 32x32 square pixels. This last pass was repeated until the program had found an average acceptable quality among the correlations in space. The computation was performed on all image pairs and the resulting velocity distributions were averaged to obtain an average flow field. Multiple parameters were derived and plotted including velocity magnitude, axial velocity, and vorticity resulting in time-averaged images and animations of these factors.

Following the PIV tests, the model was prepared for force and moment tests. The pressure taps were cleared and the dummy load cell was replaced with an ATI Mini-40 load cell. The model was assembled with the load cell in line with the model-core which connects the body to the sting. The rear-face was designed so that no contact was made

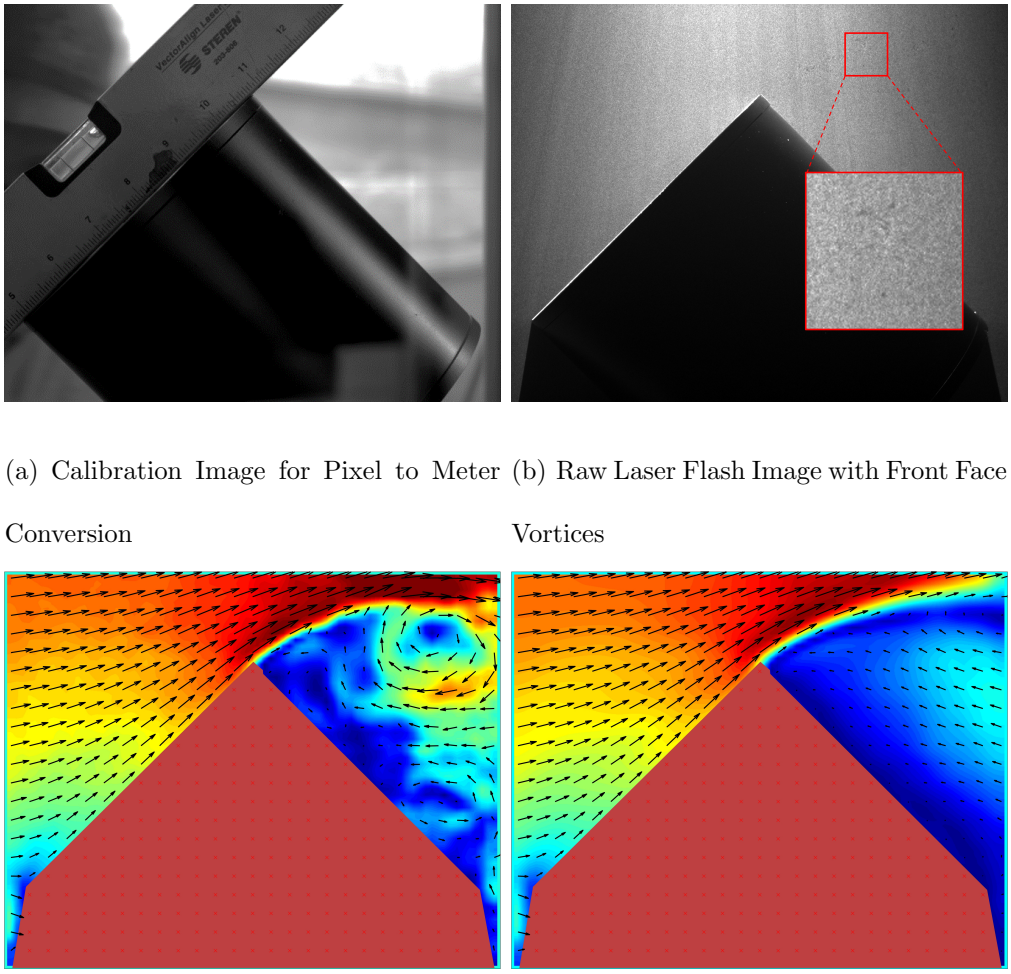

(a) Calibration Image for Pixel to Meter Conversion

(b) Raw Laser Flash Image with Front Face Vortices

(c) Instantaneous Velocity Contour

(d) Time-Averaged Velocity Contour

Fig. 13: Four Key Stages of PIV Postprocessing

with the sting allowing force measurements to remain uncompromised. Pressure tubing was fed through the iron-pipe sting, outside the tunnel, under the Stewart platform, and finally connected to the pressure-data acquisition system.

The pressure tubing and ATI Mini-40 load cell installed within the body, as shown in Fig.14, was not required to be reinstalled in between angle changes. This simplified the testing procedure significantly; however, the model did require separation from the piping in order to switch out the elbow section described earlier in this section. For each angle, the wind tunnel was stepped up in increments of 10m/s and then back down via the middle data points to verify the absence of sensor drift. This resulted in data points occurring in the following order (in m/s), 0, 10, 20, 30, 25, 15, 5. Pressure, force, and tunnel velocity data was collected simultaneously using the NI LabVIEW virtual instrument used to control the subsonic wind tunnel. The program collected an average of 100 data points and the data was exported to comma-separated value files for analysis. In total, static force and pressure data was collected for 91 combinations of flow speed and angle in an efficient test schedule.

Fig. 14: Internal Model Image of ATI Mini-40 Load Cell and Pressure Taps

3.2 NASA 6″ MSBS

Dynamic data of the fineness-ratio 1 cylinder was captured at the NASA LaRC MSBS during a series of runs with two model designs. The design of these models stemmed from combinations of standard practices used at the LaRC facility and a few case-specific considerations. First, the center of rotation relative to the cylinder geometry was desired to be

varied to ensure that different dynamic phenomena could be captured. Due to the small model size as well as ferrous material restrictions associated with the magnetic system, it was easier to manufacture multiple models with differing mass-distributions than to create a model design with variable interior components. This method was implemented by fabricating the model in separate fore-body and back-shell components with varying lengths as shown in Fig. 15. The second major design consideration was that there should be a sharp leading edge on the front and rear faces of the cylinder. Any chamfer or fillet would prevent clean separation around the sides of the model and diminish the comparability of these results to other tests. This was accomplished by 3D-printing the models with the flat faces on the print-bed ensuring smoothness, and following the manufacturing process with careful sanding of the sides to verify corner sharpness. The model was also designed with the following standard requirements of all models tested in the NASA LaRC MSBS.

1. Ensure blockage ratio of the model is less than 10%.

2. Allow enough interior space for the model to hold a 0.75″ diameter cylindrical permanent magnet.

The blockage ratio was calculated as the front facing area of the model (1.23in^2) divided by the tunnel cross sectional area (33.76in^2). After verifying that the blockage ratio would be acceptable and the diameter was large enough for housing the cylindrical permanent magnet, the designs were created with the specifications outlined in Table 2. The models were fabricated using a FlashForge Creator Pro 3D-printer, sanded to ensure corner sharpness, and painted with a matte-black finish to reduce glare in image capture. Two white circles for camera tracking were adhered to the curved face of the cylinder models, one on the

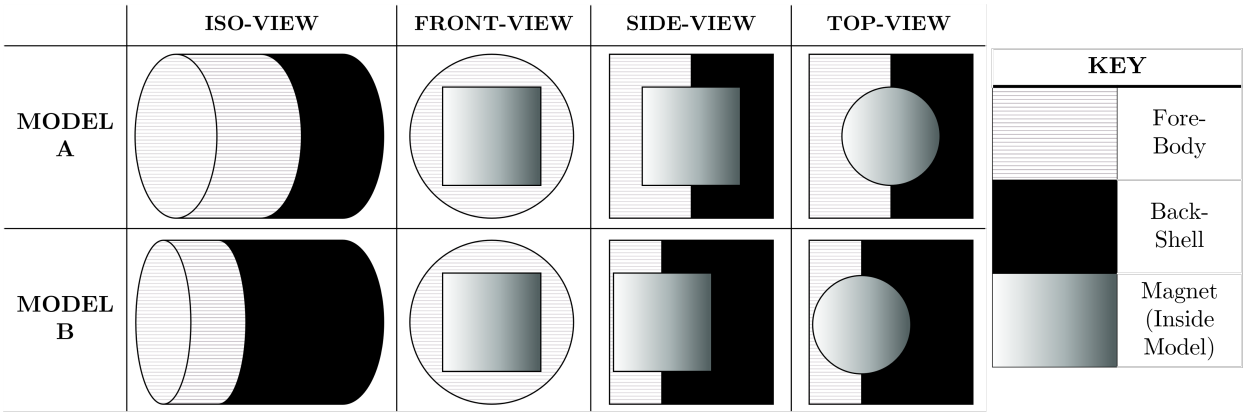

Fig. 15: Cylinder Model Configurations for NASA LaRC 6″ MSBS

fore-body and the other on the back-shell. Each model's components were weighed and documented for use in the LaRC tunnel, and then testing was able to proceed.

TABLE 2: NASA MSBS Cylinder Model Specifications

	Model A	Model B
Fore-Body Length (Inches)	0.625	0.40
Back-Shell Length (Inches)	0.625	0.85
Diameter (Inches)	1.25	1.25
Blockage Ratio (%)	3.6	3.6
Center of Gravity (% Chord)	50	32

The electromagnet and wind tunnel system were powered on and initialized via the MATLAB control script. The electronic position sensor was calibrated with the test section clear using the physical configuration panel and procedure outlined by Schott [10]. The first model was assembled by surrounding the permanent magnet core by the fore-body and back-shell and adhering them together using thin double-sided tape. The model was held in

the test section by hand, at the center of MSBS magnetization, and the coil currents were switched on allowing gravity to be counteracted. The camera systems were initiated and used to guide the model into the center of the camera views. This was accomplished by effectively changing the center of magnetization within the test section using the physical controls to offset the coil currents. All offsets were automatically recorded in the data acquisition software.

Data recorded by the system includes calibration settings, dynamic pressure, coil temperature, EPS x-y-z voltages, MSBS coil currents, time values, a video captured of the model, as well as a few derived parameters. The duration of a sample is configurable in the system and for the tests performed was set to 5 seconds. The sensor data set was acquired at a frequency of 1 kHz and the video data at 180 frames per second, resulting in 5 sensor samples per video frame.

The tunnel was sealed and testing began with the centered rotational axis model (model A). Data points were collected in correspondence with the test matrix in Table 3. During initial performance checks, it was determined that model A was easily excited into a state of continuous full-pitch rotation, which will subsequently be referred to as tumbling. Collecting pure oscillatory data with this configuration proved difficult and it was determined that obtaining data of the transition from oscillatory motion to tumbling would be an appropriate scope change. Three flow off data points were acquired (Run #1-3), followed by a successful transition point at run #4 . The flow speed was left unchanged and repeat measurements were taken to determine the rate of rotational acceleration and the maximum rotational velocity the model would achieve. With this data collected, the model was removed from the

test section and the forward rotational axis model was setup following the same procedure outlined above.

Model B was more resilient to oscillatory motion and tumbling which allowed a more extensive test of the dynamic motion compared to model A. The tunnel was stepped up to a dynamic pressure of 194Pa where oscillation was initiated, the flow was subsequently brought down to 45Pa to collect low speed oscillations. The tunnel velocity was then incrementally increased until the model's forces exceeded the tunnel's control capabilities.

TABLE 3: NASA MSBS Test Matrix

Run #		1	2	3	4	5	6	7	8	9
Model A	Dynamic Pressure (Pa)	0	0	0	10	10	10	10	-	-
	Flow Velocity (m/s)	0	0	0	4.9	4.9	4.9	4.9	-	-
Model B	Dynamic Pressure (Pa)	0	10	106	194	194	45	106	192	353
	Flow Velocity (m/s)	0	4.9	16.0	21.6	21.6	10.4	16.0	21.5	29.2

CHAPTER 4

COMPUTATIONAL METHODOLOGY

4.1 WORKFLOW OF THE COMPUTATIONAL CAMPAIGN

The computational campaign presented in this work was designed to support the experimental studies of the axially-oriented cylinder model previously discussed. The CFD effort was approached using the plan defined in Fig. 16. This plan is divided into four key phases of work, these being 1) campaign design, 2) preprocessing, 3) problem processing and 4) postprocessing, each of which will be described in this chapter.

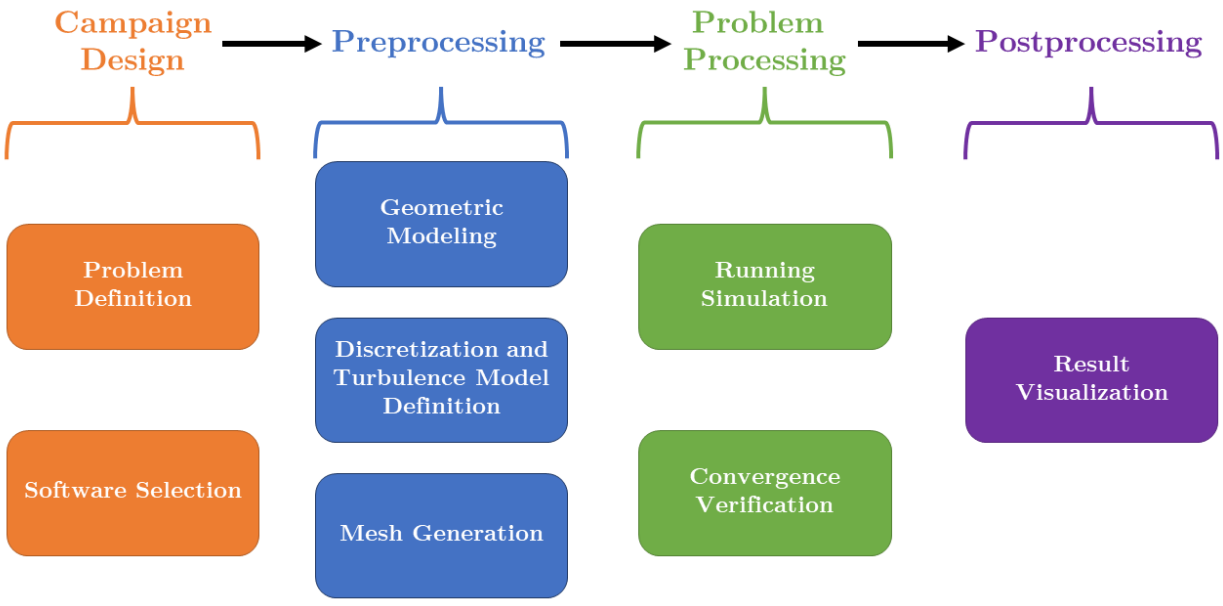

Fig. 16: Workflow of Computational Campaign

The first phase of work involves defining the scope of the CFD problem, as well as, the assumptions and computational conditions that will drive the model, the method itself,

and software choices. Once these factors were defined, a software package was chosen that could reasonably accomplish those goals while also accounting for availability and cost. The preprocessing of the problem is the most crucial phase as it encompasses all geometric modeling as well as the mathematical model (time discretization and turbulence model) selection and the mesh generation. The mesh generation and time discretization must be selected synchronously as convergence is codependent between the two. Once preprocessing is complete, the solver is run to iterate through the defined problem and the convergence is monitored. If satisfactory convergence (either monotonic or oscillatory) is reached then the data moves into postprocessing; however, if the convergence is found to not be satisfactory the preprocessing stage must be revisited and the time and space discretization examined. Converged results are sent into postprocessing where data is visualized in an informative and representative manner.

The aforementioned phases are described below in detail for the computational work performed on the axially-oriented cylinder.

4.2 CAMPAIGN DESIGN

The computational studies performed are accompanying tests to match between both the NASA LaRC MSBS and ODU wind tunnel experimental setups described in the earlier sections. The end goal of all the combined tests is to explore the flow structure of the low-fineness-ratio axially-oriented cylinder and to attempt to understand the origin of its dynamic motion. In order to attain this information it was determined to approach the problem in a similar setup to its accompanying experiments, starting with static tests and then performing more complicated dynamic tests. The sub-goals set to outline this

computational investigation are as follows;

1. Perform fixed-orientation free-stream tests of the cylinder at angles of attack ranging from 0 to 90°. Obtain the following data points;
   (a) Wake Structure Visualization
   (b) Forces and Moments
2. Determine feasibility of dynamic free-stream solutions and execute if feasible.

It was decided, based on interest and computational run time, that goal 1 above would be performed two-fold, once to obtain a steady-state solution and again to perform transient-static calculations. Adding the transient version provides a stepping stone of complexity from the static steady-state solution before the feasibility study of rotating transient models. In order to complete these goals, a suitable software package or set of packages needed to be chosen for the work to begin.

Typically, the preprocessing, mathematical solver, and the postprocessing can be performed in either separate programs designed individually for each of the three steps, or in a single packaged application that performs all three alone. The benefit of using three independent software packages is that the user can select a program with features that would facilitate the success of each step individually, specifically for their defined problem. Using an all-in one commercial package runs the risk of having one of the three CFD steps being weaker than the others. The benefit of using a commercial software is that there is less overhead for problem solving as there are little risks of compatibility issues and it is easier to tell where any problem lies. Another benefit for a new user, is that there is only one

software package to learn rather than three separated packages.

For this study it was determined that a commercial software would be best based on the reasoning above. Based on the goals needed to be reached defined previously, as well as, product availability, the software package scFLOW provided by Software Cradle Co. was selected. The application is a finite-element polyhedral-mesh all-in-one package with pre & postprocessor as well as a solver included. ScFLOW also has moving mesh and 6-DOF motion simulation capabilities which made it of interest for analyzing this blunt body model.

4.3 PREPROCESSING

ScFLOW's computational suite allowed for the entirety of preprocessing to take place in one location. In this section, the process of geometric model design and boundary condition parameters, as well as, time and space model selection and mesh generation are presented.

4.3.1 GEOMETRIC MODELING

Rather than importing a CAD model from a traditional software, the simplicity of the cylinder model allowed for it to be rendered from scratch in the scFLOW preprocessor. The model being studied is a simulated version of the 1.75″ diameter cylinder used in the NASA LaRC MSBS experiments. It was determined that for minimization of computational complexity, the boundaries would represent a free-stream condition rather than fully simulate wall conditions of the LaRC MSBS octagonal test section. To this end, a fluid region with axial symmetry around the model was created with free-slip wall boundary conditions (Fig. 17).

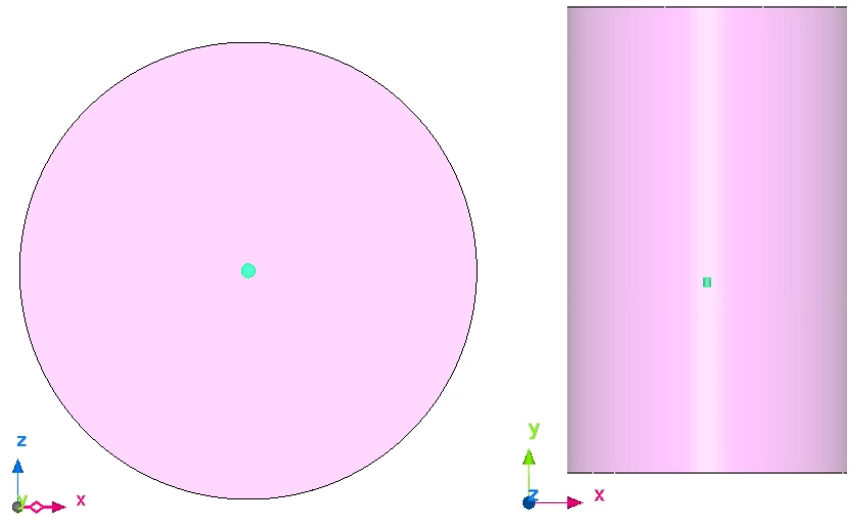

(a) Front-View Perspective of Model & Fluid Region

(b) Top-Down Perspective of Model & Fluid Region

Fig. 17: Views of the Fluid Region (Pink) and Cylindrical Model (Green) in ScFLOW

The inlet of the fluid region was set with the flux condition of 32.86m/s normal velocity and a turbulence intensity and ratio (eddy viscosity/molecular viscosity) of 5 and 100 respectively. The outflow conditions at the downstream face of the fluid region were set to normal inflow/outflow in the scFLOW preprocessor with the same turbulence intensity and ratio settings as the inlet. The surface of the cylinder model being tested was set to no-slip with no roughness considered. The size of the fluid region was determined with respect to the chord of the model being examine and is explained in Eq. 11 - 13.

$$c = 1.75in = 0.04445m$$

$$L_u > 20 \times c = 35in = 0.889m \tag{11}$$

$$L_d > 30 \times c = 52.5in = 1.3335m \tag{12}$$

$$D_{fr} > 20 \times c = 35in = 0.889m \tag{13}$$

Following these relations for fluid region size allows ample time for the flow to develop from the inlet, as well as an appropriately sized wake region where the flow is most complex. Special attention went into the refinement of the wake region and will be discussed in Section 4.3.3.

For the fixed-orientation tests, the model's angle of attack was selected and a separate case generated for each angle being simulated. This process resulted in the creation of 19 geometries ranging from 0° to 90° angle of attack. By defining the problem geometry, flow boundaries, and wall boundaries, the problem scope is set for the fixed-orientation cases. The next step in the preprocessing routine is to choose mathematical models that can appropriately estimate the conditions provided and then to generate a mesh that provides optimum model convergence.

4.3.2 MATHEMATICAL MODEL SELECTION AND DEFINITION

ScFLOW is a program capable of performing many multi-physics problems, from simple laminar flow cases to fluid-temperature interactions of multi-phase flows. For the model we have defined in Section 2.3, scFLOW's selection of turbulent flow solving methods was adequate. The CFD campaign taken was separated into two mathematical models, the first

being a steady-state method and the second being transient or time-dependent method both assuming incompressible air at 20^oC as the flow medium.

RANS k-ϵ models with standard parameters were incorporated for quick testing of the model at each angle of attack. LES methods were used at key pitch angles to balance the computational costs and the value added for comparison to the wind tunnel tests.

4.3.3 MESH GENERATION

After the definition of discretization methods and turbulence models, a mesh needs to be designed for the geometry that can complement the mathematical methods. ScFLOW uses an octree based mesh generation algorithm rather than a Delaunay mesh which is otherwise commonly used. The octree method encloses the geometry into partitions of eight octants with refinement arising through recursive subdivision into smaller sets of octants, demonstrated in Fig. 18. The octree method of generating meshes does not rely on a well defined surface mesh to start, making it more robust than the Delaunay method. The disadvantage of using this method is that there is more adjustment and definition needed to appropriately scale the octant size as it reaches the model. ScFLOW's mesh generation functionality performs these adjustments automatically.

For the geometry previously defined in Section 4.3.1, 3 levels of refinement were created; coarse, medium, and fine, each being approximately twice as many elements as the previous. The purpose of the multiple refinement levels is to provide a confirmation of grid independence of the solution. Each octree was created in scFLOW's preprocessor based on a few key parameters outlined in Table 4.

The parameters set for each octree set were max octant size, surface octant size, influence

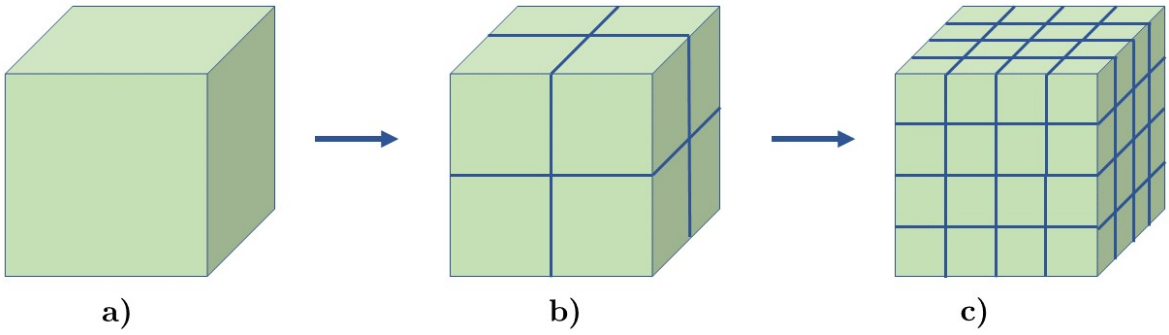

Fig. 18: Octree Refinement Process, a) Refinement Level 0, b) Refinement Level 1, c) Refinement Level 2

range of the surface octants, and the minimum range of octants per refinement level. The maximum octant size dictates the largest element width and height in the free stream. The surface octant size sets the smallest element width and height on the surface of the cylinder. Influence range defines the range relative to the max octant size that the smallest octant size must exist. This parameter ensures that even with small near-wall octants, there is an appropriately refined region away from the wall. The last parameter is similar to the influence range; however, applies to all octants and is based on the total element count. For a refinement level range of 4, the octree will have atleast 4 layers of octants at a given size before expanding to a larger size. This increases model accuracy at the cost of increased nodes and computational time. These variations in parameters result in three octrees of varying designs displayed in Fig. 19.

There was one additional step in the octree generation phase before mesh generation could start. Refining the mesh close to the model is good practice; however, extra care needs to be performed for blunt body aerodynamic problems. The wake downstream of the

TABLE 4: Octree Generation Parameters

Refinement Level	Max Octant Size (mm)	Surface Octant Size (mm)	Influence Range	Δ Refinement Level Range
Coarse	35	1	2	4
Medium	22.225	0.5	2	4
Fine	11.1125	0.25	2	4

model contains flow that is significantly more complex than the rest of the stream away from the cylinder. It is for this reason that the octree level was refined in a region behind in the model. This extra refinement region surrounds the model by $2c$ radially, starts $2c$ upstream from the model, and extends $20c$ downstream from the model. Within this region, each octant except the octants on the model surface were subdivided once for extra resolution.

Once the octrees were defined and generated, the mesh creation process was performed. Setting up the octree parameters preemptively takes care of most of the mesh sizing steps; however, it was important that the near model region be defined in a structure mesh rather than polyhedral as shown in Fig. 20. This industry practice is defined by finding the desired Y+ and using it to estimate first cell size. The Y+ value can be written as:

$$Y+ = \frac{\rho \cdot U_T \cdot \Delta s}{\mu} \tag{14}$$

where ρ is the fluid density, U_T is the frictional velocity, Δs is the first cell height, and μ is

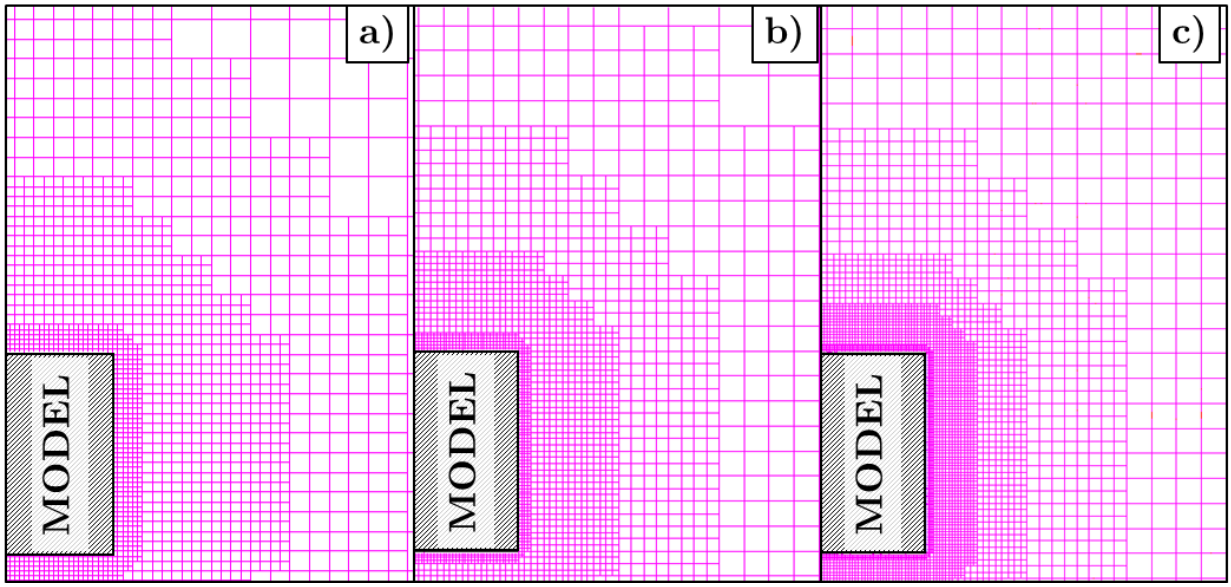

Fig. 19: ScFLOW Generated Octrees, a) Coarse Refinement, b) Medium Refinement, c) Fine Refinement

the fluid viscosity. U_T can be defined as:

$$U_T = \sqrt{\frac{\tau_\omega}{\rho}} \tag{15}$$

$$\tau_\omega = \frac{1}{2} \cdot C_f \cdot \rho \cdot U^2 \tag{16}$$

where τ_ω is the wall shear stress, C_f is the skin friction coefficient, and U is the free stream velocity. The skin friction coefficient was estimated from empirical values [23], whereas the rest of the values were inlet conditions for the solver.

Following industry best practices for external flows, our desired $Y+$ value is 1. Thus Eq. 14 can be rewritten and solved for Δs as below;

$$\Delta s = \frac{Y + \mu}{\rho \cdot U_T} \tag{17}$$

$$= 8.3402 \mu m = 0.0083402 mm$$

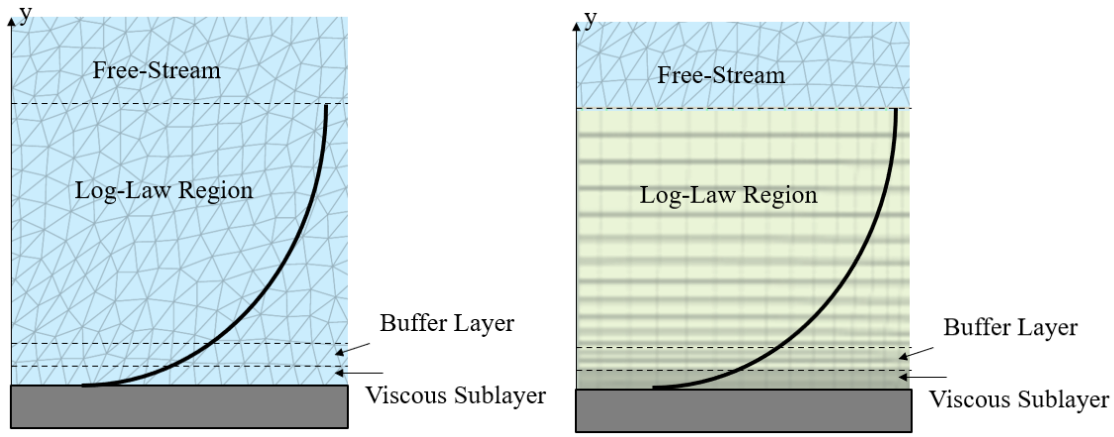

(a) Non-Uniform Mesh Close to Model Body (b) Structured Mesh Added to Near-Wall Flow.

Fig. 20: Unstructured vs Structured Near-Wall Mesh for Effective Flow Resolution in Boundary Layers

TABLE 5: Approximate Polyhedral Mesh Statistics

Refinement Level	Mesh Node Count	Mesh Face Count	Mesh Element Count
Coarse	2,800,000	3,600,000	600,000
Medium	6,900,000	8,500,000	1,400,000
Fine	36,500,000	44,500,000	7,000,000

The meshes generated for the runs varied in element, node, and face count between each angle of attack model; however, the approximate quantities are outlined in Table 5 for the course, medium, and fine mesh levels that were created. The increased spatial resolution of the grids allowed finer differentiation of velocities at the cost of computational time. LES

runs were performed on medium meshes due to the computational overhead that would be required for a fine spatial and temporal run.

4.4 PROBLEM PROCESSING

The scFlow solver was run on the ODU Turing HPC cluster using the Slurm job scheduler. Linux bash scripts were written to automate the scFlow solver file execution for the range of angle of attack cases. Each simulation was performed on 48 cores of the HPC's Intel Xeon E5-2660 2.20GHz hardware.

4.5 POSTPROCESSING

Flow visualization and parameter exporting from the results were performed in scFLOW's postprocessor suite. Contour plots were created to match that of the wind tunnel PIV runs for both RANS and LES results. ScFLOW allowed simple collection of surface pressures, forces, and moments both in steady state and transient calculations. These quantities were exported and analyzed in MATLAB for comparison to wind tunnel results. Animations of the flow for temporal runs were also generated for visualization purposes.

4.6 LES ROTATIONAL RUN SETUP

Time permitted the design and completion of a dynamic LES computation to assist in bridging the gap between static and dynamic experimental results. The run was accomplished using scFLOW's discontinuous mesh solver, with a fixed rotational rate applied to the cylinder. While scFLOW does have 6-DOF simulation capabilities, it was deemed out of scope for this work. The fluid region was designed as a $20c$ diameter cylinder encompassing

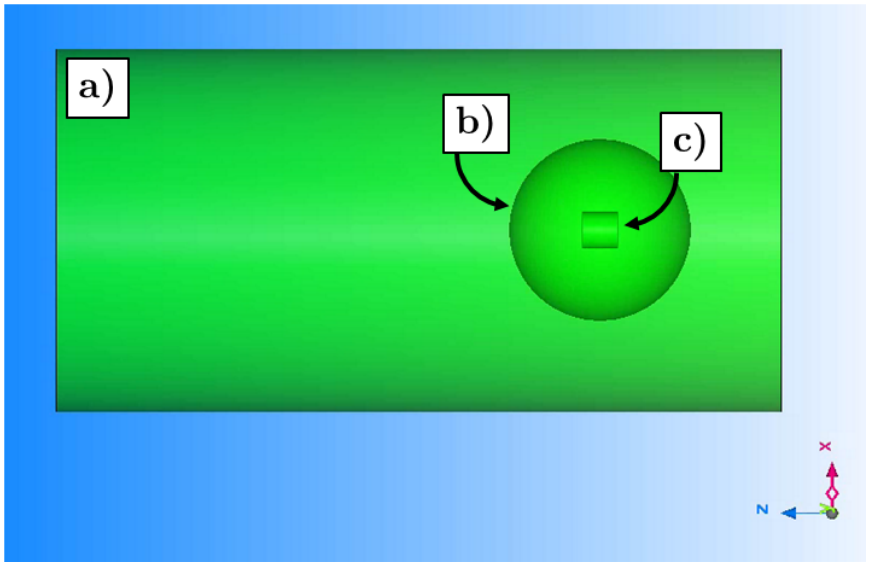

Fig. 21: Dynamic ScFlow LES Run Design of a) Fluid Region, b) Rotational Sub-Region, and c) Model

a $5c$ diameter sphere which is the rotational domain. This configuration is displayed in Fig. 21.

The rotation was set to begin after 0.1s, and to rotate at a fixed rate of 2Hz until the time reached 2.5s. The solver was set to LES second order with a fixed Courant number of 0.9. The run was performed on the ODU Turing HPC cluster using 128 cores.

CHAPTER 5

STATIC RESULTS

5.1 ODU LOW-SPEED WIND TUNNEL RESULTS

The static experiments at the ODU subsonic wind tunnel resulted in force, moment, pressure and flow structure data for the configurations outlined in the previous chapter.

5.1.1 FORCE AND MOMENT

At each flow condition data point, 100 measurements were taken from the ATI Mini-40 sensor and were used to calculate drag and lift coefficients and their respective standard deviations. All error bars on subsequent graphs represent ±2 standard deviations of the mean of the data. The resulting drag and lift coefficients as well as their respective standard deviations are plotted in Fig. 22 for a Reynold's Number of 1×10^5.

The drag coefficient follows a roughly parabolic curve in the region of -10° to +10°. From 35° to 45°, the drag is nearly constant, with the coefficient beginning to lower at 55°. The 80° to 90° follows a negative trend to the lowest drag coefficient found at 90°. The lift values were much smaller in magnitude and effected more by model vibrations. There is a high error in the 0° angle of attack data due to the oscillatory nature of the flow.

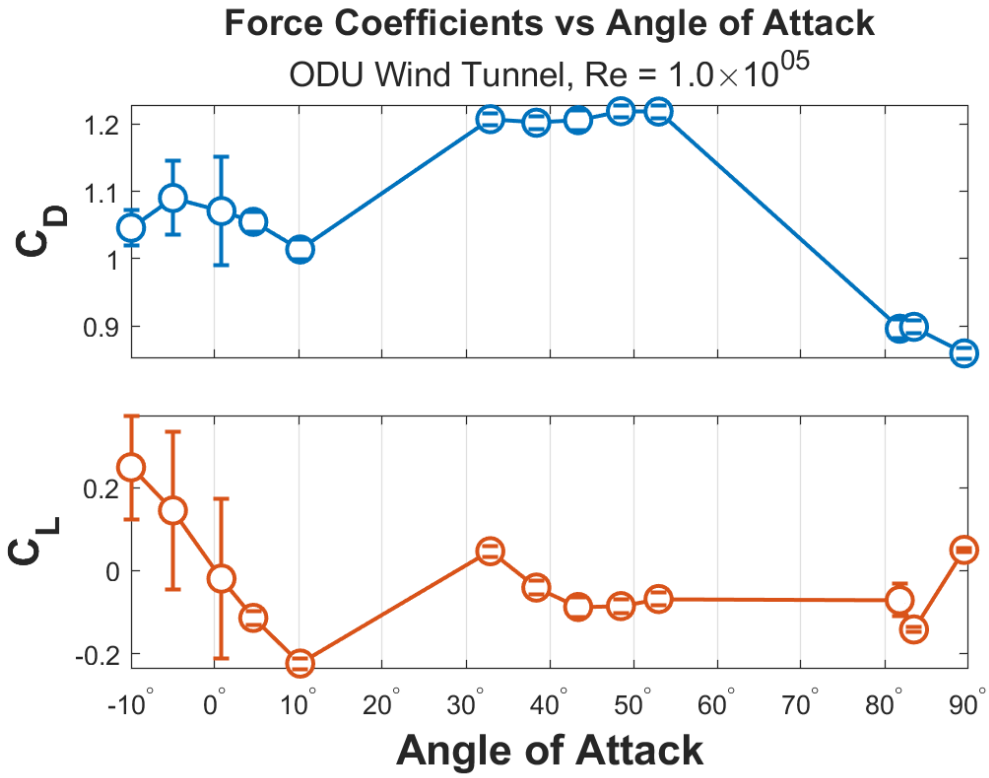

Fig. 22: Drag and Lift Coefficients vs Pitch for the ODU Wind Tunnel Test at $Re = 1.0e05$

Moment data was also collected, with the most significant results coming from pitch moment. Non-dimensionalization was performed using the cylinder's face surface area as the reference area. The moment coefficients were plotted for pitch, yaw, and roll, and can be seen in Fig. 23.

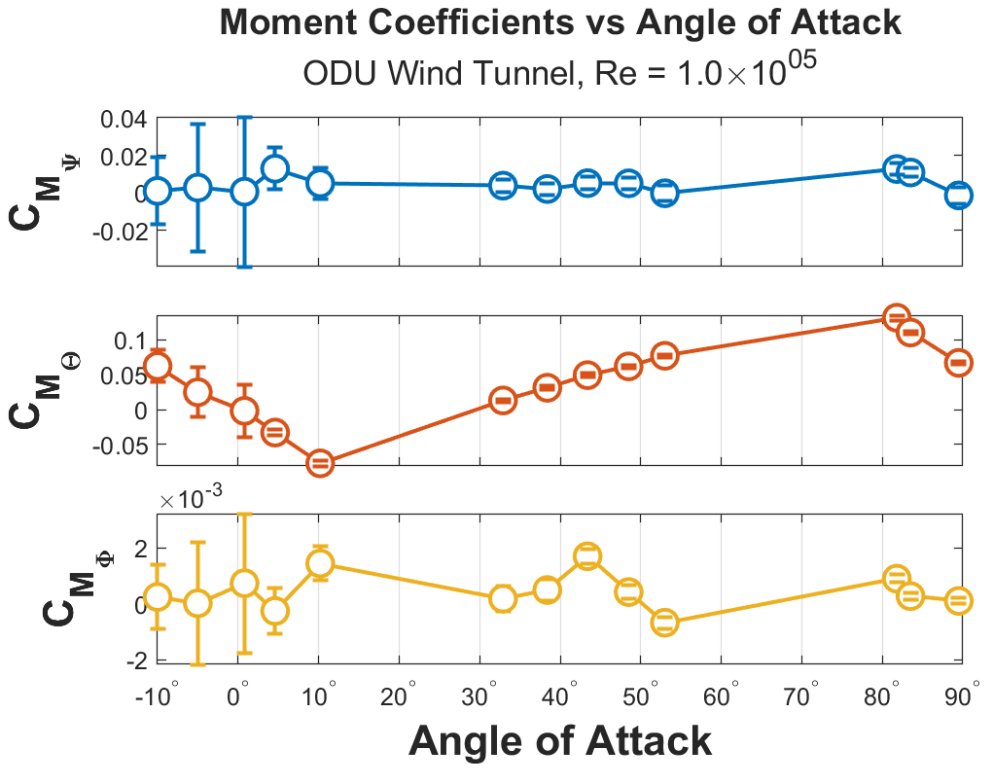

Fig. 23: Pitch, Yaw, and Roll Moment Coefficients vs Pitch for the ODU Wind Tunnel Test at $Re = 1.0e05$

5.1.2 PRESSURE RESULTS

The pressure data was non-dimensionalized and averaged at each angle of attack and pitot tube location. The standard deviation was also calculated at each location. The results of this process, as well as the orientation of the pressure taps are displayed in Fig. 24.

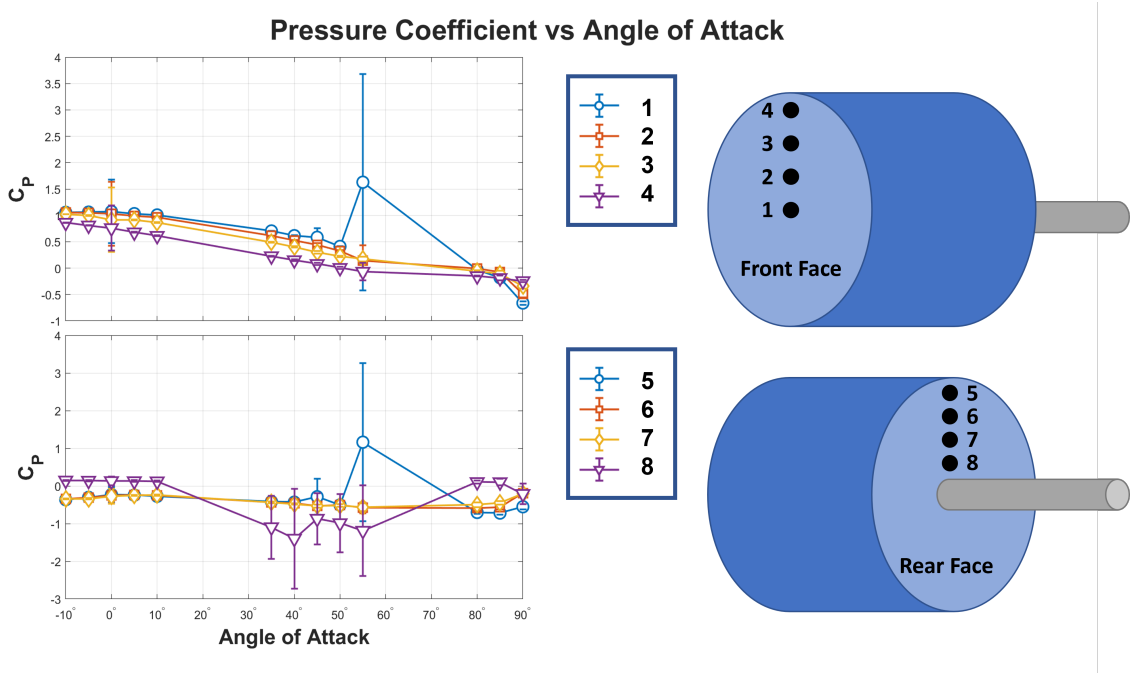

Fig. 24: Average Coefficient of Pressure vs Angle of Attack with Standard Deviation Error Bars

5.1.3 PARTICLE IMAGE VELOCIMETRY

Flow visualization results are presented starting with PIV, then with CFD results. The orientation of the cylinder in the flow field images is depicted visually in Fig. 25. The CFD flow field images were framed to match the PIV results, allowing an easier comparison of fields.

PIV flow visualization results were collected, of which the time-averaged velocity magnitude visualizations are presented in Fig. 26. 0° shows a fully separated wake with the recirculation region being fully captured. 10° instantaneous photos had a mix of reattached and detached flow fields; however, the time averaged value does show reattachment occurring at the trailing edge. 45° shows the fully attached front face of the cylinder with a

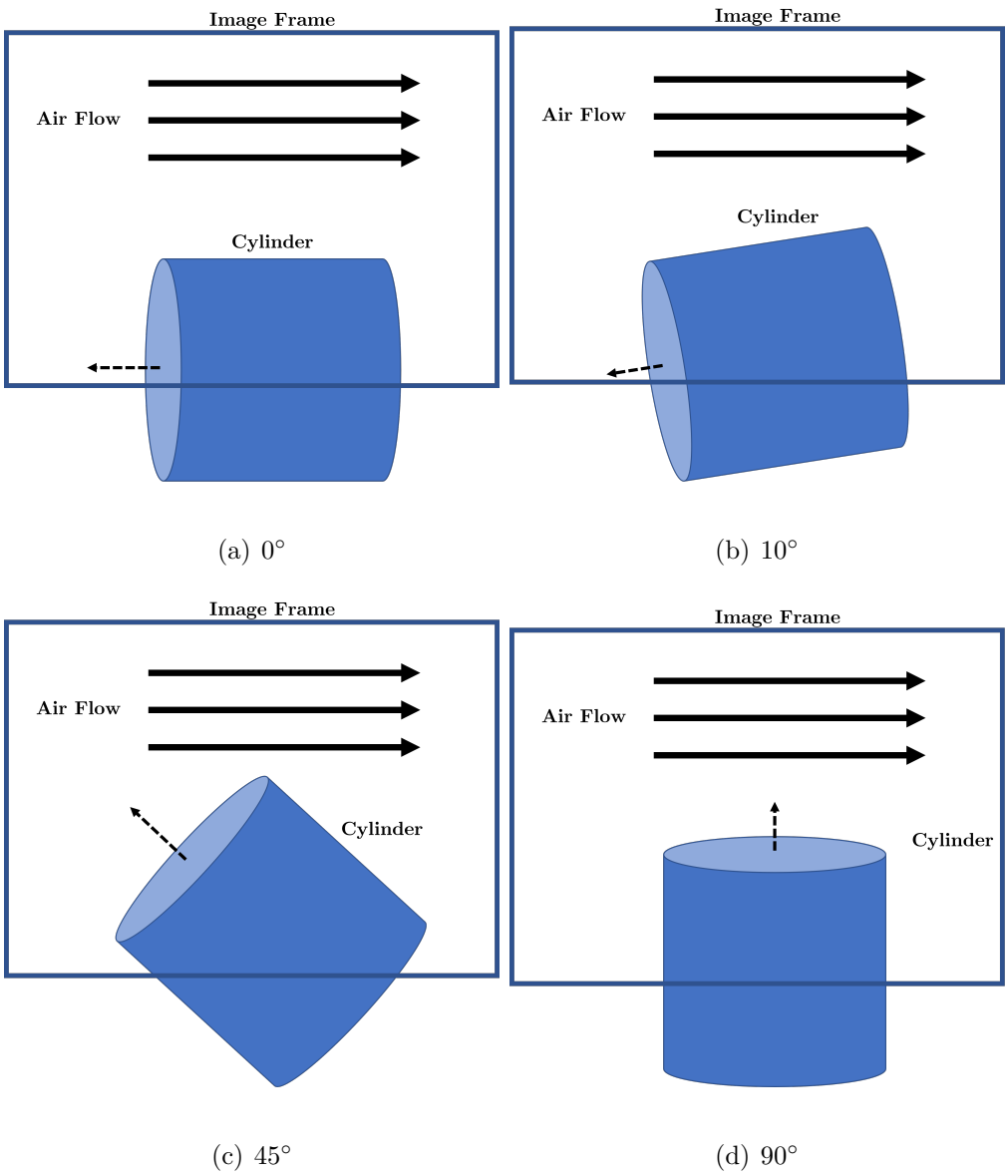

(a) 0° (b) 10°

(c) 45° (d) 90°

Fig. 25: Visual Depiction of Model Orientation in All Flow Visualization Result Images

large recirculation region. The 90° time-averaged result shows attachment on the face of the cylinder and a small recirculation region.

The PIV software captured axial velocity and vorticity in addition to the results in Fig. 26. These additional variables were plotted and are included in Appendix A along with

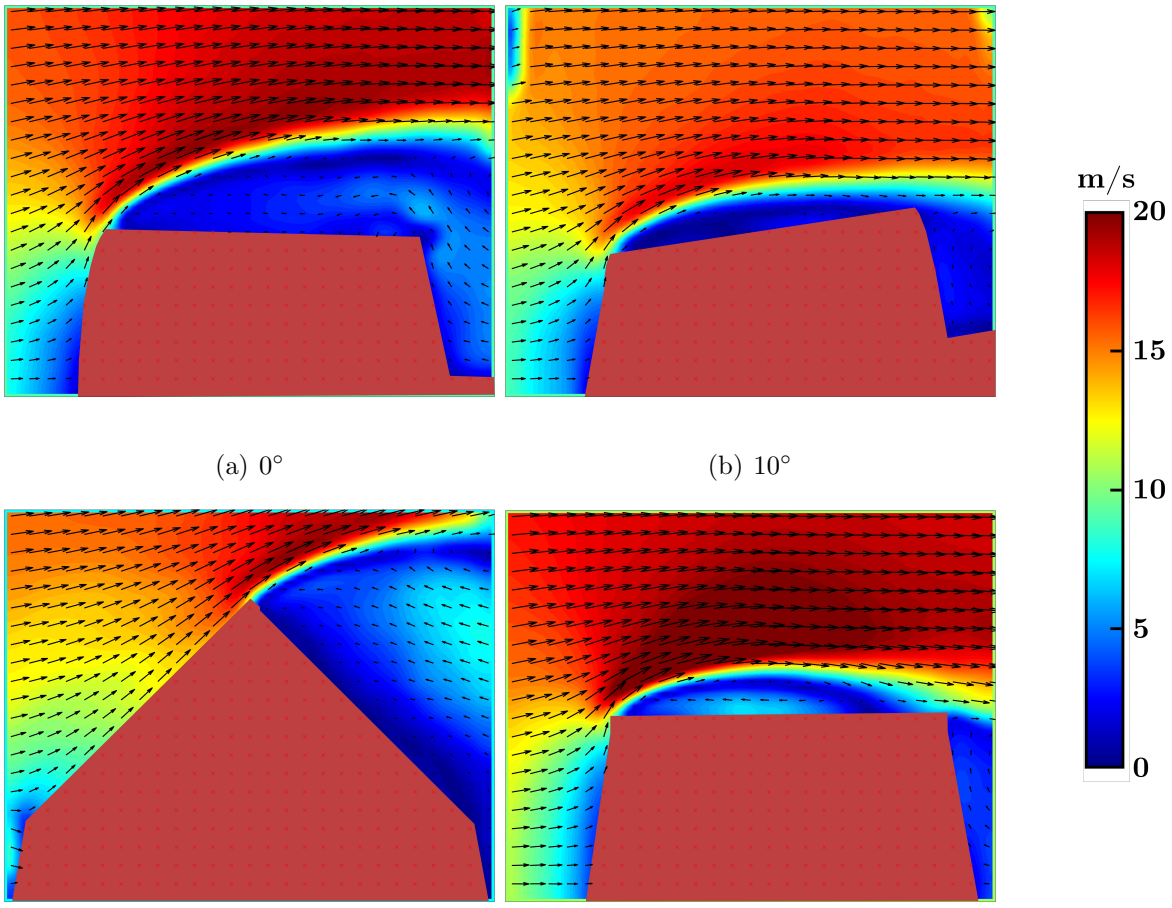

(a) 0°

(b) 10°

(c) 45°

(d) 90°

Fig. 26: Velocity Magnitude Renderings of PIV Correlations for 0°, 10°, 45°, and 90°

zoomed-view runs of 0° and 10°.

5.2 COMPUTATIONAL RESULTS

The CFD runs resulted in large amounts of data, both flow field visualizations and force, moment, and pressure plots. The results have been tailored to best compare and contrast the more limited results of the experimental setup.

5.2.1 FORCE AND MOMENT

The RANS and LES results for drag and lift coefficients are displayed in Fig. 27. The slope and magnitude of drop between 0 and 10° for both drag and lift correlate for both LES and RANS with LES estimating a larger drag coefficient. The drag then follows a bell curve shape centered at 40°, the tail end of which begins to change slope at 75°, evening out at 90°. The LES follows a similar trend in terms of direction; however, with a limited number of data points in this region it is impossible to fully corroborate the trends.

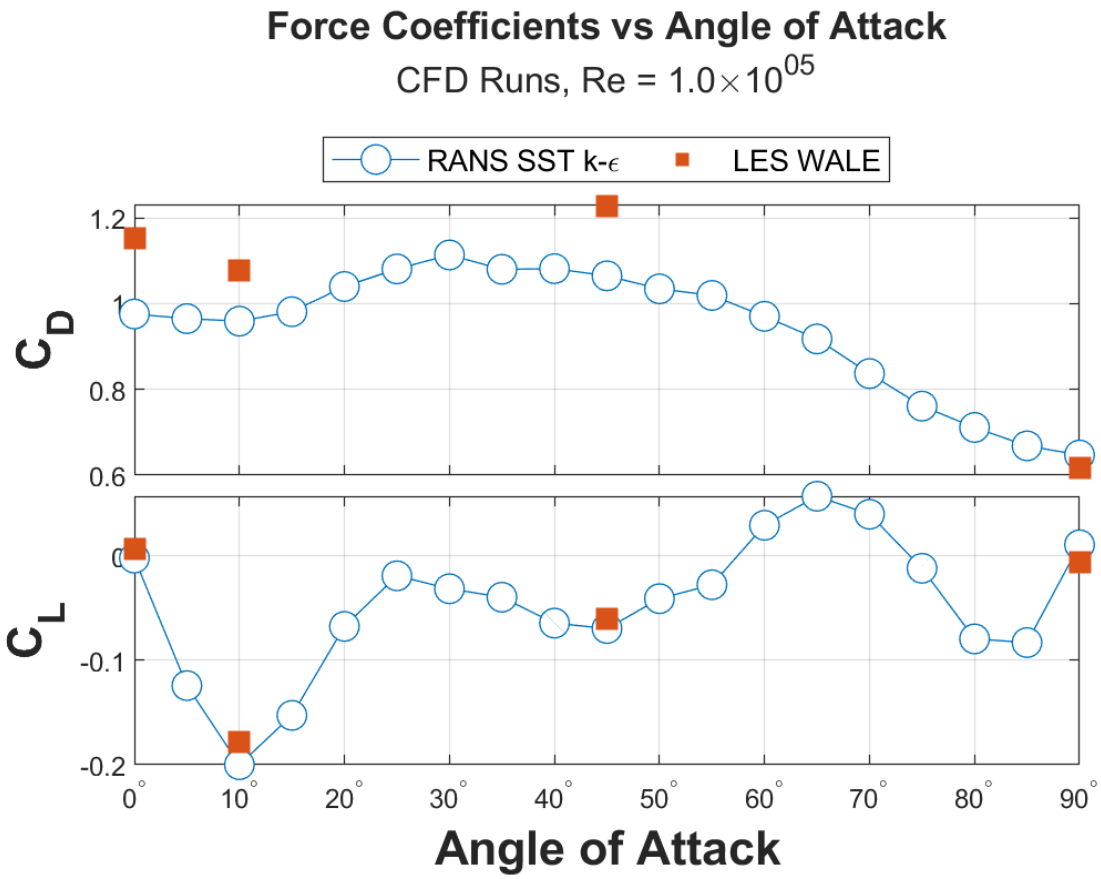

Fig. 27: Drag and Lift Coefficients vs Angle of Attack for the CFD Tests

5.2.2 FLOW VISUALIZATION

RANS and LES results were oriented to mimic those of the wind tunnel tests, with velocity magnitude contour plots being displayed in Fig. 28 and Fig. 29. The RANS flow structure shows a fully separated flow for 0°, local reattachment at 10°, full frontal attachment at 45° and a small recirculation zone for the 90° case.

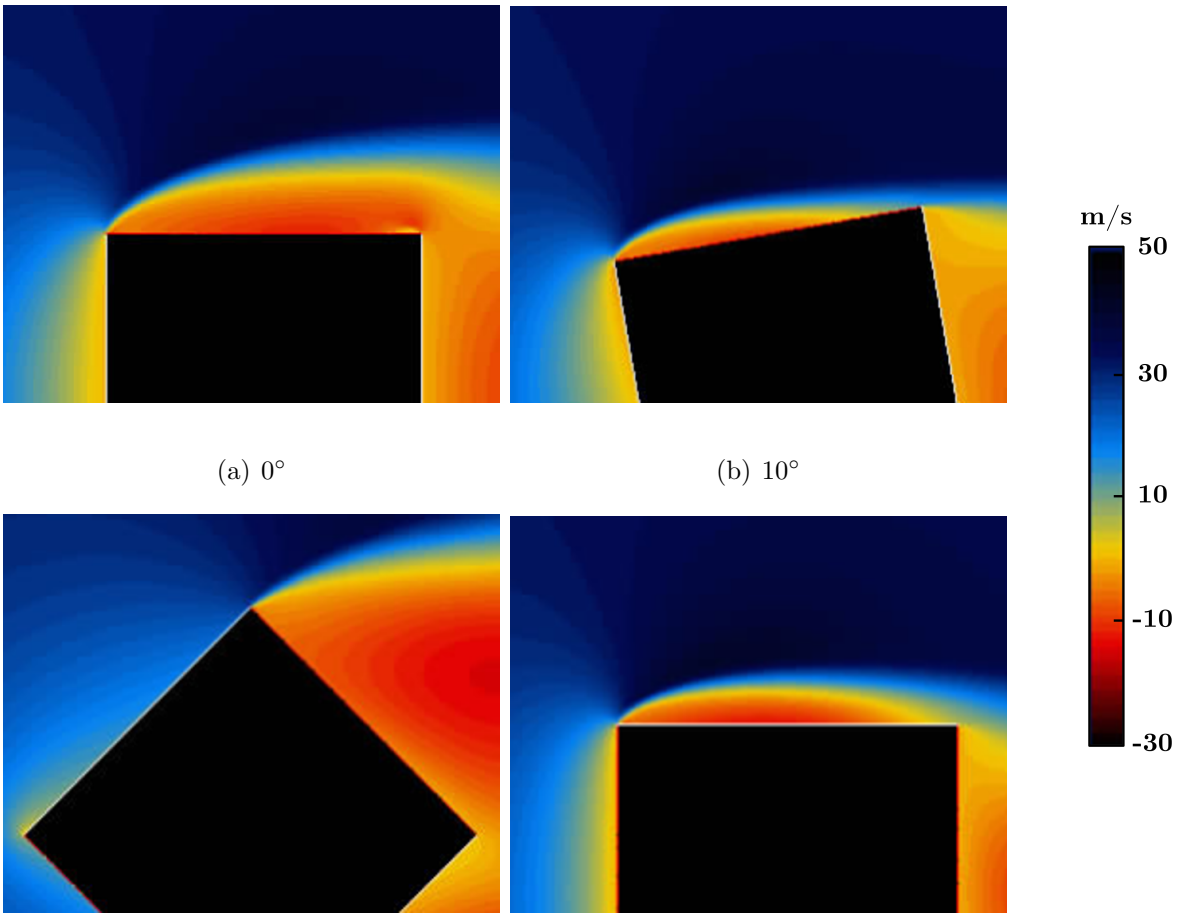

(a) 0° (b) 10°

(c) 45° (d) 90°

Fig. 28: Velocity Magnitude Renderings of RANS Computations for 0°, 10°, 45°, and 90°

The LES results display the large recirculation zone of the 0° cylinder, with more space between the wall and the edge of the boundary layer than with the RANS results above.

The 10° contour shows reattachment but closer to the trailing edge than that of the RANS solutions. The 45° case shows no separation on the windward face and the 90° case has a small recirculation zone.

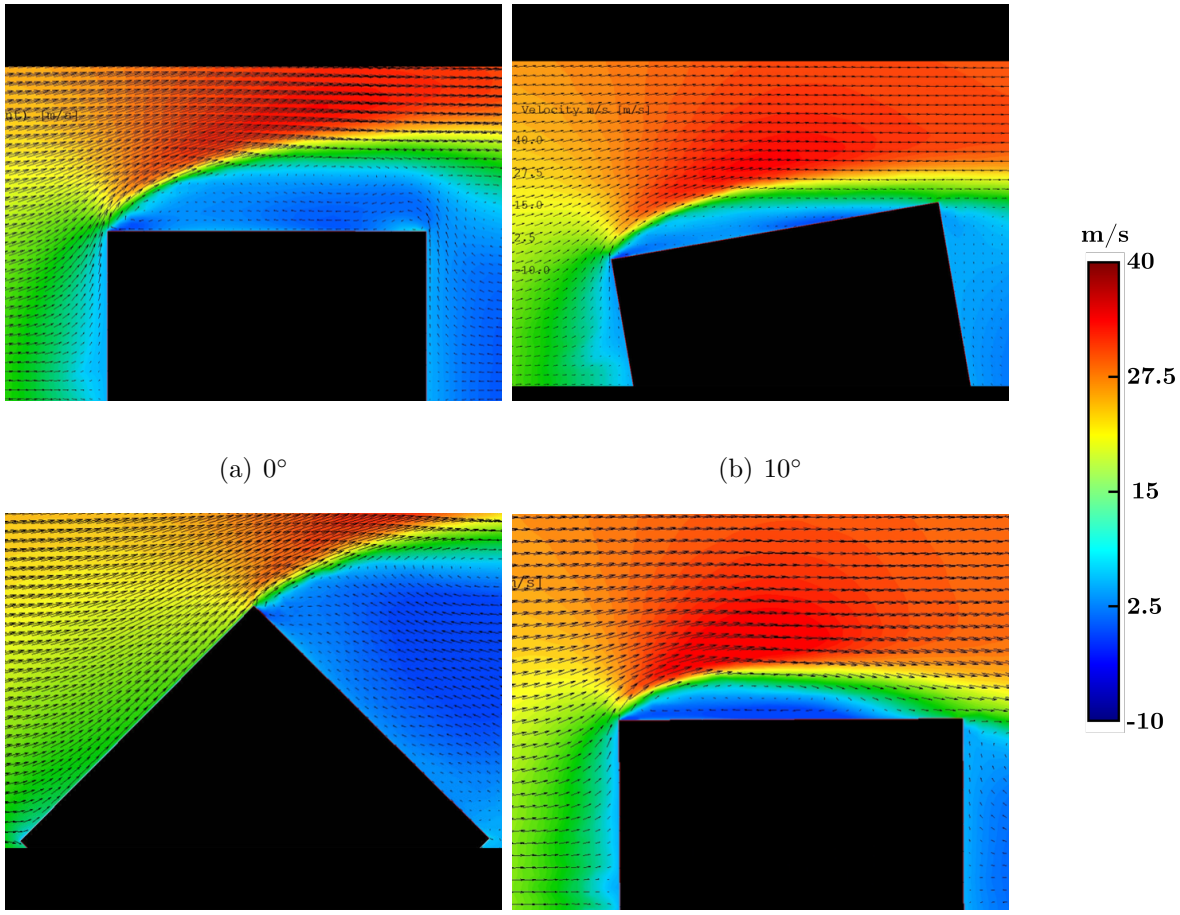

(a) 0° (b) 10°

(c) 45° (d) 90°

Fig. 29: Velocity Magnitude Renderings of LES Computations for 0°, 10°, 45°, and 90°

CHAPTER 6

DYNAMIC RESULTS

6.1 LES ROTATIONAL RUN

The dynamic LES computational test described in Section 4.6, resulted in time-series model forces and moments, as well as flow field visualization for the cylindrical model. Five full cycles at a rotational velocity of 2Hz were captured, with a temporal data resolution of 31kHz and a visualization resolution of 100Hz. The angle of attack was calculated for the model at each time step, and the forces and moments were examined in time-based analysis and in angle-averaged analysis.

The time-based analysis was performed to identify key areas of interest. Force and moment coefficients were compared in time across the 2.5s run, with the full graphs being shown in Fig. 30 and Fig. 31 below. The drag coefficient oscillates between approximately 1.2 and 0.8 across the 5 rotations. The lift coefficient is also oscillatory; however, the noise obscured much of this coefficient's lower amplitude. The side force coefficient shows no sign of temporal dependence, which is expected. The pitching moment graph shows a nearly sawtooth behavior rather than pure sinusoidal. The roll and yaw coefficients are much lower amplitude, with the latter being oscillatory in time and the former appearing independent of time.

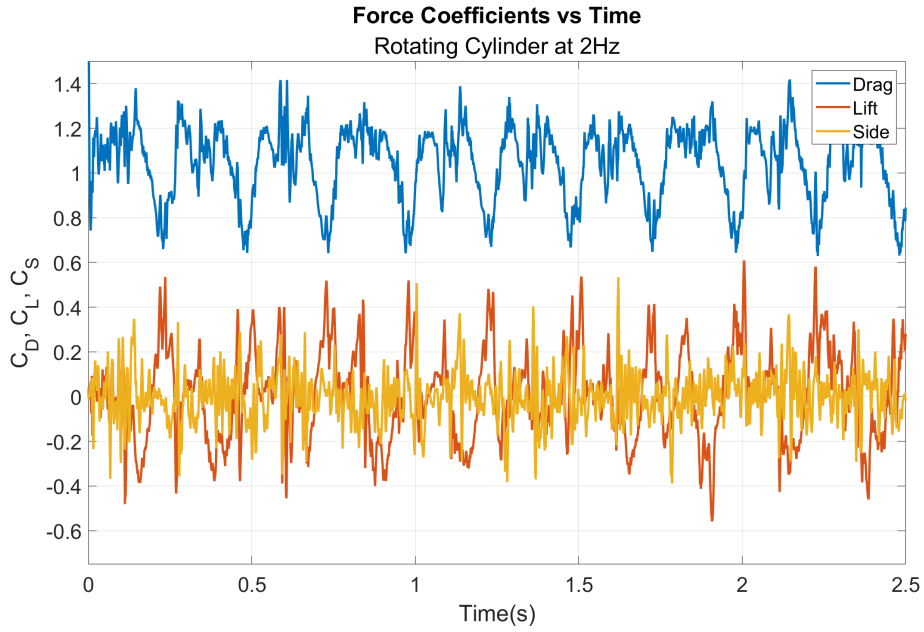

Fig. 30: Drag, Lift, and Side Force Coefficients vs Time for the Rotating LES Run

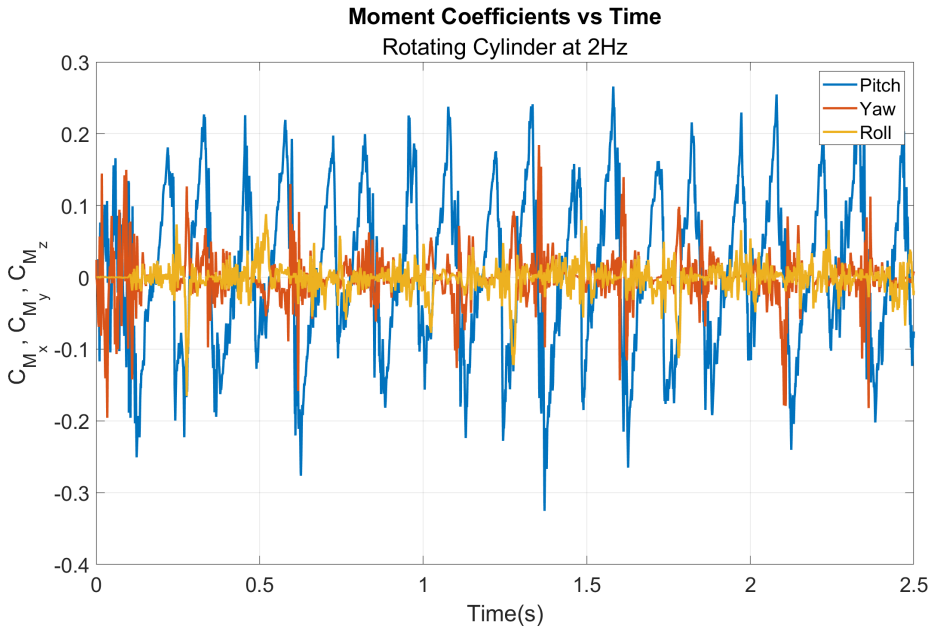

Fig. 31: Pitch, Yaw, and Roll Moment Coefficients vs Time for the Rotating LES Run

Additional analysis of the pitching moment, drag, and lift coefficients in time was performed. The data set was grouped into each rotation from 0° to 180°. Due to model symmetry, the angle is considered wrapped after 180° rather than 360°. These rotations were then averaged together based on angle of attack. An example of this process is showcased for the pitching moment in Fig. 32.

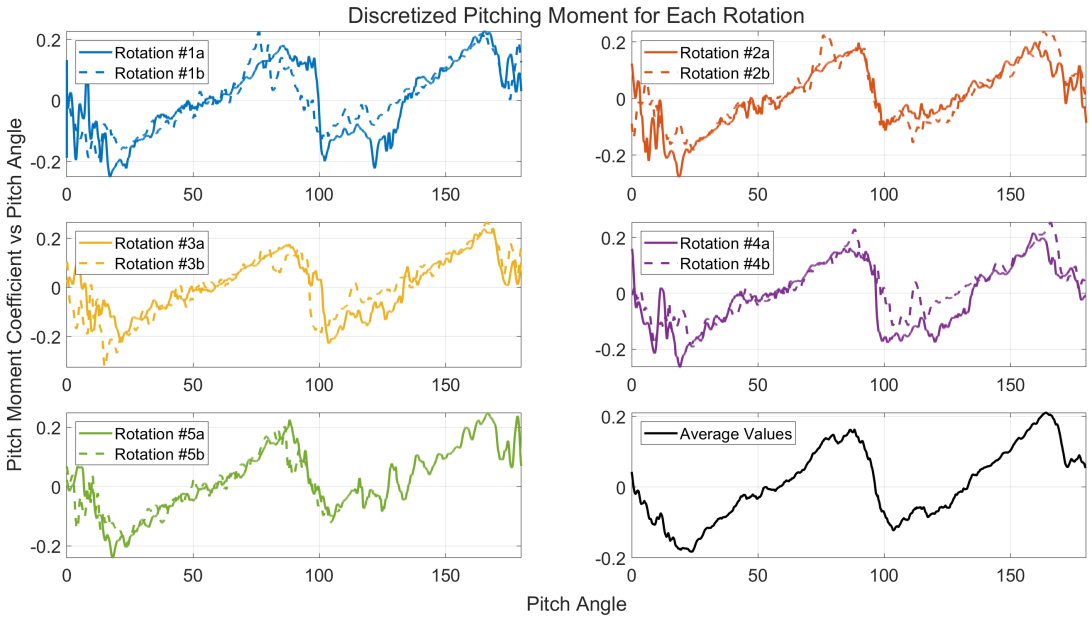

Fig. 32: Unwrapping Technique Used to Average Coefficients at Different Angles of Attack, Showcased for Pitching Moment

The averaged unwrapped force and moment coefficients are displayed in Fig. 33 and Fig. 34 respectively. The drag coefficient minimizes when the lateral surface is oriented perpendicular to the flow, whereas the lift coefficient peaks at this point. The standard deviation is also plotted in these graphs, with the peak occurring in lift at the 90° case. The pitching moment average is much higher than the yaw and roll moments, with maximum standard deviation occurring at the 0 and 180° locations.

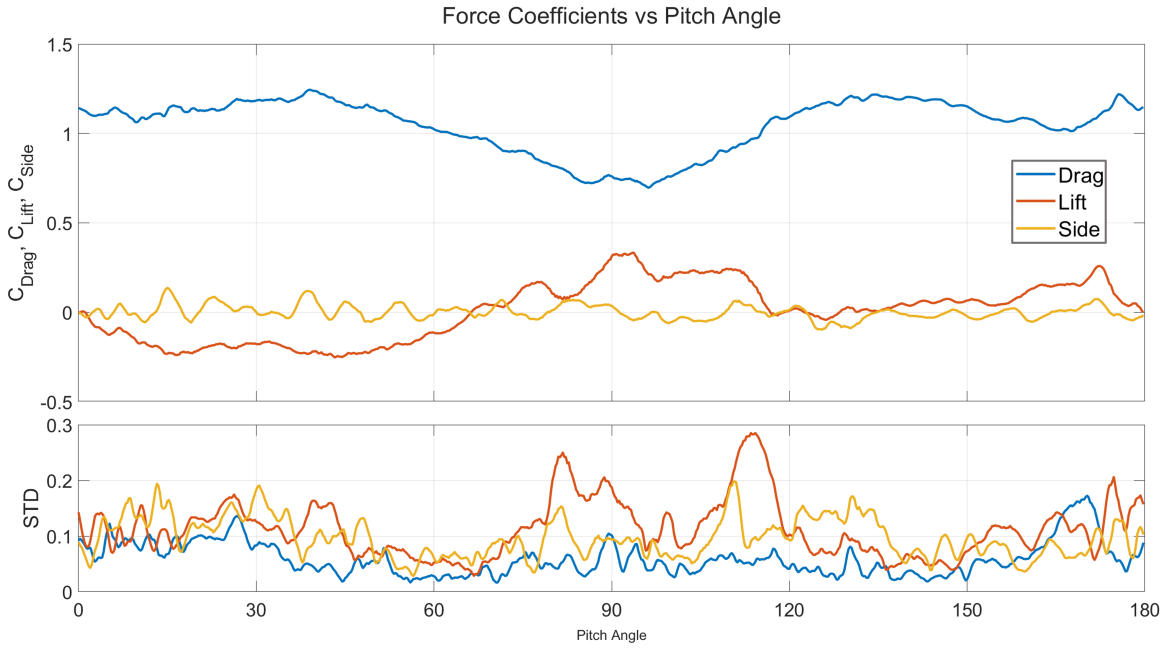

Fig. 33: Dynamic LES Drag, Lift, and Side Force Coefficients vs Pitch Angle

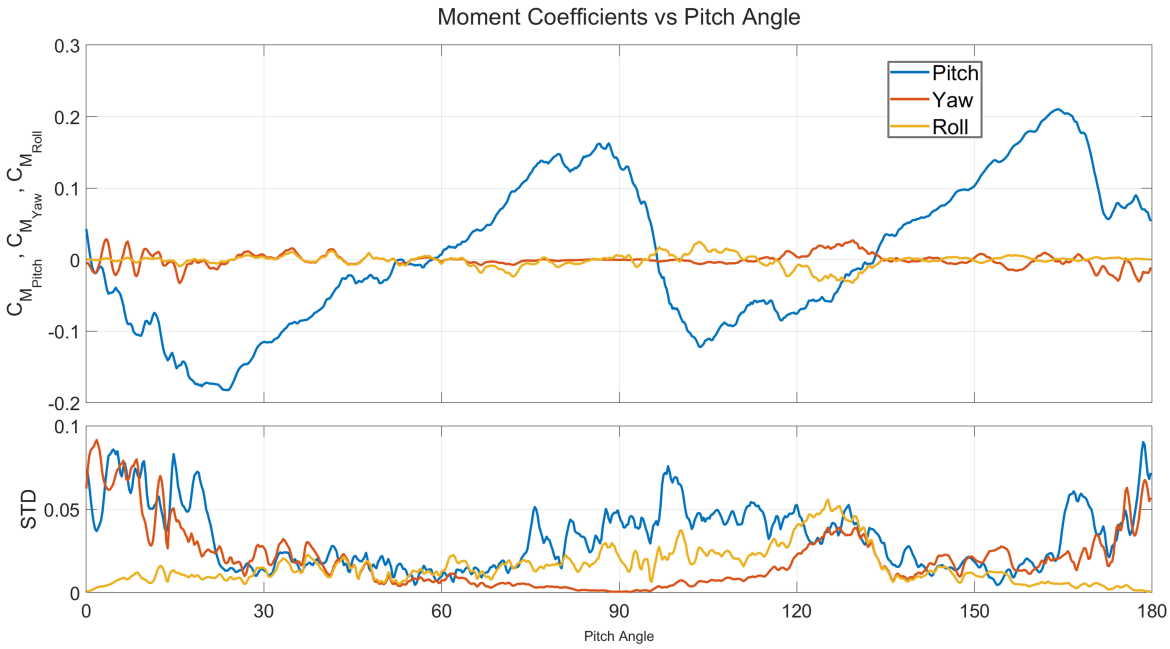

Fig. 34: Dynamic LES Pitch, Yaw, and Roll Moment Coefficients vs Pitch Angle

6.2 MSBS RESULTS

The full data is available in Appendix B for the range of runs outlined in Section 3.2. The coil currents were converted into forces using calibration parameters previously obtained and then values were nondimensionalized for comparison. Initially, it was attempted to perform data reduction using the same method performed for the rotational LES run as shown in the previous section. This method yielded results which showed little variation with pitch angle as shown in Fig. 35(a). A 3-D plot of the drag coefficient, pitch angle, and time was created to explore the results further as seen in Fig. 36. There is a large amplitude shift in the drag force as the rotation switches directions on each oscillation. To properly characterize the values over a range of pitch angles, averages were conducted using clockwise oscillating components and counter-clockwise components separately (Fig. 35(b) & Fig. 35(c)).

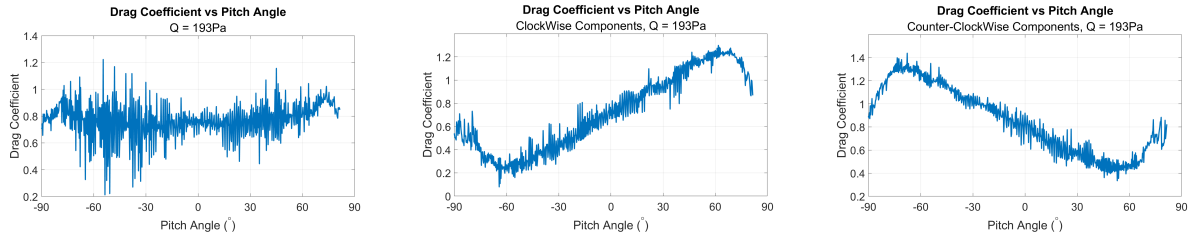

(a) Full Data Set (b) Clockwise Subset (c) Counter-Clockwise Subset

Fig. 35: Drag Coefficient vs Pitch Angle Discretized for the Different Subsets of Data

Low-oscillating runs were captured allowing a $\approx 0°$ pitch drag coefficient to be calculated for comparisons. A run consisting of transition from pitch-oscillation to a tumbling motion at Q = 10Pa was also captured and shown in Fig. 37, with three subsequent data sets collected to record tumbling growth over time. Oscillation frequency was measured in two ways, using a sinusoidal curve-fitting technique and a peak to peak counting method.

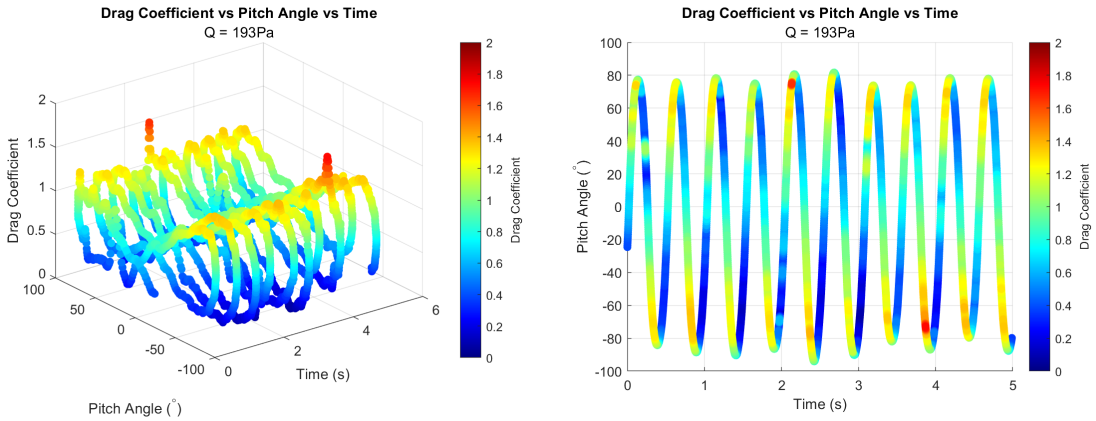

(a) Isometric View

(b) Pitch vs Time View

Fig. 36: Drag Coefficient vs Pitch Angle vs Time for Q = 193Pa

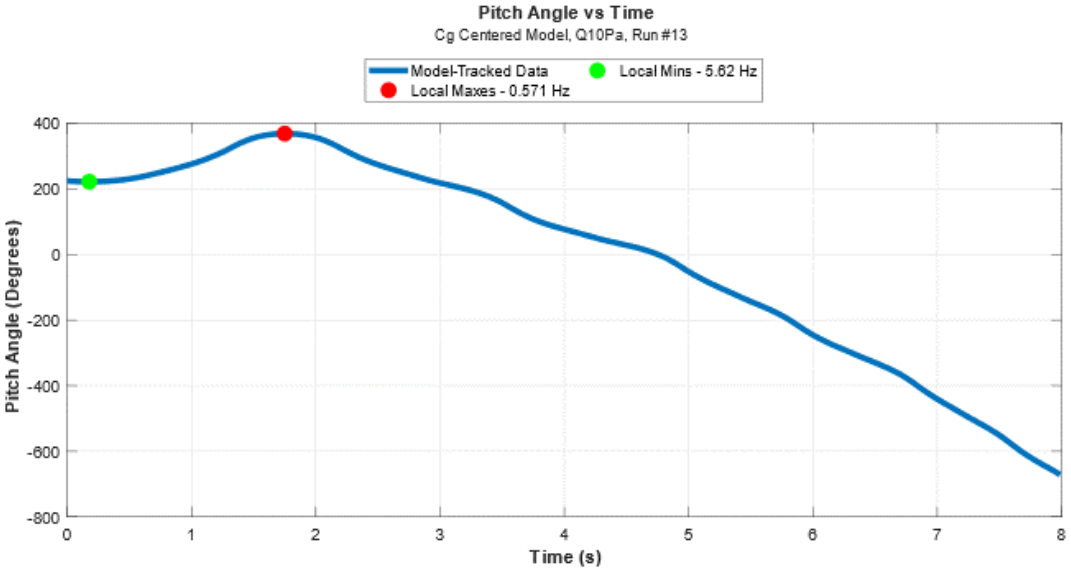

Fig. 37: Transition From Pitch-Oscillation to a Tumbling Motion at Q = 10Pa

CHAPTER 7

COMPARISON OF EXPERIMENTAL AND COMPUTATIONAL RESULTS

Empirical results were collected from literature both recent and historical and are included in comparisons with the results presented in this work. The earliest comparison is to Eiffel's drop testing in 1907 [1] on a cylinder model with a fineness ratio 1, which was dropped from 95m. This data is followed by his wind tunnel testing from 1913 [24], where Eiffel tested two different diameter cylinders both with a fineness ratio of 1. Eiffel's data was converted from the "K" air resistance coefficient to the modern drag coefficient for comparison. The next dataset is from Roberson's wind tunnel comparison of turbulent and non-turbulent flow conditions on blunt body drag [25]. Also included is a group of empirical comparison data from recent tests performed in the Tohoku University MSBS wind tunnel [7, 26]. All the aforementioned data collected, present drag coefficients at 0° pitch angle for a fineness ratio of 1. The last reference is from Prosser and Smith's work in 2015 on LES studies of yawing cylinders [27]. This study gives comparison data for 0° to 90° pitch angle of drag, lift, and pitching moment coefficients. Prosser's work uses yaw rather than pitch and 90° representing axial flow rather than 0° in this thesis. These factors where acceptable for comparison due to symmetry with notation being the only difference. Lastly, it is worth noting that Prosser uses $L \cdot D$ as reference area which was converted to the $\pi(D/2)^2$ reference area used for our coefficients.

The resulting drag, lift, and pitching moment charts with empirical data is shown in Fig. 38, Fig. 39, and Fig. 40 respectively. All results can be seen in Appendix D.

At 0° angle of attack the cylinder is consistent in lift and pitching moment across tests, simulations, and empirical whereas drag coefficient has a wider range of values. The results presented here are not corrected for blockage effects which can produce lower than expected drag numbers, particularly in the MSBS case where blockage ratio is much higher. Dynamic LES, ODU wind tunnel, and Static LES runs show comparable drag numbers with the 0° empirical data.

When the model pitches and the flat face begins to be subject to windward forces, a lift and pitching moment are produced in the opposite direction. This results in a negative lift curve slope at small angles until 10°, which is consistent with Prosser and Smith's results. The MSBS lift data is much less responsive to the flow changes; however, the sign of the lift curve is the same. Drag in this region is consistent across static tests and the dynamic LES test with a loss of drag until 10° pitch angle.

At 10°, the flow visualization results show the trailing edge reattachment occurs. This event coincides with changes in trends of the forces on the model. From 10° to around 30° the lift slope is nearly opposite that of the 0 to 10° range in this work's static results as well as Prosser and Smith's results. Drag begins to increase in all of the results of this work; however, empirical data does not show any change in drag until 20° angle of attack. The dynamic LES results begin to shift away from the static results at this point, with the lift slope not changing until closer to 20° much like Prosser and Smith's results.

Between approximately 30 and 55° the features of the model results change again, with a

leveling out of lift and drag forces as the flow becomes more symmetric and the crossing of the 0 pitching moment plane. With the flat face near to 45° and the loss of windward separation, drag changes slope resulting in a maximum drag at a orientation in this range. Prosser and Smith's maximum drag was at 0°, with 30° being a close second for the $Re = 0.96e05$ run. RANS had maximum drag at 30°, ODU wind tunnel at 50°, static LES at 45°, and dynamic LES at 42°.

Empirical, dynamic and static LES, and static ODU tests suggest a sharp drop off in drag after some flow point past the 45° mark, although the angle at which this happens varies across the tests. The Lift curve shows a sharp change past 60° for the higher resolution tests, suggesting a potential flow regime point of interest in this region .

As the curved face is subjected to more windward forces, the flow becomes less axisymmetric than before and the results in this area grow more uncertain. The lift curve changes sign multiple times in this region in both the RANS, dynamic LES, and empirical data.

The tumbling effects are driven by the pitching moment and there are anti-symmetries present in the results presented. The pitching moment curve has the change in slope back towards zero close to 75° for most cases presented. The dynamic LES results near 90° seem to have incorporated a lagging effect where the flow effects have yet to take full effect at that angle of attack.

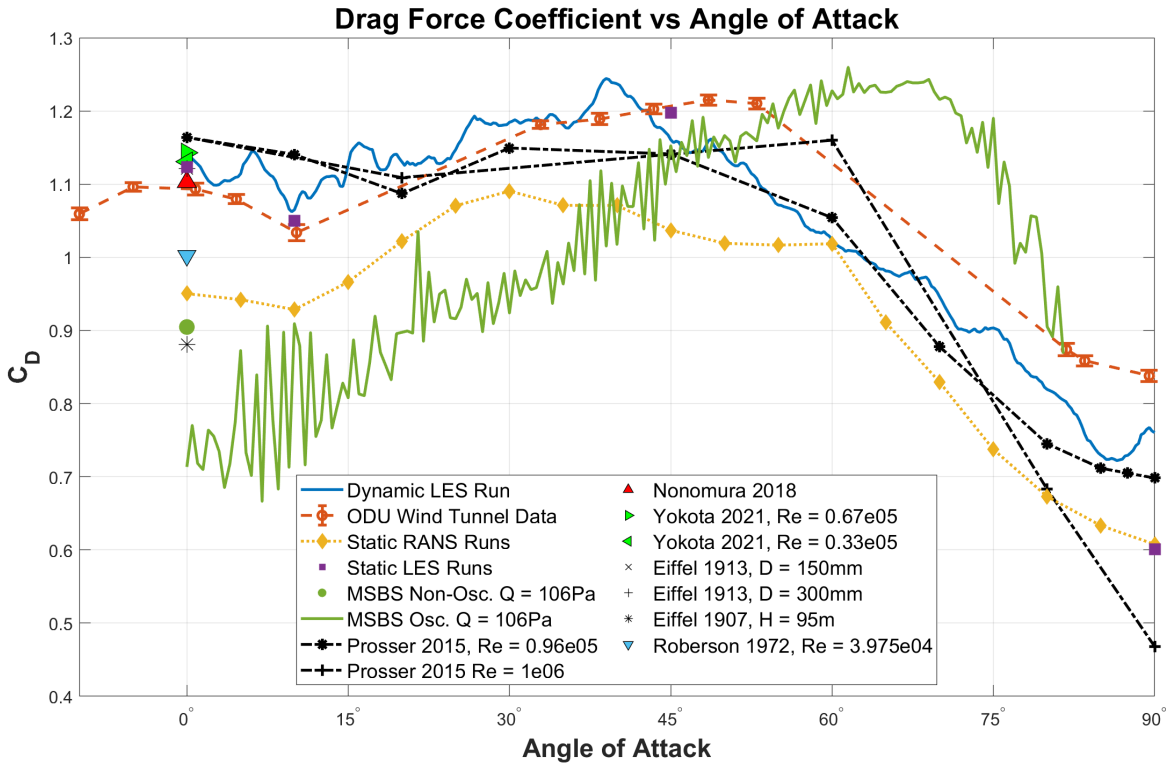

Fig. 38: Drag Coefficients for Empirical Data and the Tests Performed in This Work

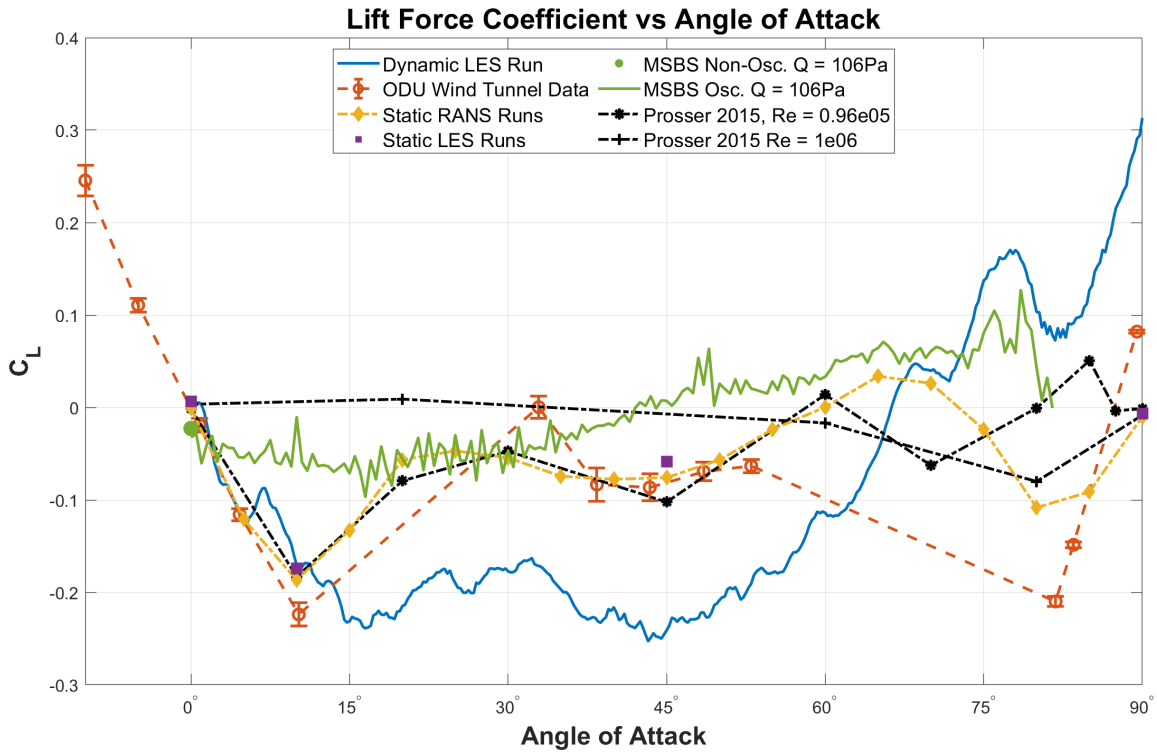

Fig. 39: Lift Coefficients for Empirical Data and the Tests Performed in This Work

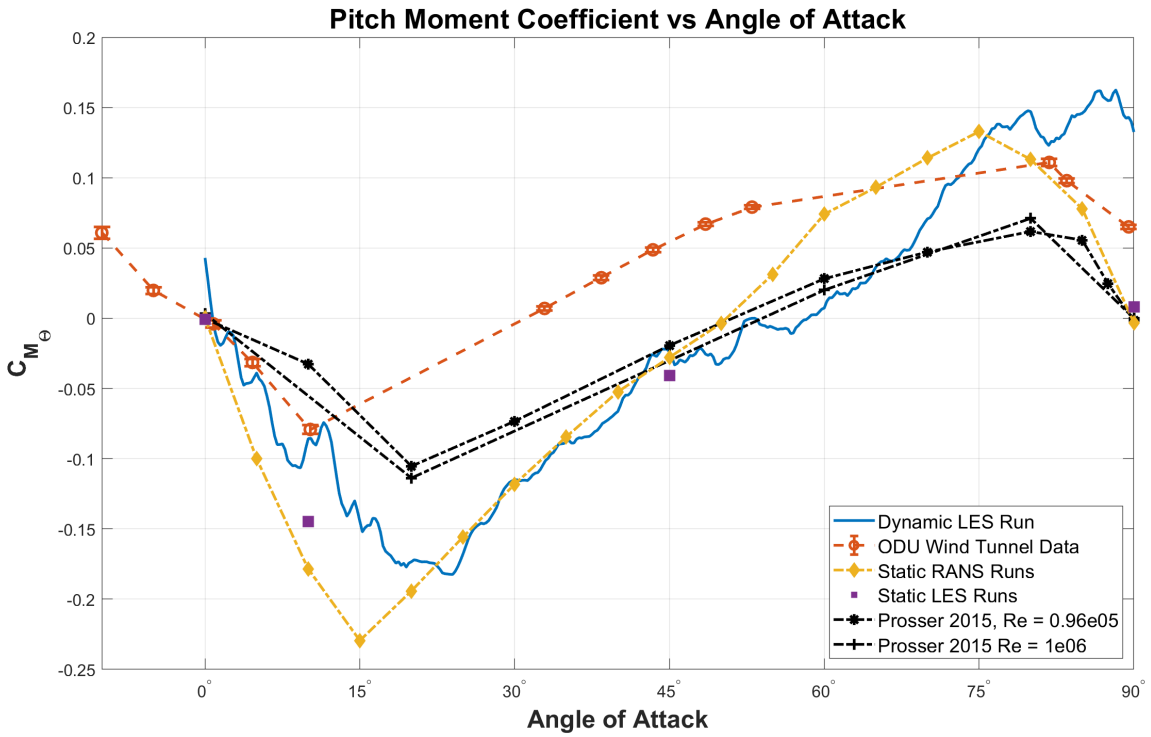

Fig. 40: Pitch Moment Coefficients for Empirical Data and the Tests Performed in This Work

CHAPTER 8

CONCLUSIONS

In this work, significant progress has been made to enhance the current state of knowledge surrounding low-fineness-ratio cylinders' aerodynamics. Previous empirical studies have focused on fineness ratio, with little attention being paid to pitch angle variation. A set of experiments and computational runs on a fineness-ratio 1 cylinder, consisting of static force and moment wind tunnel testing, PIV testing, RANS and LES static computations, LES rotating computations, and MSBS dynamic wind tunnel testing were performed. The results of these efforts were compared both between tests and with historical data for pitch rotation between 0° and 90°. Quantitative results displayed agreement in trends for drag, lift, and pitching moment coefficients between various cases. Flow field visualizations demonstrated reasonable agreement between RANS, LES, and PIV tests for four distinct flow structures. The efforts herein greatly improve the quantity of data points for low-fineness-ratio cylinders at angles greater than 0° and less than 90°, as these orientations have been scarcely inspected before.

Effort remains to improve connections made in static tests, to the tumbling phenomenon observed during dynamic testing. The unsteady flow field and coupling of torque and rotational drag on tumbling cylinder data introduces extra complexity to the results, requiring a finer approach for validation. More dynamic testing would be advantageous to tying the dynamic and static data together as well as 1-DOF CFD testing allowing a fluid dynamic simulation of MSBS testing to occur. There is higher discrepencies of the data presented

from the 45° to 90° angle of attack cases, most likely from the loss of flow symmetry that occurs once the majority of the windward surface becomes curved rather than flat. This angle range would be advantageous to study more statically, in particular with flow visualization. The 3D effects propose difficulties with this endeavor so careful consideration of methods would be necessary, stereo PIV would be particularly useful.

In terms of an analytical approach to the tumbling problem, a potential avenue of exploration could be the study of tumbling plates which has been explored for decades. The low-fineness-ratio cylinder from the blunt body perspective could be seen as a very high-fineness-ratio circular plate from the tumbling studying aerodynamicists' perspective.

REFERENCES

[1] G. Eiffel, "Recherches expérimentales sur la résistance de l'air," tech. rep., La Société Des Ingénieurs Civils De France, 1907.

[2] H. J. Allen and A. J. E. Jr., "A study of the motion and aerodynamic heating of ballistic missiles entering the earth's atmosphere at high supersonic speeds," *Forty-Fourth Annual Report of the NACA*, 1958.

[3] C. P. Britcher and M. Schoenenberger, "Feasibility of dynamic stability measurements of planetary entry capsules using a magnetic suspension and balance system," in *32nd AIAA Aerodynamic Measurement Technology and Ground Testing Conference*, June 2016.

[4] T. A. Dukes and R. N. Zapata, "Magnetic suspension with minimum coupling effects for wind tunnel models," *IEEE Transactions on Aerospace and Electronic Systems*, vol. AES-1, no. 1, pp. 20–28, 1965.

[5] H. M. Parker, "Theoretical and experimental investigation of a three.dimensional magnetic-suspension balance for dynamic-stability research in wind tunnels.," *Semi-annual Status*, no. 1, p. 47, 1966.

[6] T. Stephens, "Design, construction, and evaluation of a magnetic suspension and balance system for wind tunnels," Tech. Rep. CR-66903, Massachusetts Institute of Technology, November 1969.

[7] T. Nonomura, K. Sato, K. Fukata, H. Nagaike, H. Okuizumi, Y. Konishi, K. Asai, and H. Sawada, "Effect of fineness ratios of 0.75–2.0 on aerodynamic drag of freestream-aligned circular cylinders measured using a magnetic suspension and balance system," *Experiments in Fluids*, vol. 59, 2018.

[8] K. Shinji, H. Nagaike, T. Nonomura, K. Asai, H. Sawada, Y. Konishi, and H. Okuizumi, "Aerodynamic characteristics of axial circular cylinders with low fineness ratios between 0.5 and 0.75 using a magnetic suspension and balance system," in *AIAA SciTech Forum*, January 2019.

[9] K. Shinji, H. Nagaike, T. Nonomura, K. Asai, H. Okuizumi, Y. Konishi, and H. Sawada, "Aerodynamic characteristics of low-fineness-ratio freestream-aligned cylinders with magnetic suspension and balance system," in *AIAA Technical Notes*, vol. 58 no.8, August 2020.

[10] T. D. Schott and D. E. Cox, "Operational experience with the electromagnetic position sensor (eps) for the nasa 6-inch msbs," in *AIAA Scitech 2021 Forum*, January 2021.

[11] Software Cradle Co, *Multiphysics Computational Fluid Dynamics Solution Product Brochure*, 2022.

[12] H. Lübcke, S. Schmidt, T. Rung, and F. Thiele, "Comparison of les and rans in bluff-body flows," *Journal of Wind Engineering and Industrial Aerodynamics*, vol. 89, 2001.

[13] J. G. Knudsen and D. L. Katz, *Fluid Dynamics and Heat Transfer*. McGRAW-HILL Book Company, Inc., 1958.

[14] C. F. Heddleson, D. L. Brown, and R. T. Cliffe, "Summary of drag coefficients of various shaped cylinders," tech. rep., Aircraft Nuclear Propulsion Department General Electric, 1957.

[15] J. C. McFall Jr., "Dynamic stability investigation of two right circular cylinders in axial free flight at mach numbers from 0.4 to 1.7," Tech. Rep. RM L56L28, National Advisory Committee For Aeronautics, 1957.

[16] R. D. Klett, "Drag coefficients and heating ratios for right circular cylinders in free-molecular and continuum flow from mach 10 to 30," Tech. Rep. SC-RR-64-2141, Sandia Laboratory, 1964.

[17] D. E. Randall, "A method for estimating the drag coefficient of a tumbling circular cylinder," Tech. Rep. SC-TM-64-528, Sandia Laboratory, 1964.

[18] H. Nakaguchi, K. Hashimoto, and S. Muto, "An experimental study on aerodynamic drag of rectangular cylinders," *Journal of Japan Society for Aeronautical and Space Sciences*, vol. 16, 1968.

[19] Y. Ohya, "Note on a discontinuous change in wake pattern for a rectangular cylinder," *Journal of Fluids and Structures*, vol. 8, 1994.

[20] E. Baris, C. P. Britcher, and G. Altamirano, "Wind tunnel testing of static and dynamic aerodynamic characteristics of a quadcopter," in *AIAA Aviation Forum*, June 2019.

[21] W. Thielicke and R. Sonntag, "Particle image velocimetry for matlab: Accuracy and enhanced algorithms in pivlab," *Journal of Open Research Software*, vol. 9, 2021.

[22] W. Thielicke, *The Flapping Flight of Birds - Analysis and Application*. PhD thesis, Rijksuniversiteit Groningen, 2014.

[23] J. Roskam, *Airplane Design Part VI: Preliminary Calculation of Aerodynamic, Thrust and Power Characteristics*. Design, Analysis and Research Corporation, 2017.

[24] G. Eiffel, *The Resistance of The Air and Aviation*. Constable & Company LTD, 1913.

[25] J. A. Roberson, C. Y. Lin, G. S. Rutherford, and M. D. Stine, "Turbulence effects on drag of sharp-edged bodies," in *Journal of the Hydraulics Division, Proceedings of the American Society of Civil Engineers*, July 1972.

[26] S. Yokota, T. Ochiai, Y. Ozawa, T. Nonomura, and K. Asai, "Analysis of unsteady flow around an axial circular cylinder of critical geometry using combined synchronous measurement in magnetic suspension and balance system," *Experiments in Fluids*, vol. 62, 2021.

[27] D. T. Prosser and M. J. Smith, "Aerodynamics of finite cylinders in quasi-steady flow," in *AIAA SciTech*, January 2015.

APPENDIX A

PIV RESULTS

A.1 WIDE VIEW 0°, TIME-AVERAGED RESULTS

$|u|$

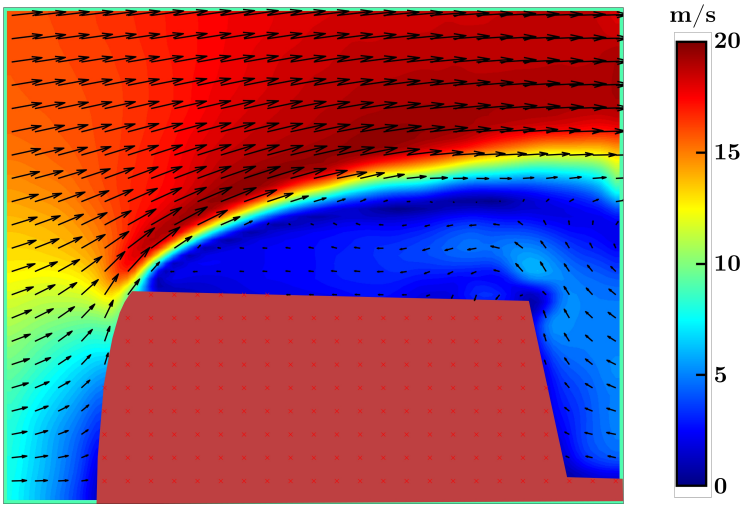

u_x

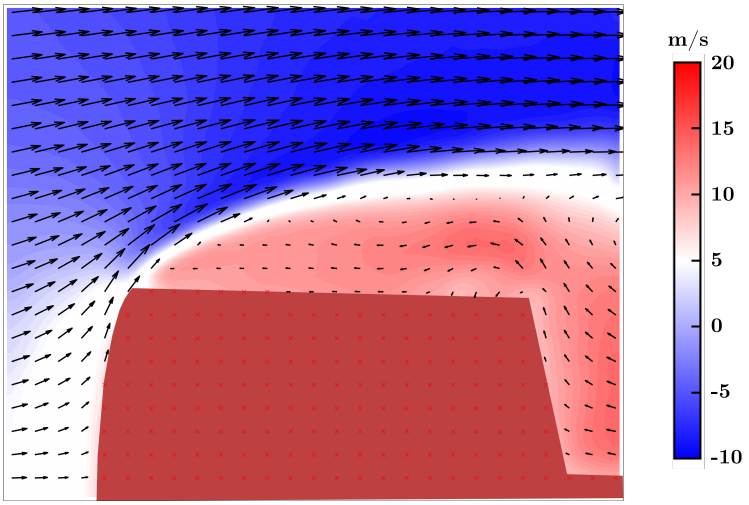

$\overrightarrow{\omega}$

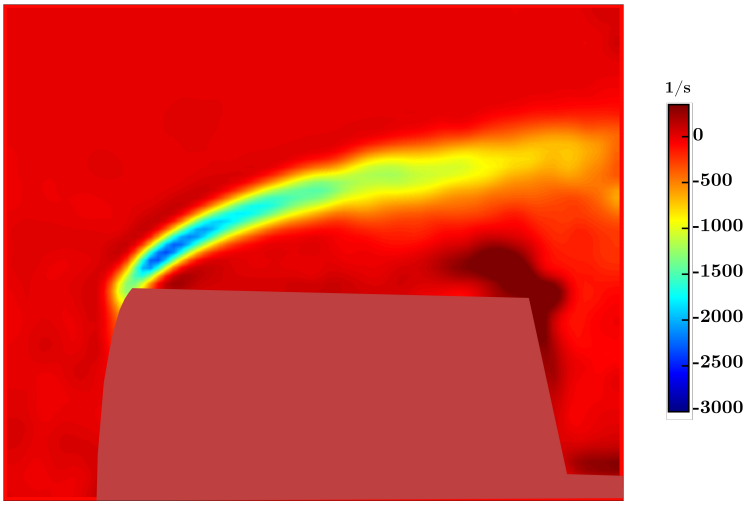

A.2 ZOOM VIEW 0°, TIME-AVERAGED RESULTS

$|u|$

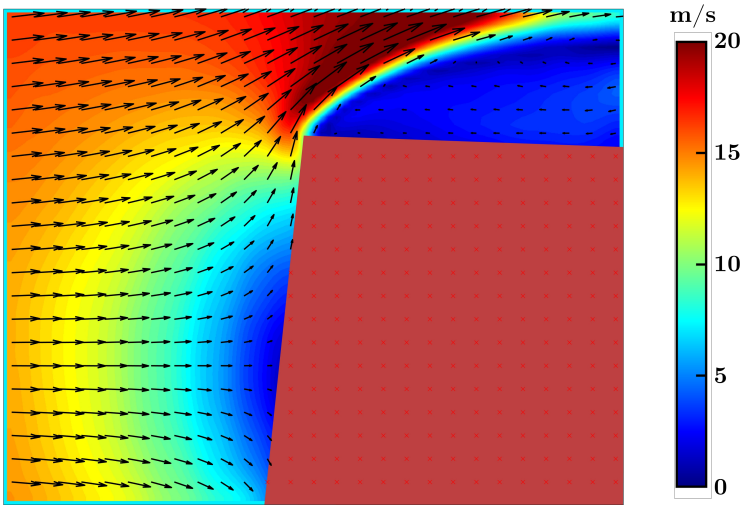

u_x

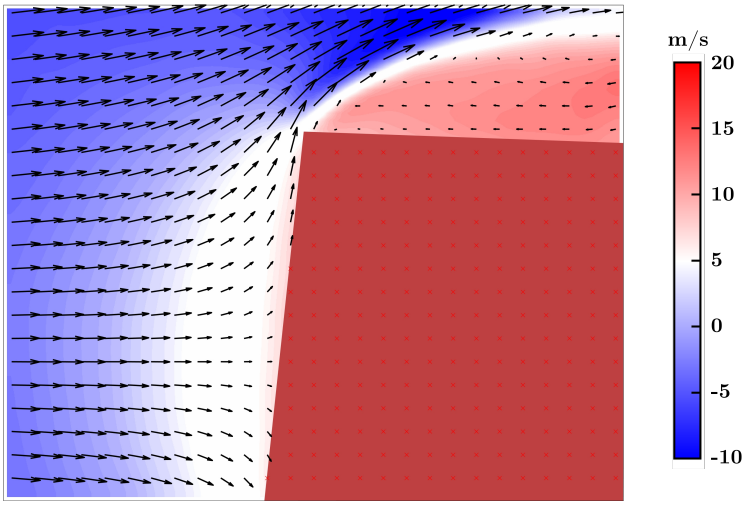

$\overrightarrow{\omega}$

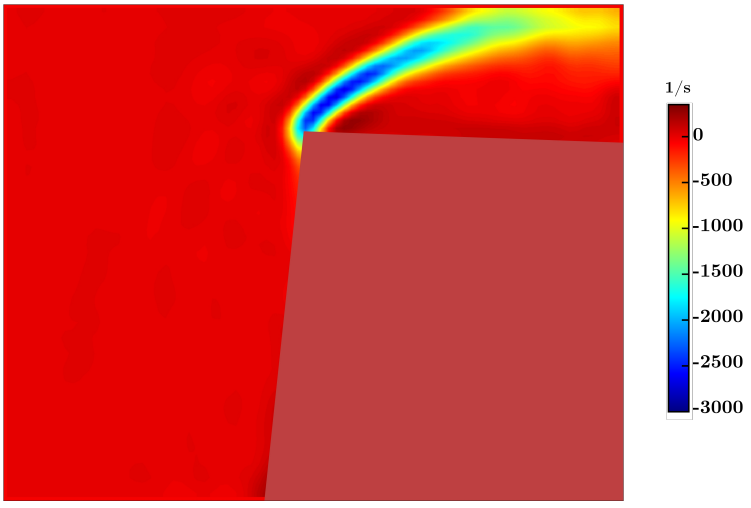

A.3 WIDE VIEW 10°, TIME-AVERAGED RESULTS

$|u|$

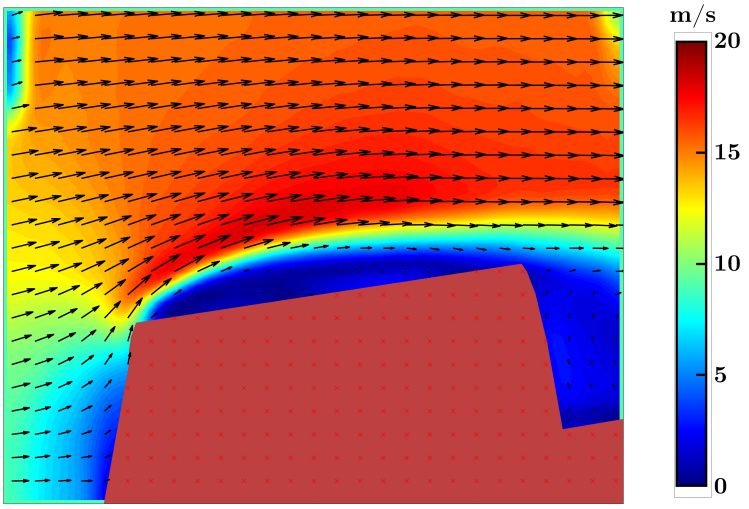

u_x

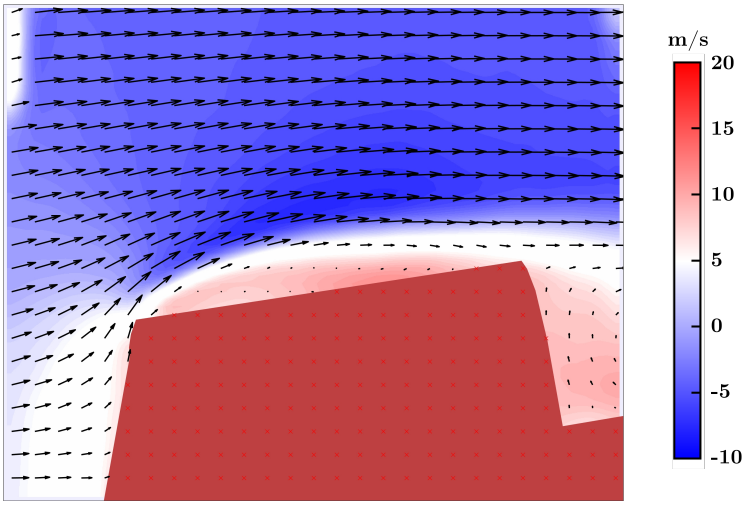

$\overrightarrow{\omega}$

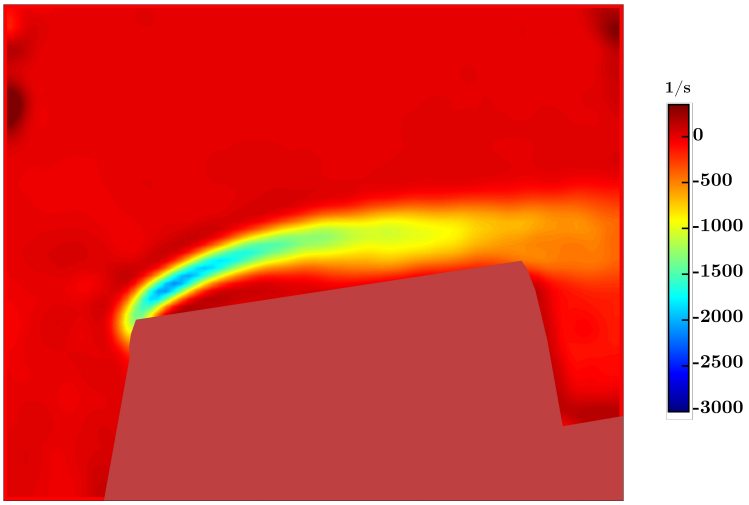

A.4 ZOOM VIEW 10°, TIME-AVERAGED RESULTS

$|u|$

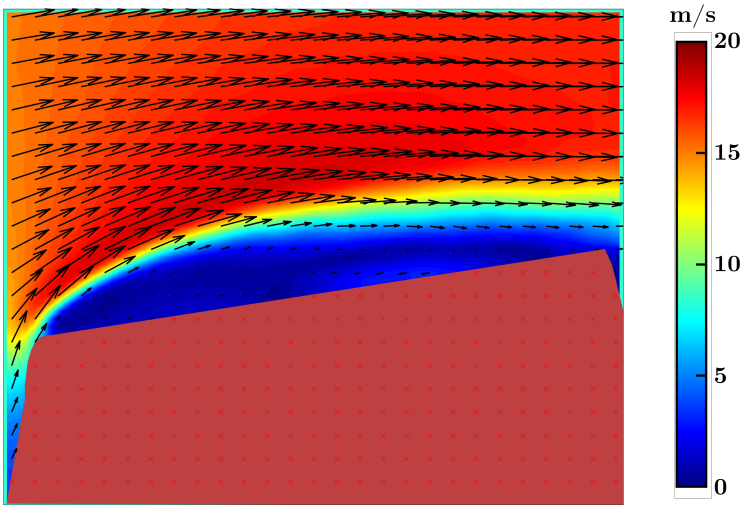

u_x

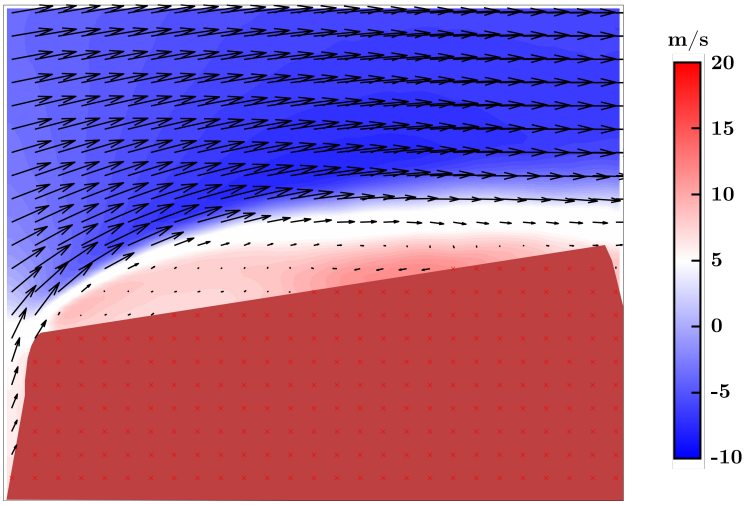

$\overrightarrow{\omega}$

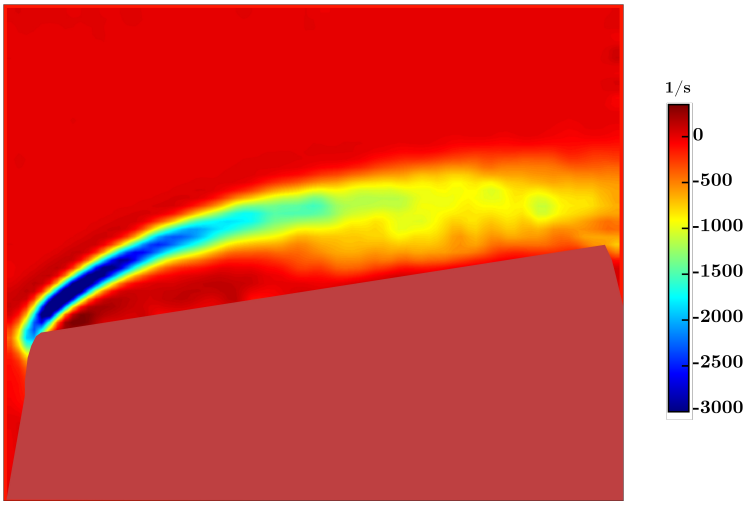

A.5 WIDE VIEW 45°, TIME-AVERAGED RESULTS

$|u|$

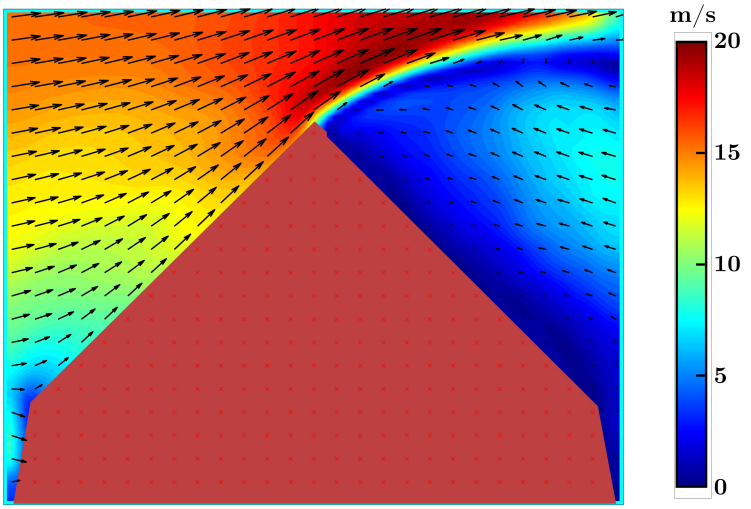

u_x

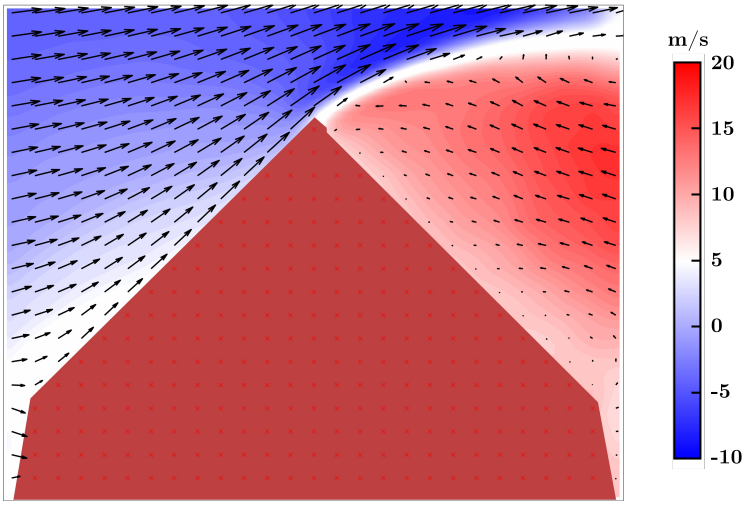

$\overrightarrow{\omega}$

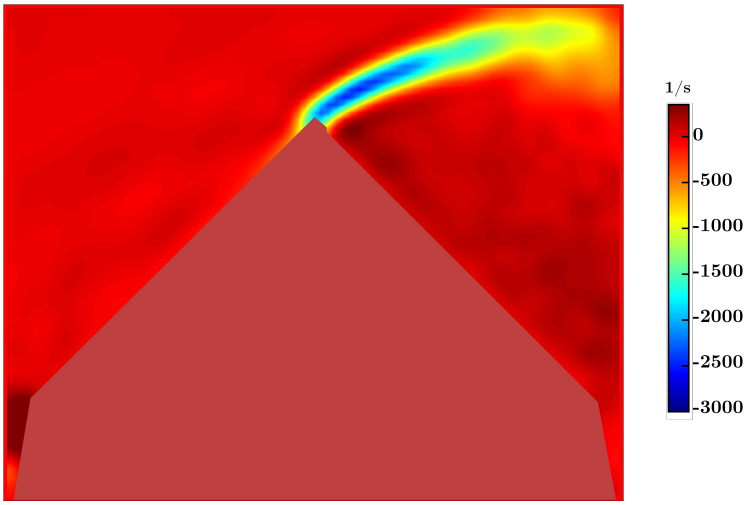

A.6 WIDE VIEW 90°, TIME-AVERAGED RESULTS

$|u|$

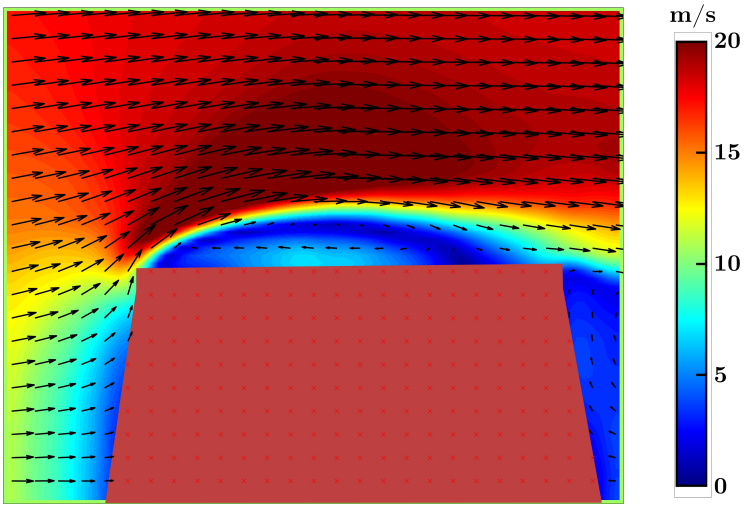

u_x

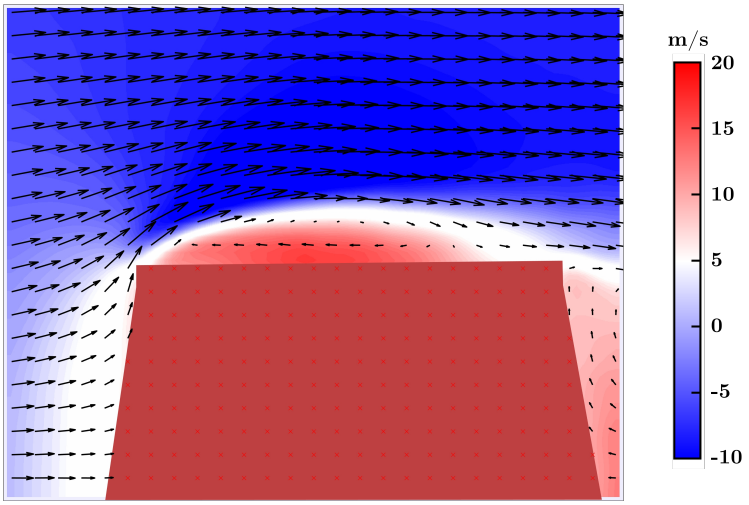

$\overrightarrow{\omega}$

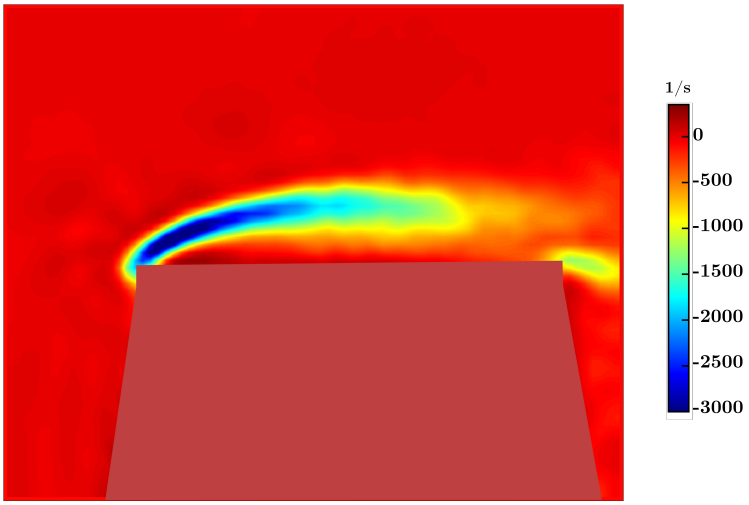

APPENDIX B

MSBS C_G - FORWARD RESULTS

B.1 RUN00: Q = 0PA

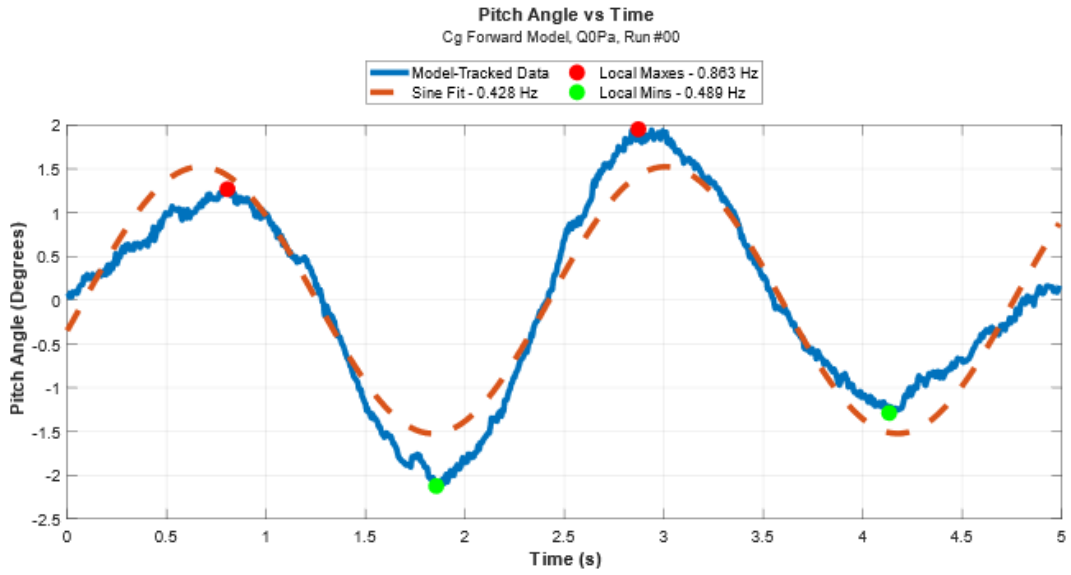

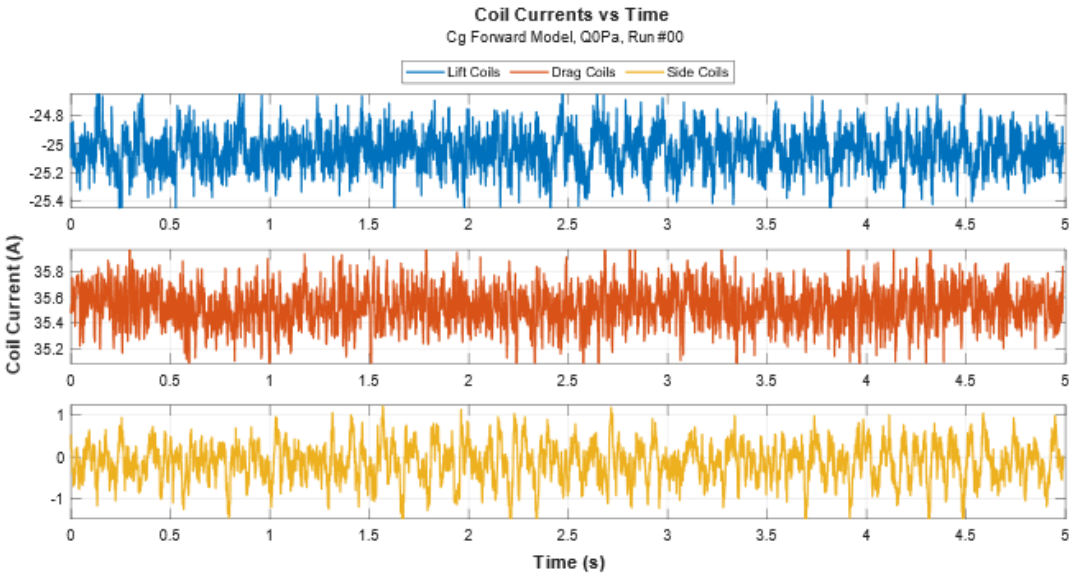

B.2 RUN02: Q = 106PA

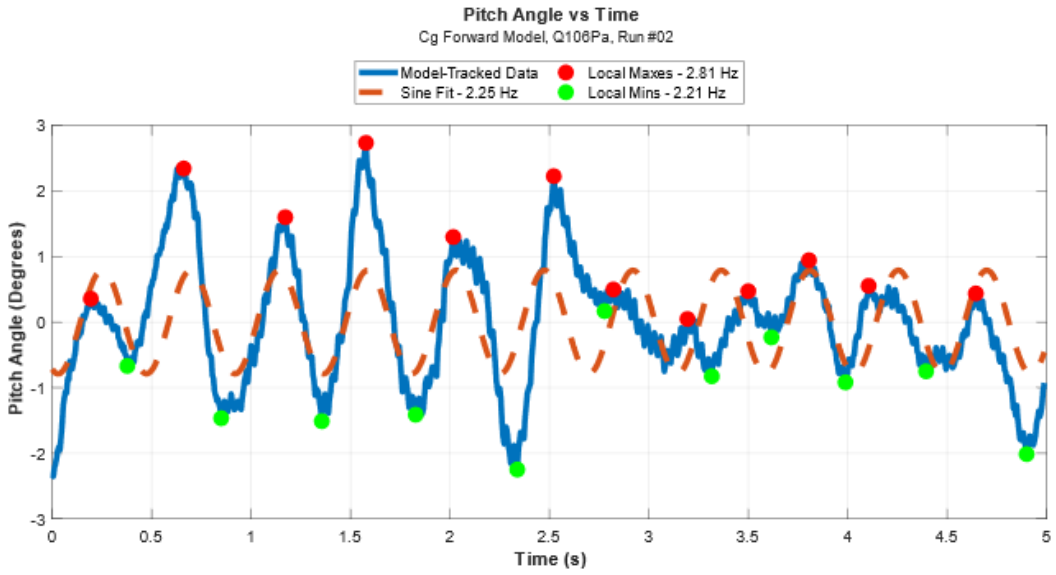

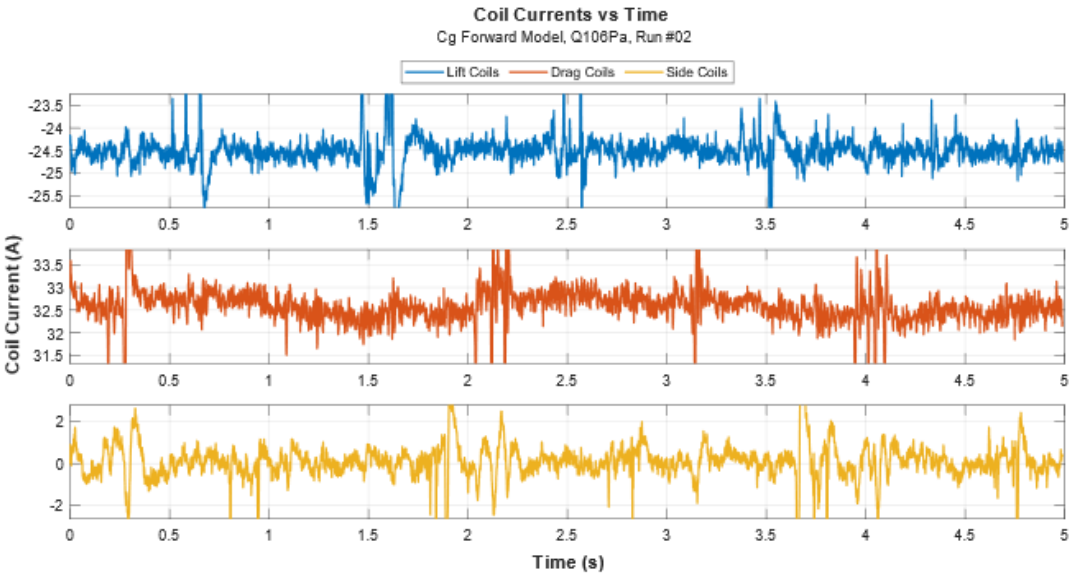

B.3 RUN04: Q = 194PA

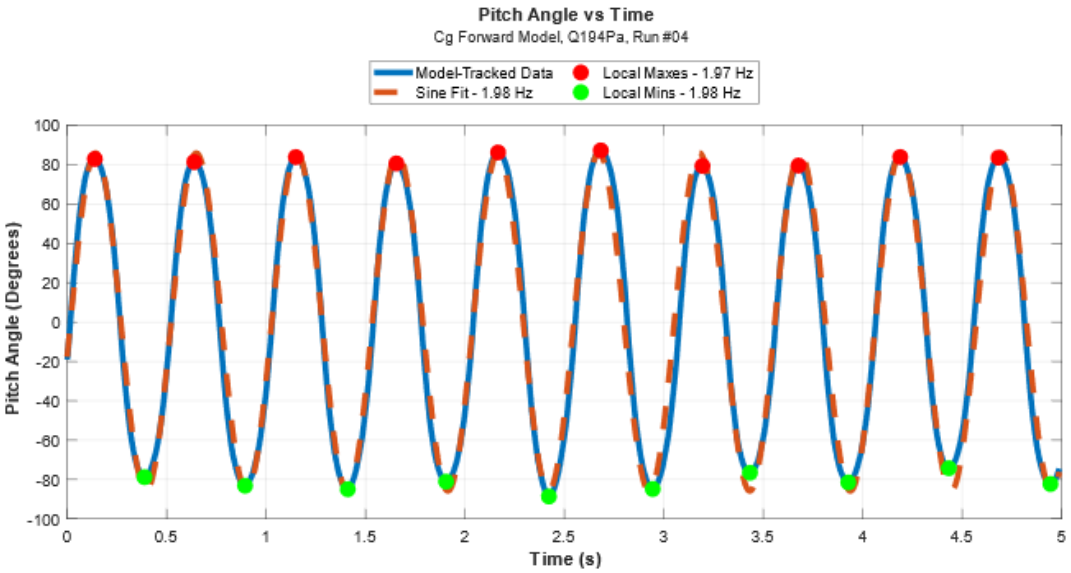

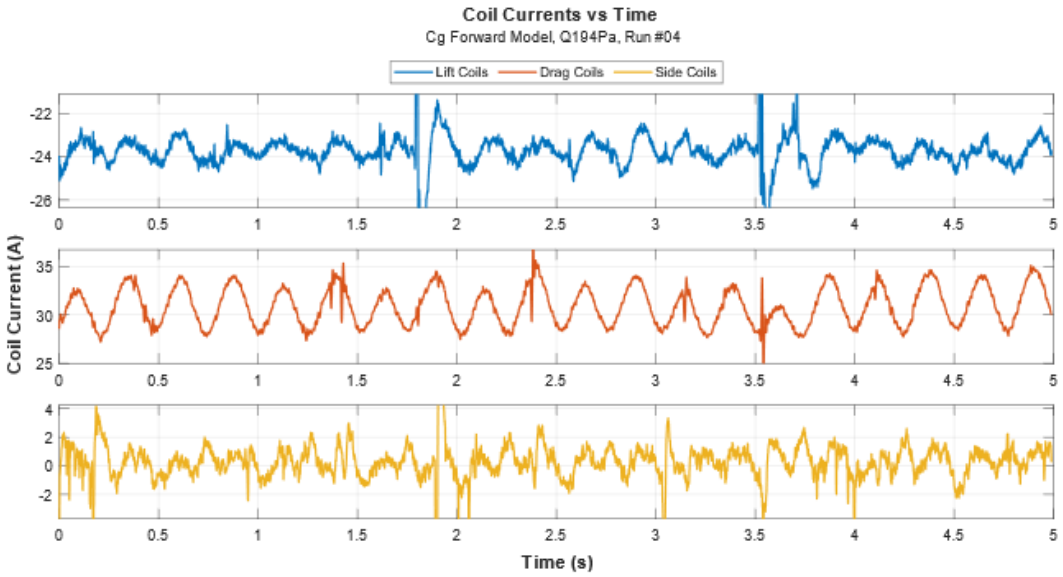

B.4 RUN05: Q = 45PA

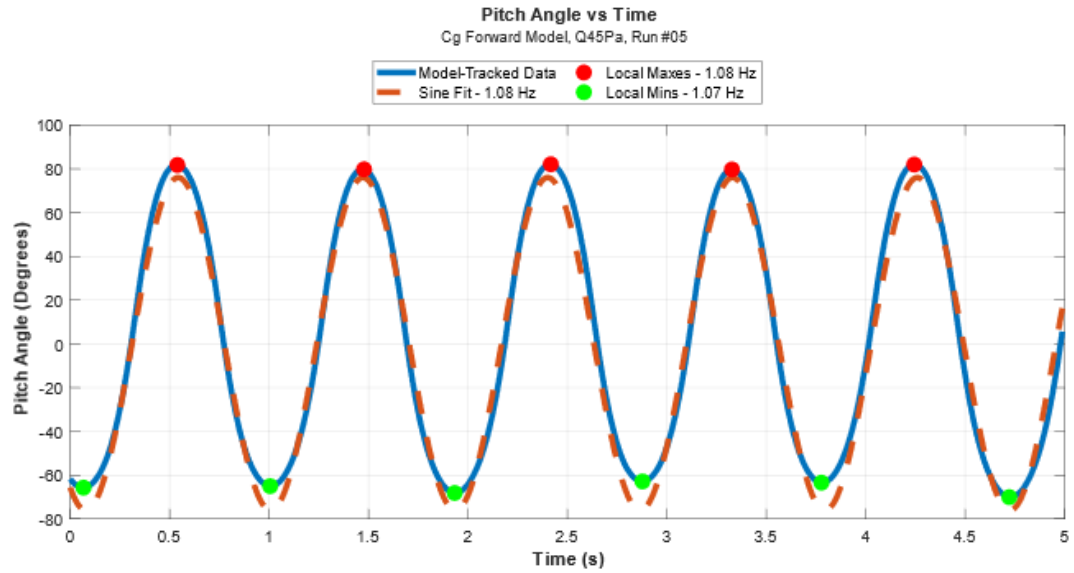

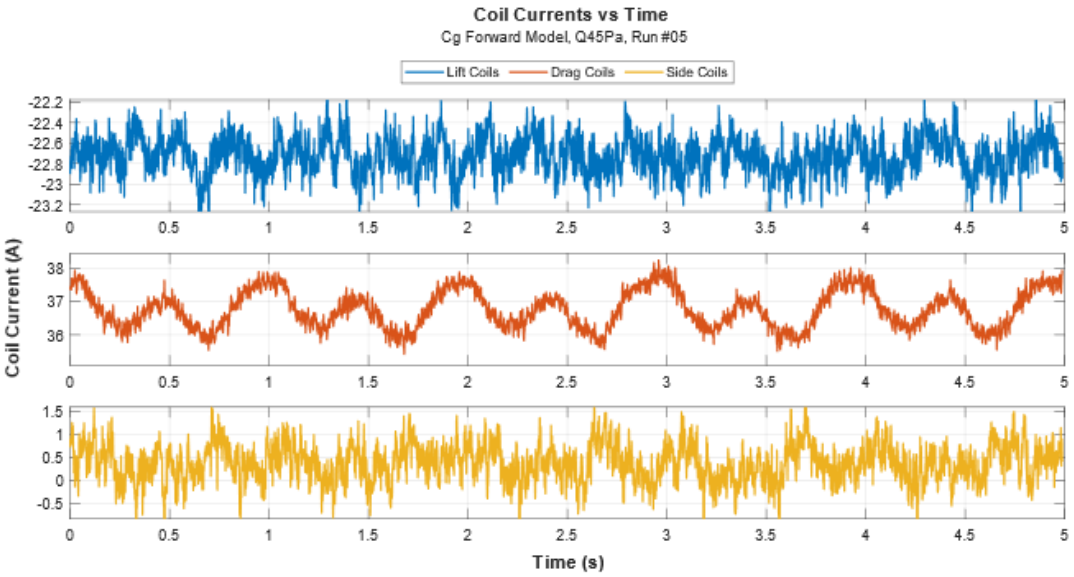

B.5 RUN06: Q = 106PA

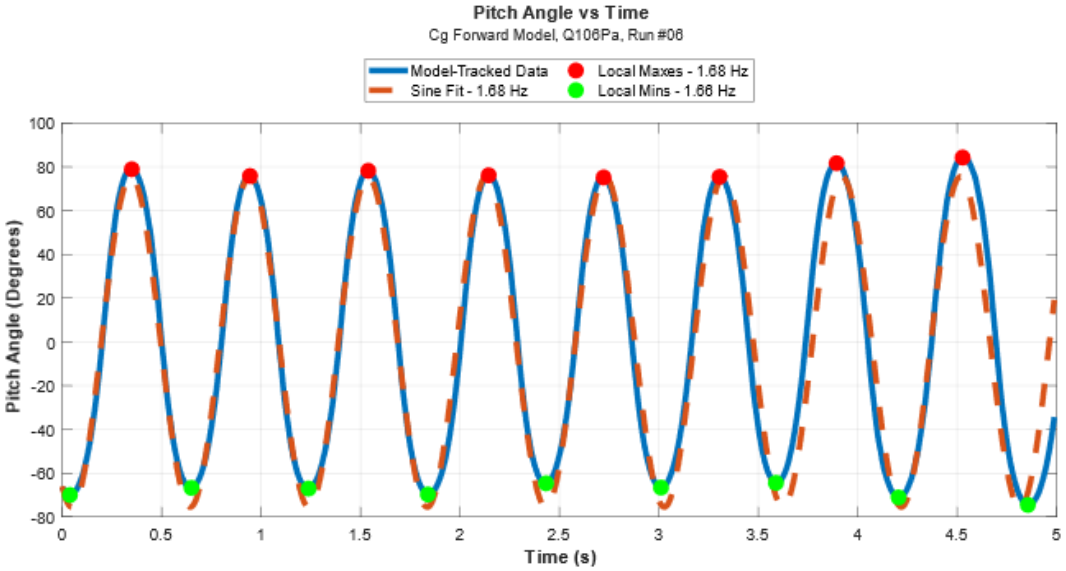

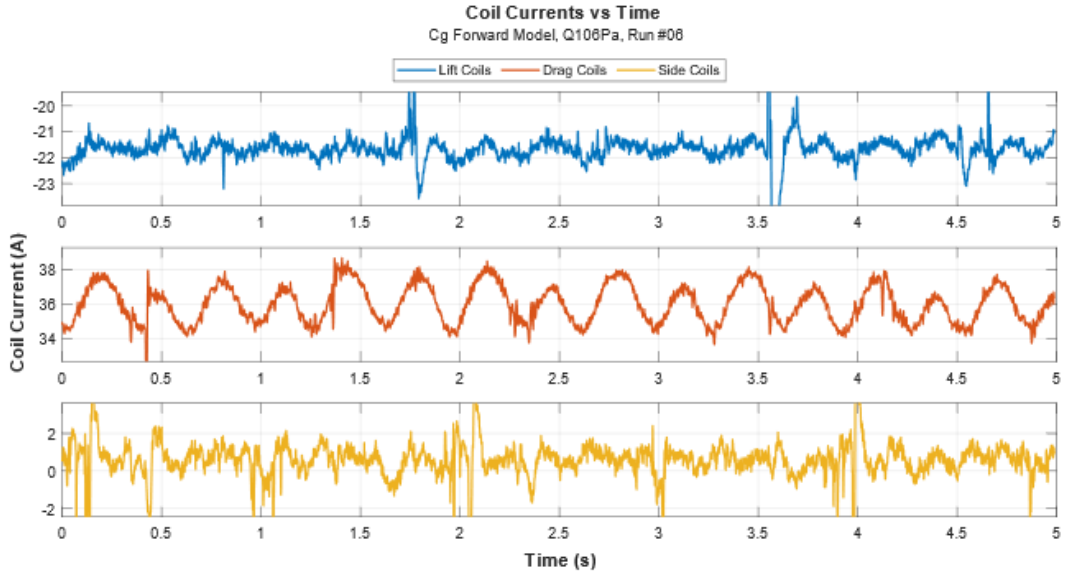

B.6 RUN07: Q = 192PA

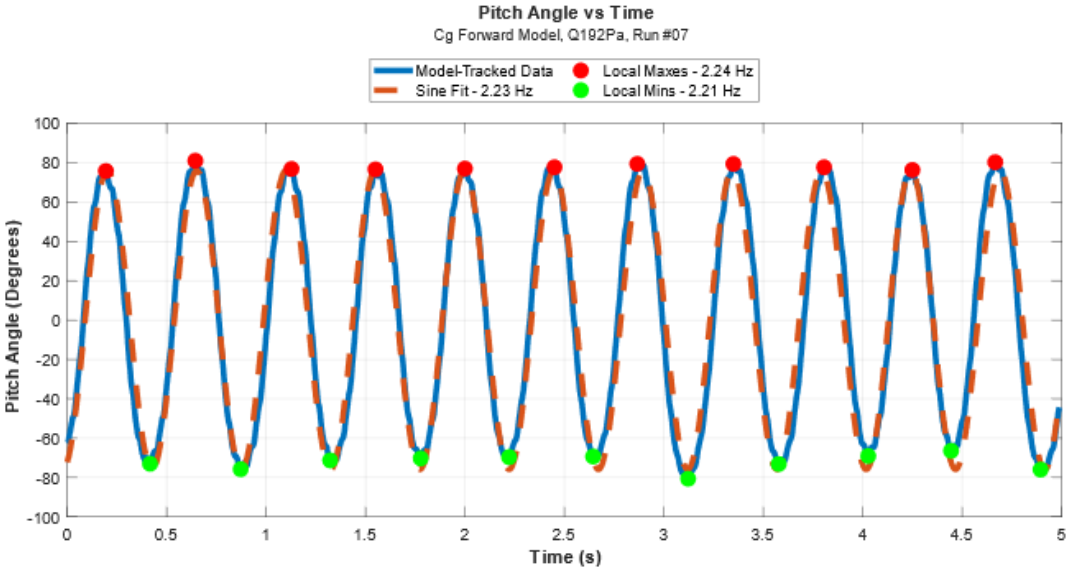

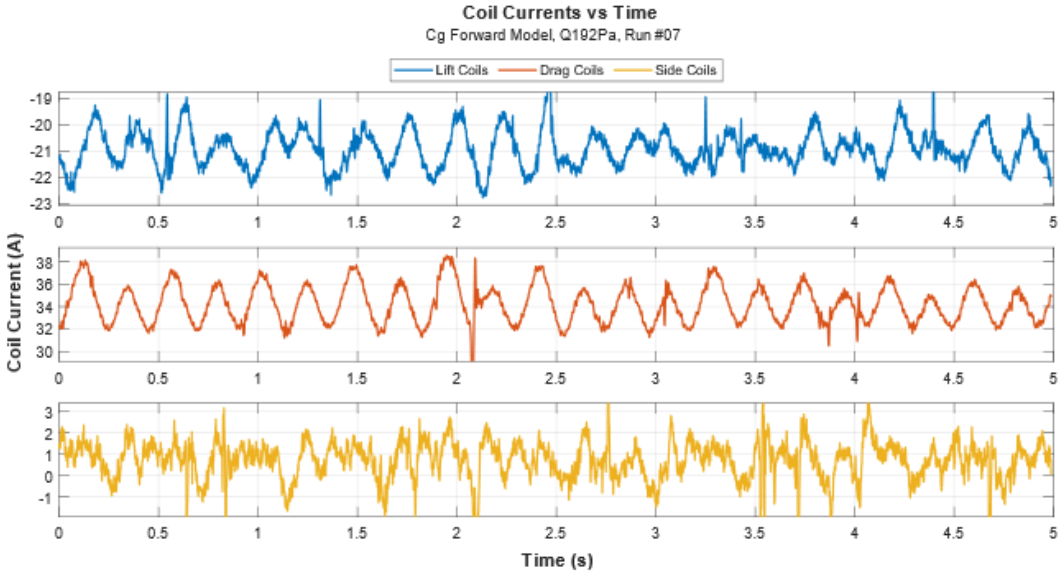

APPENDIX C

MSBS C_G - CENTERED RESULTS

C.1 RUN10: Q = 0PA

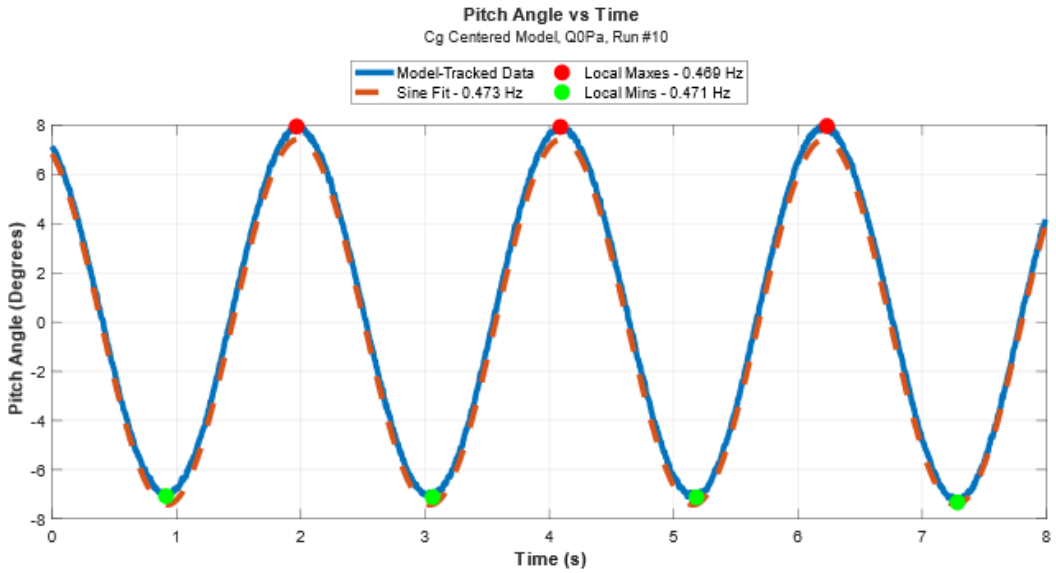

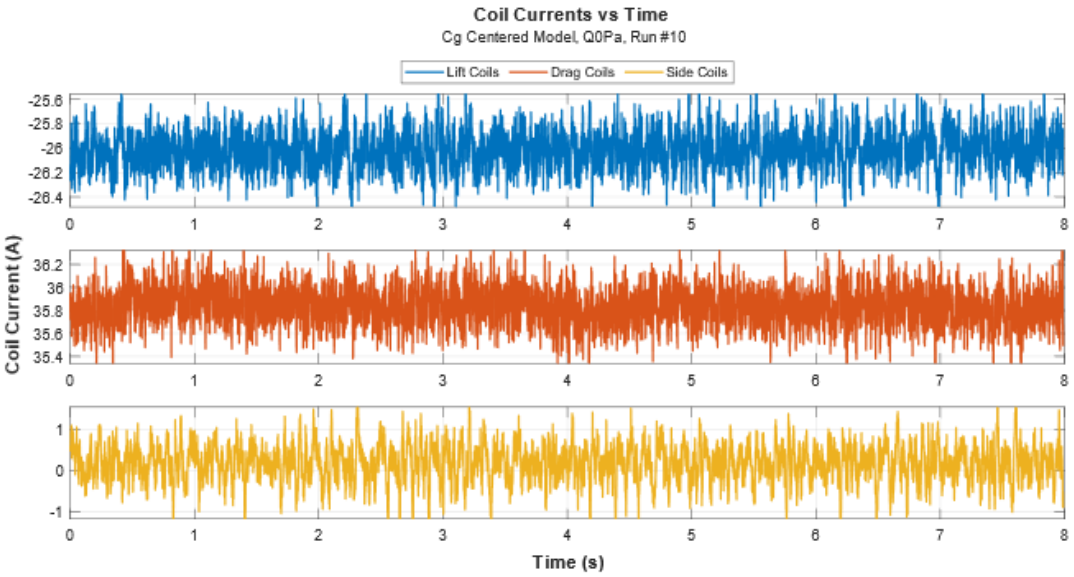

C.2 RUN12: Q = 0PA

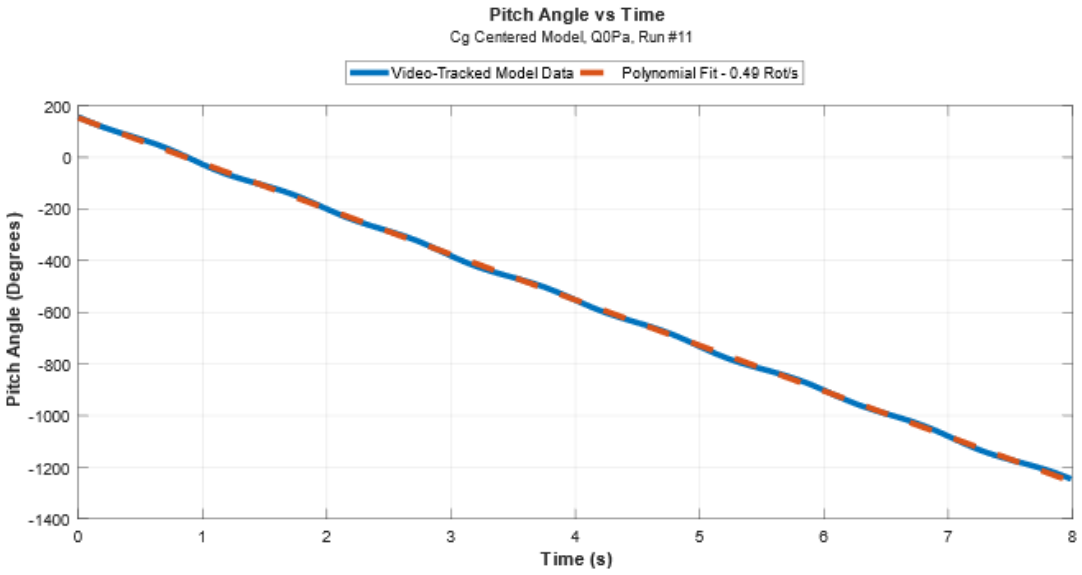

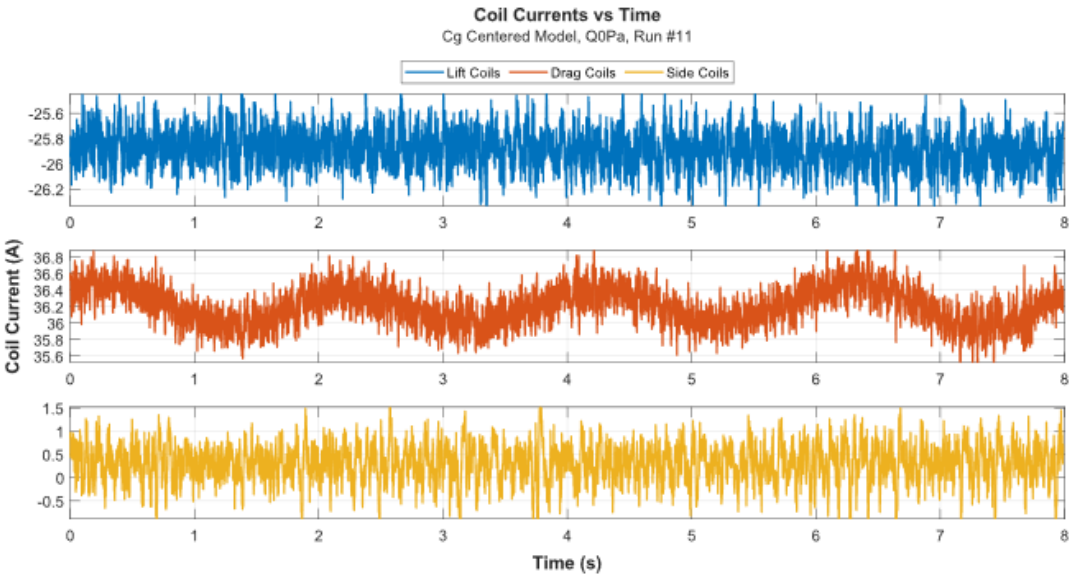

C.3 RUN13: Q = 10PA

C.3.1 FULL RUN

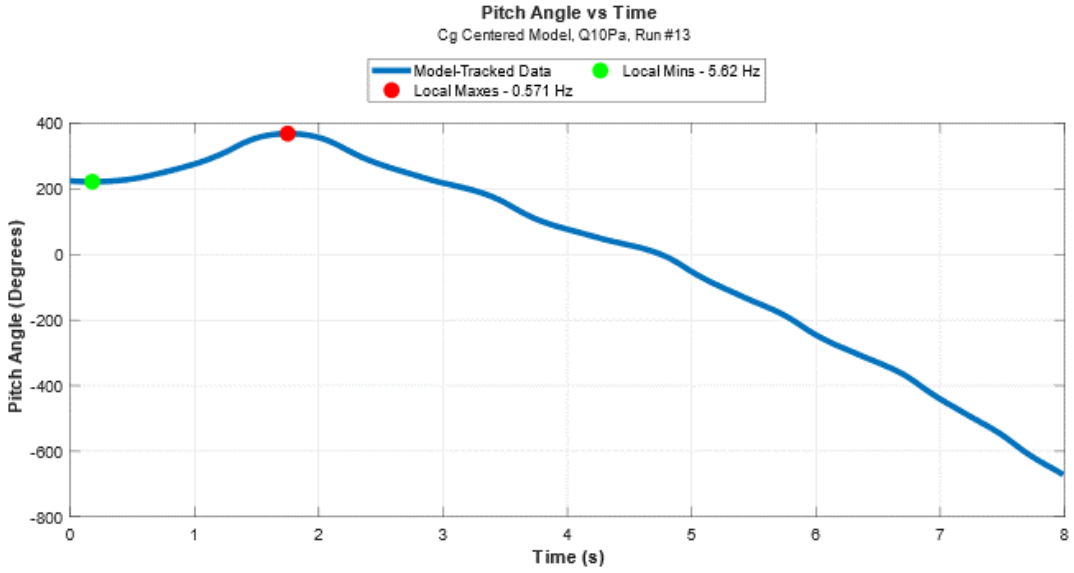

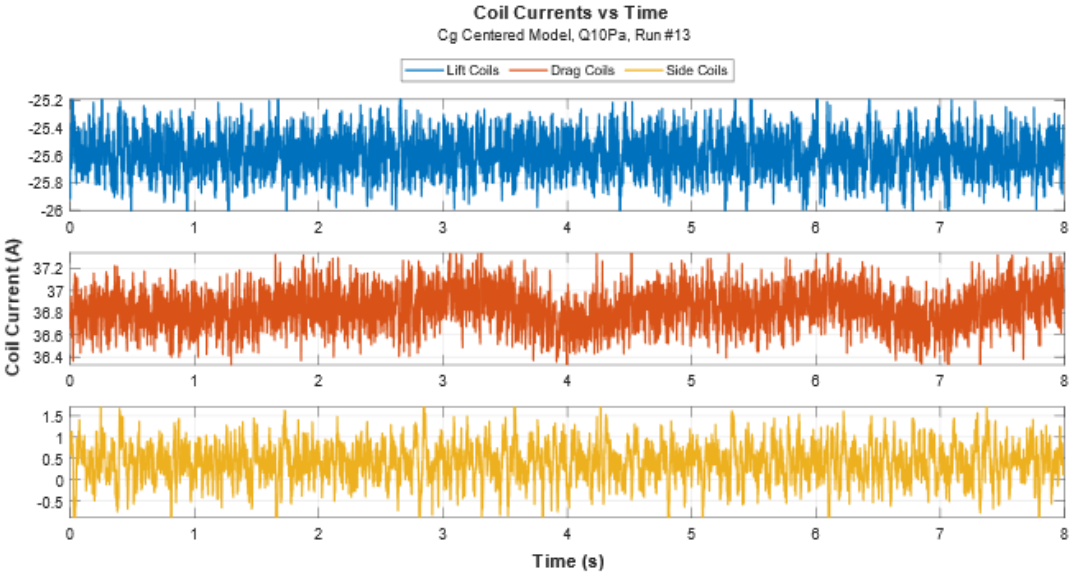

C.3.2 OSCILLATING COMPONENT OF RUN, T = 0S - 2.5S

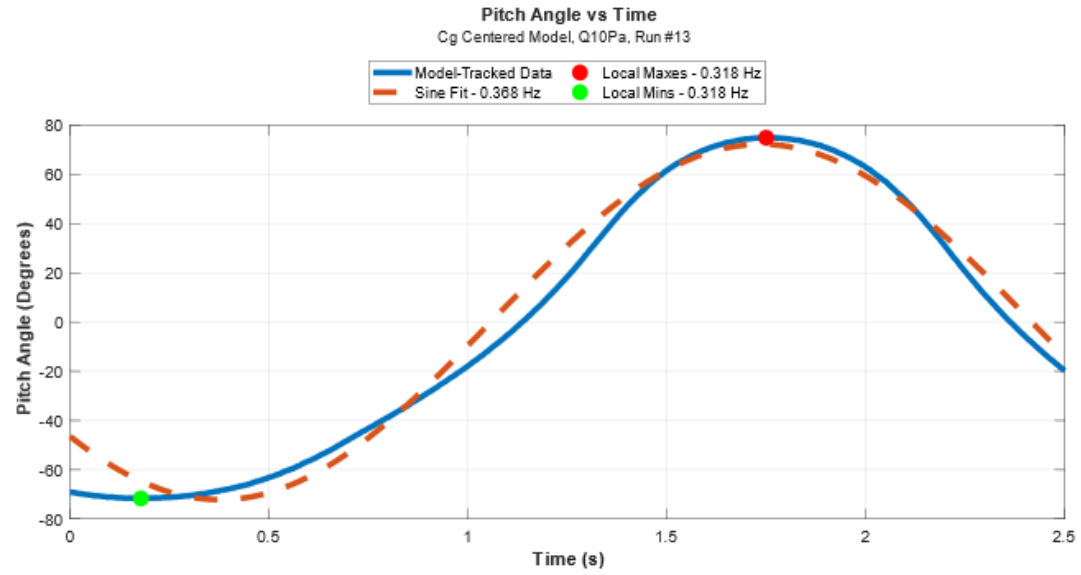

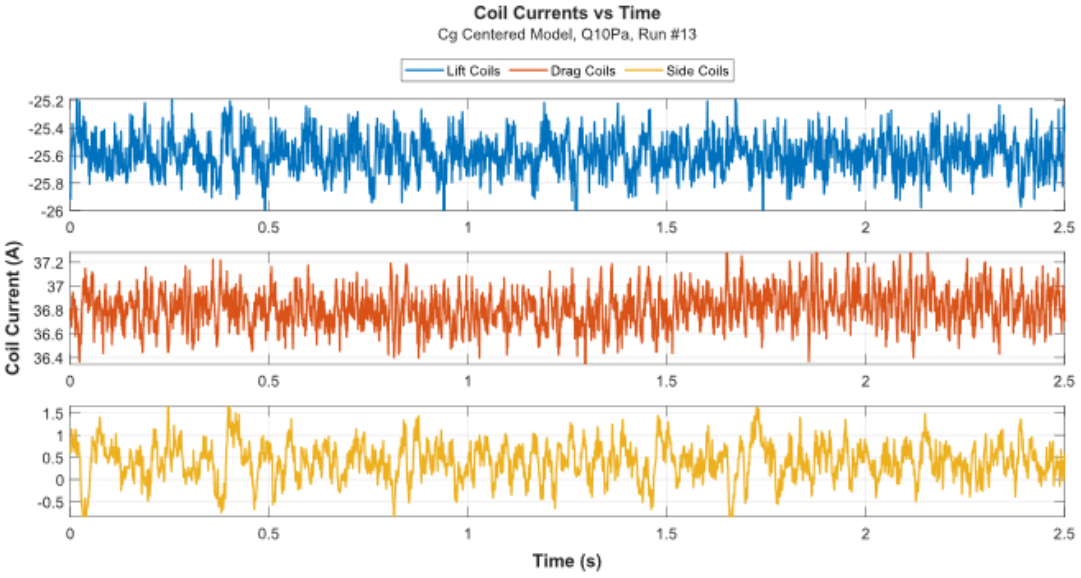

C.3.3 TUMBLING COMPONENT OF RUN, T = 2.5S - 8S

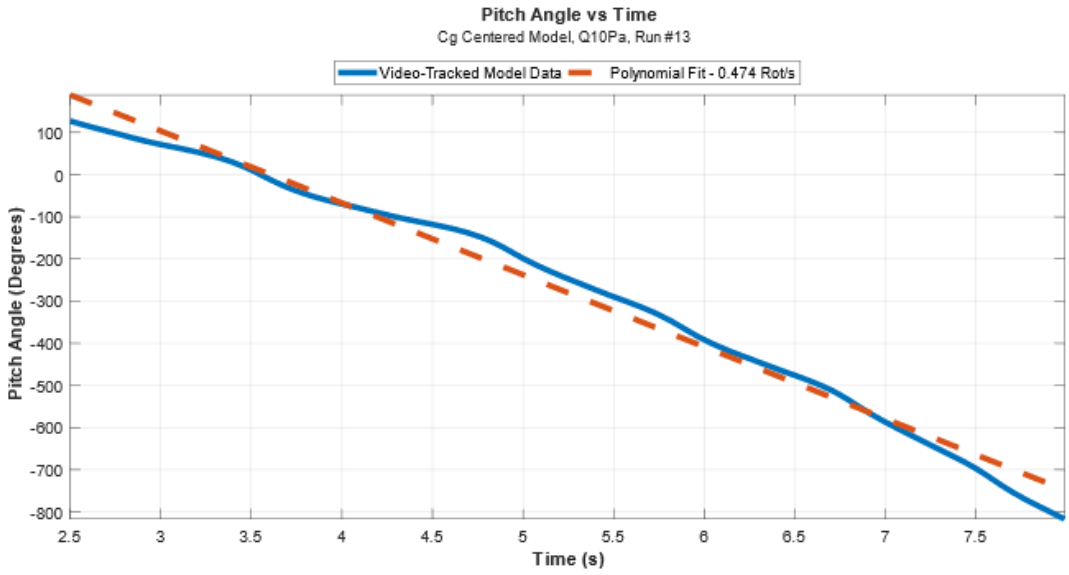

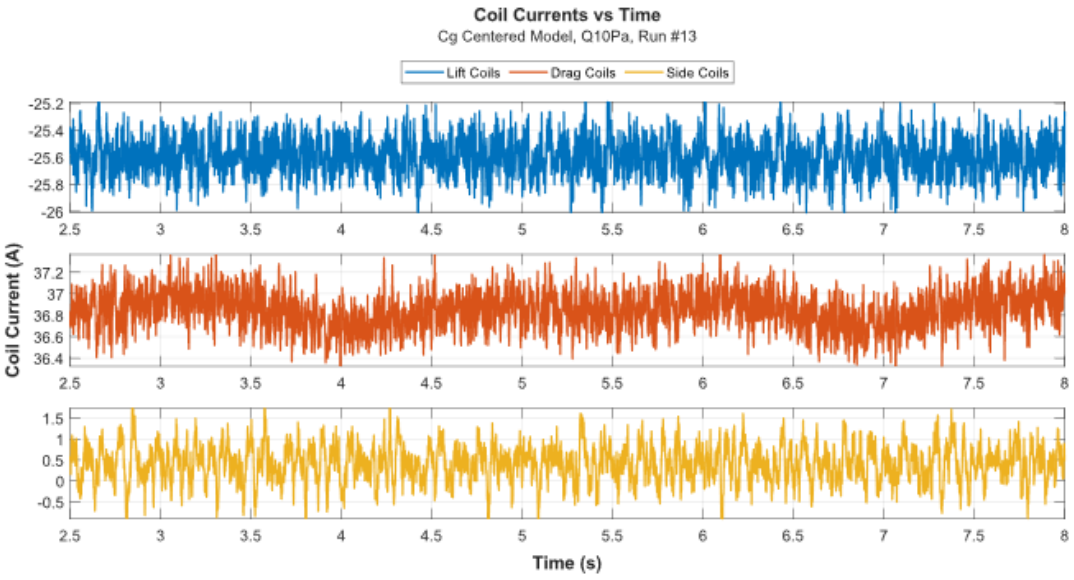

C.4 RUN14: Q = 10PA

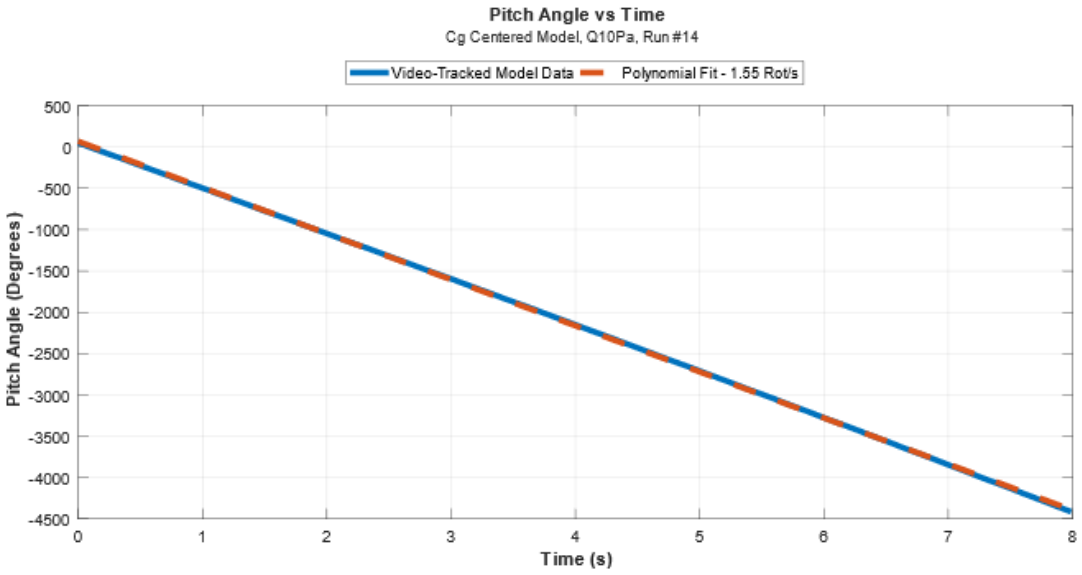

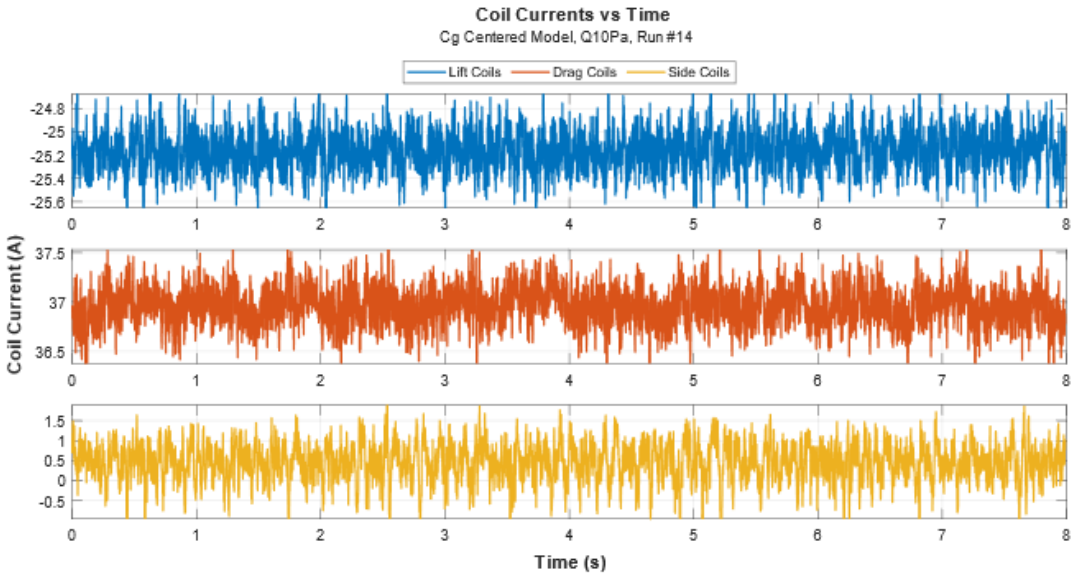

C.5 RUN15: Q = 10PA

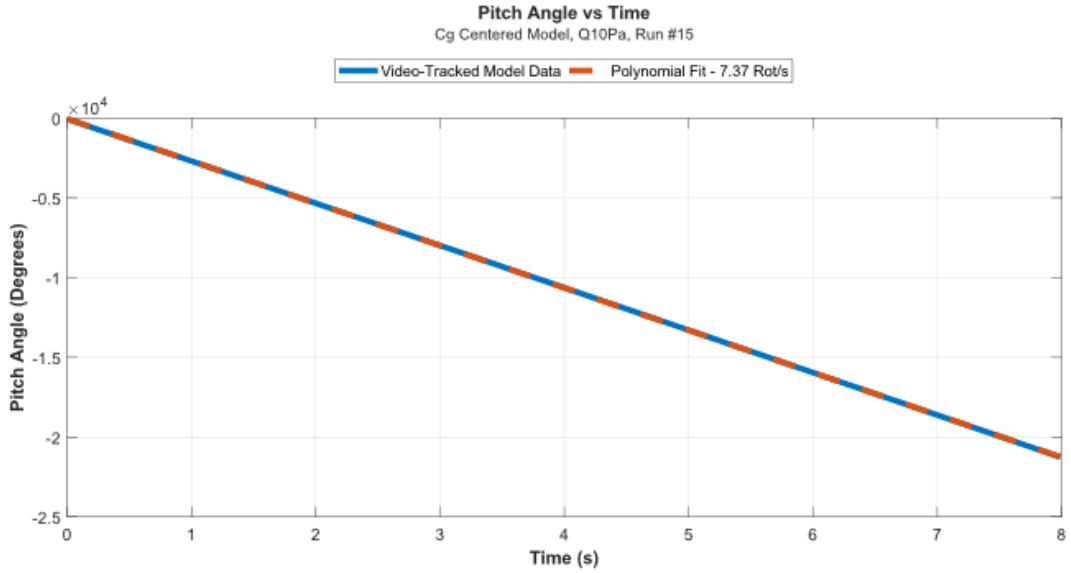

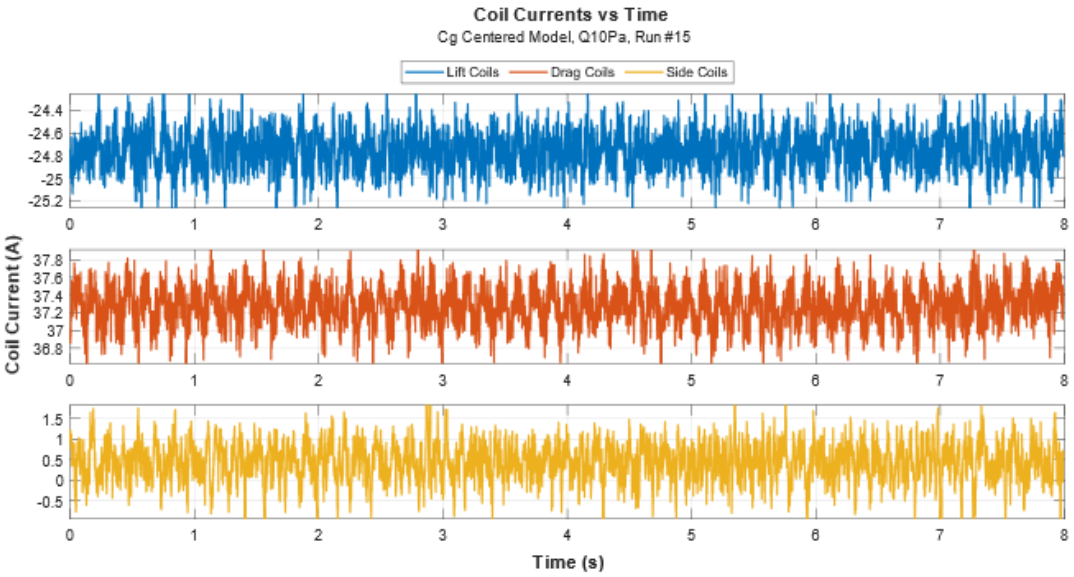

C.6 RUN16: Q = 10PA

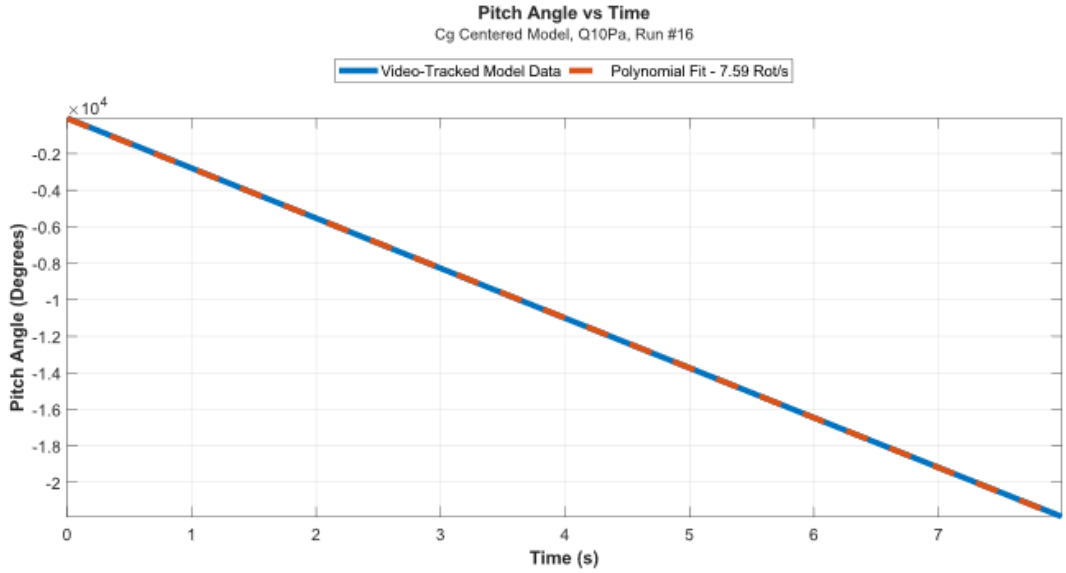

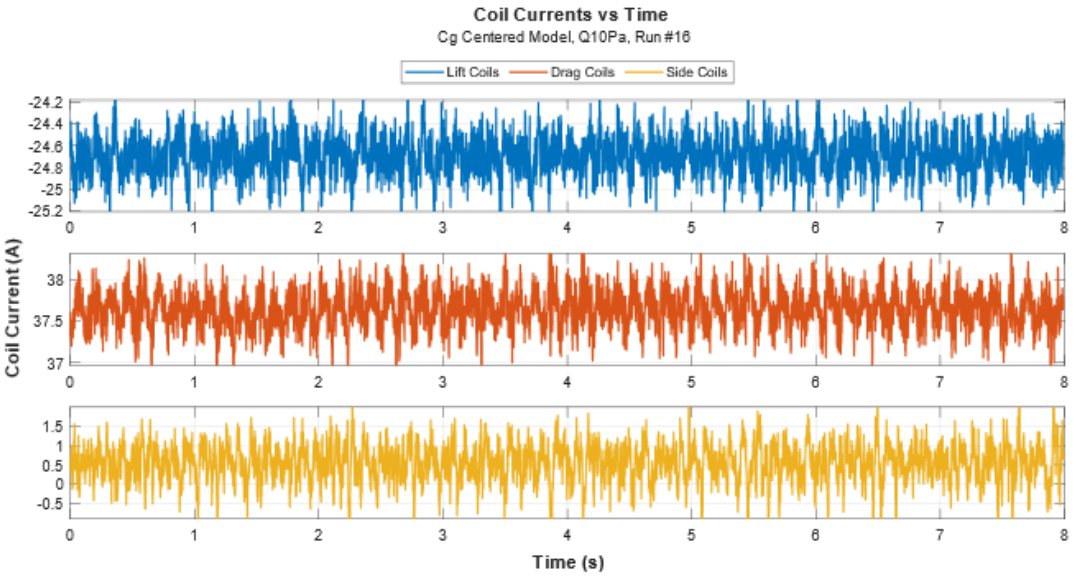

APPENDIX D

FULL RESULT COMPARISON

D.1 DRAG FORCE COEFFICIENT

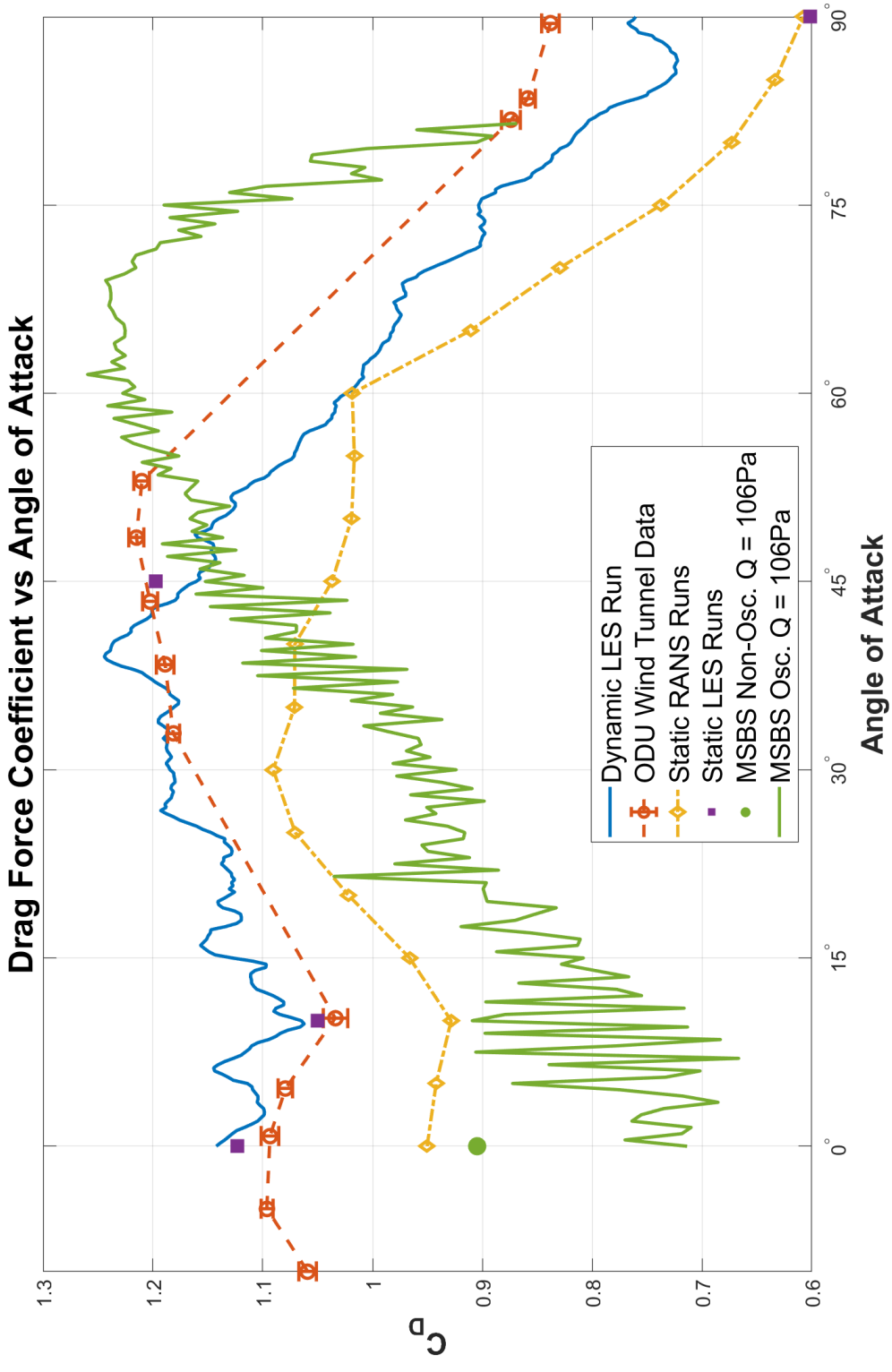

D.2 LIFT FORCE COEFFICIENT

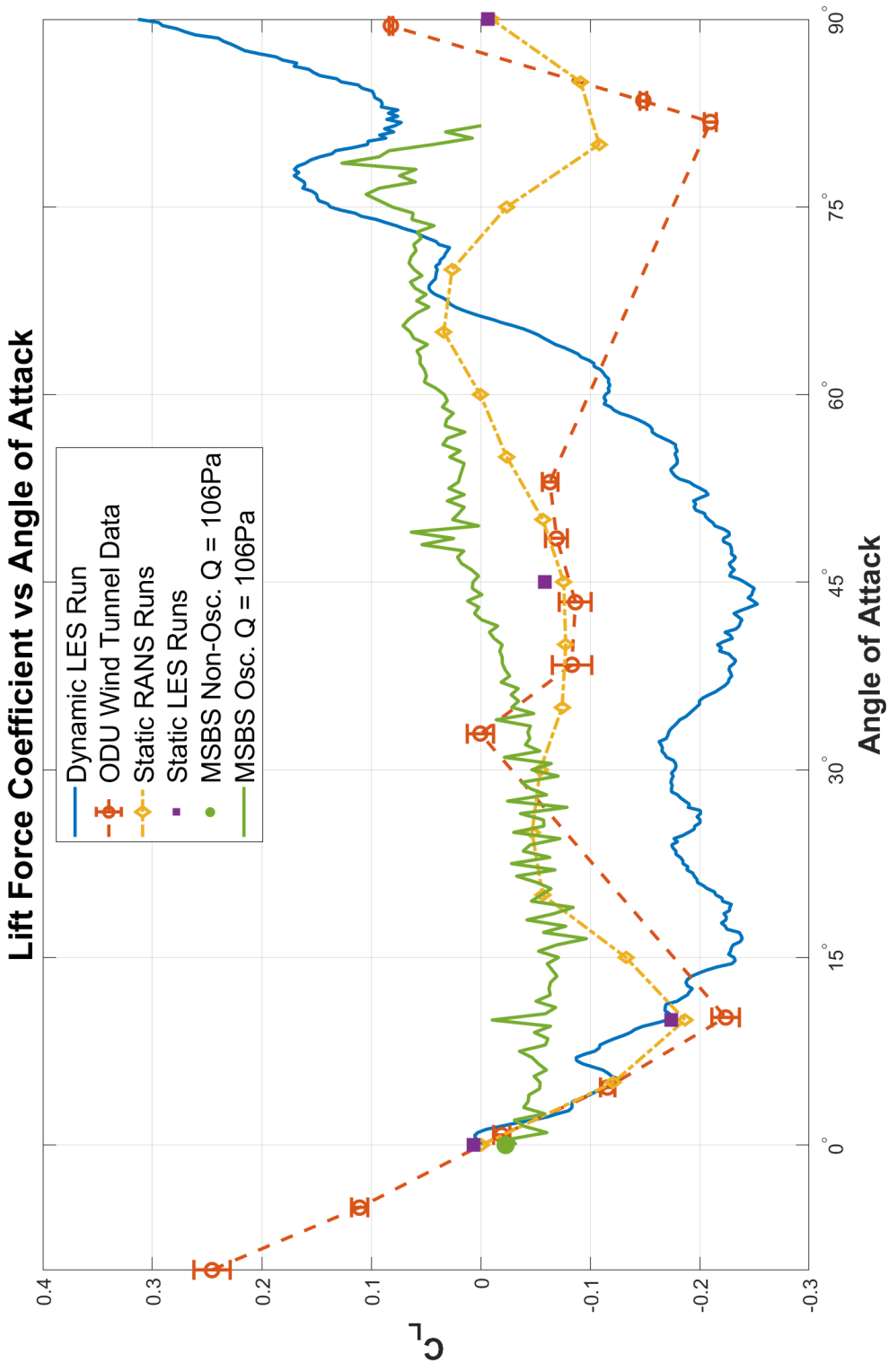

D.3 SIDE FORCE COEFFICIENT

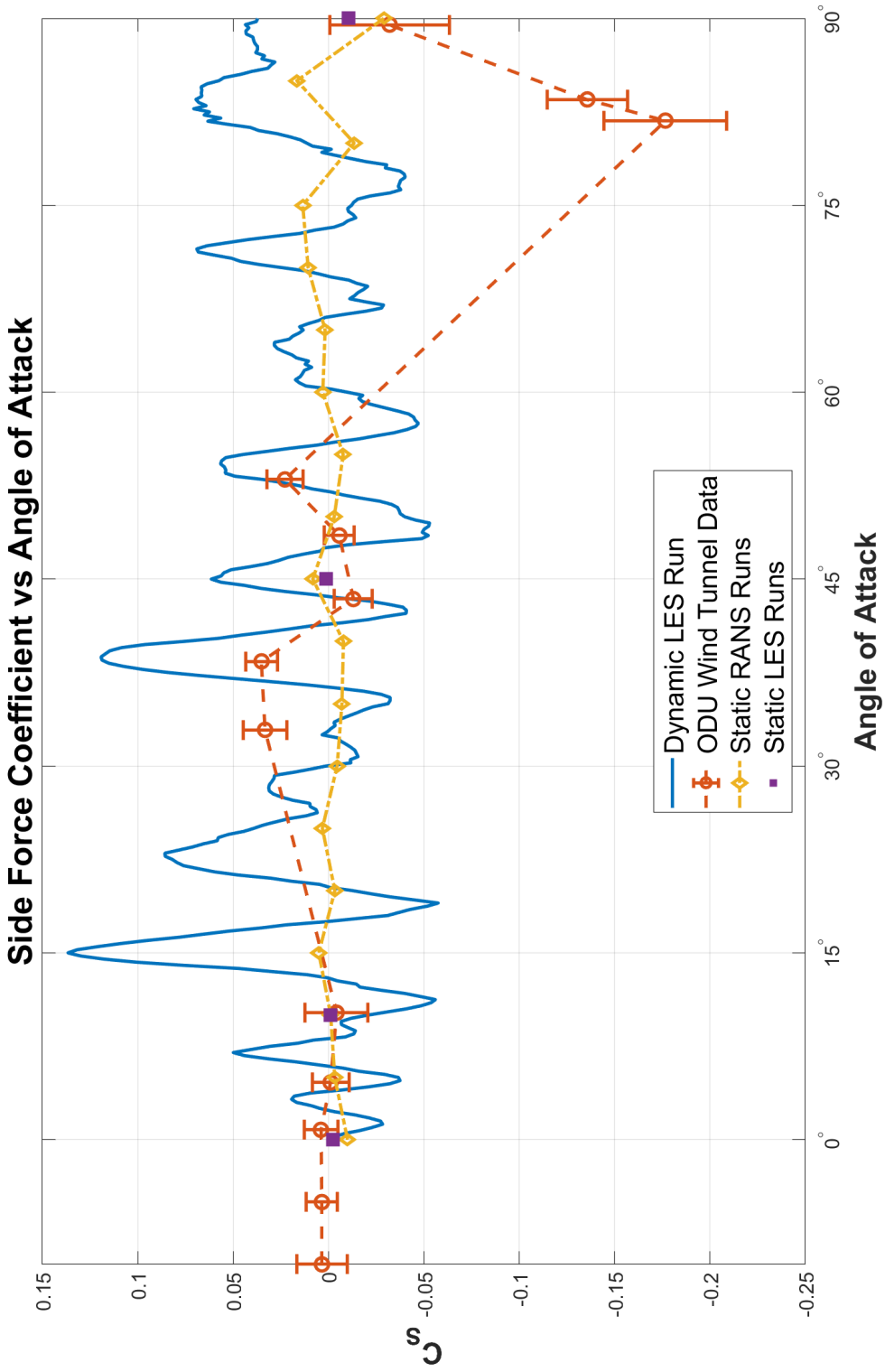

D.4 PITCHING MOMENT COEFFICIENT

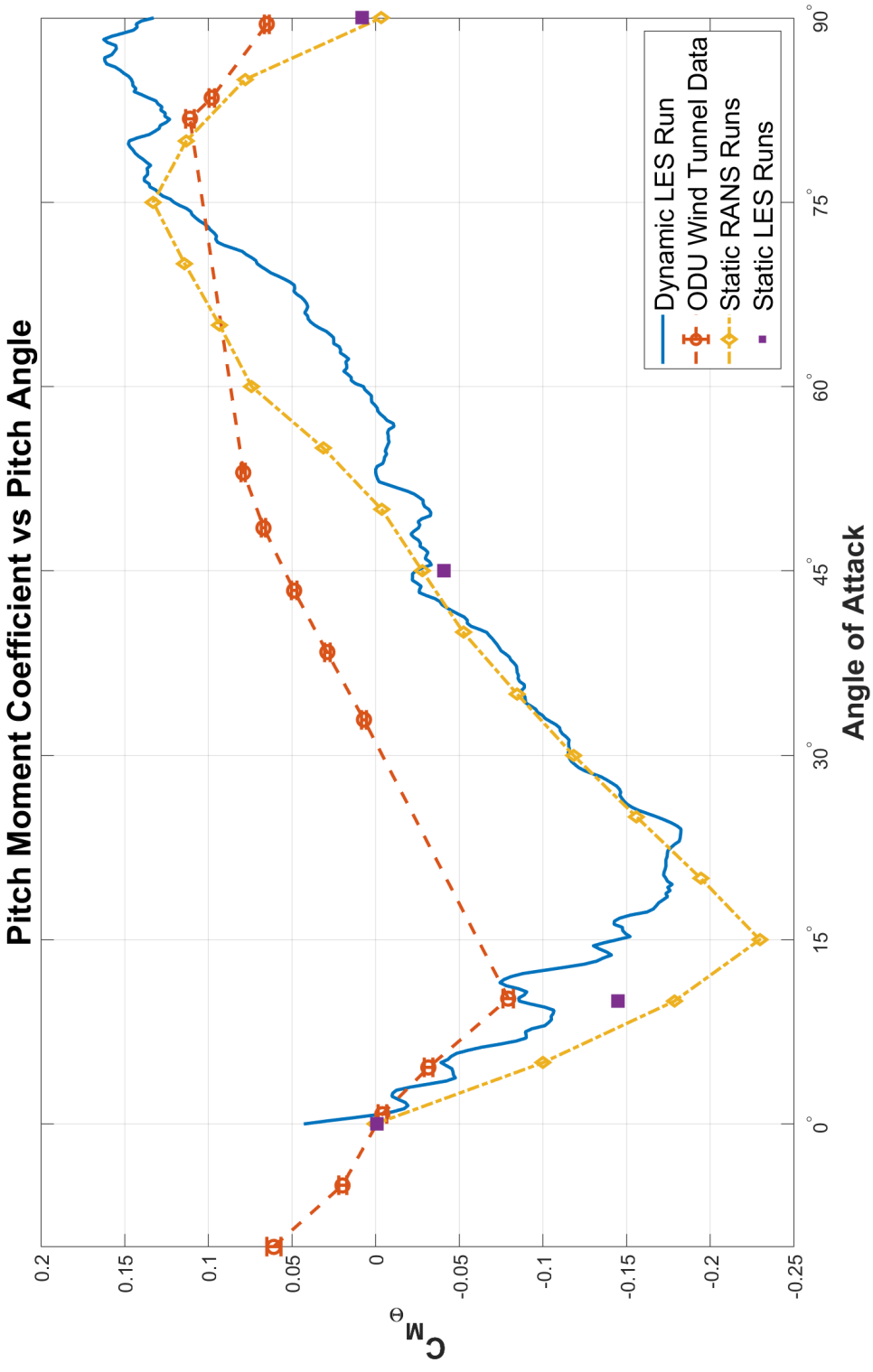

D.5 YAWING MOMENT COEFFICIENT

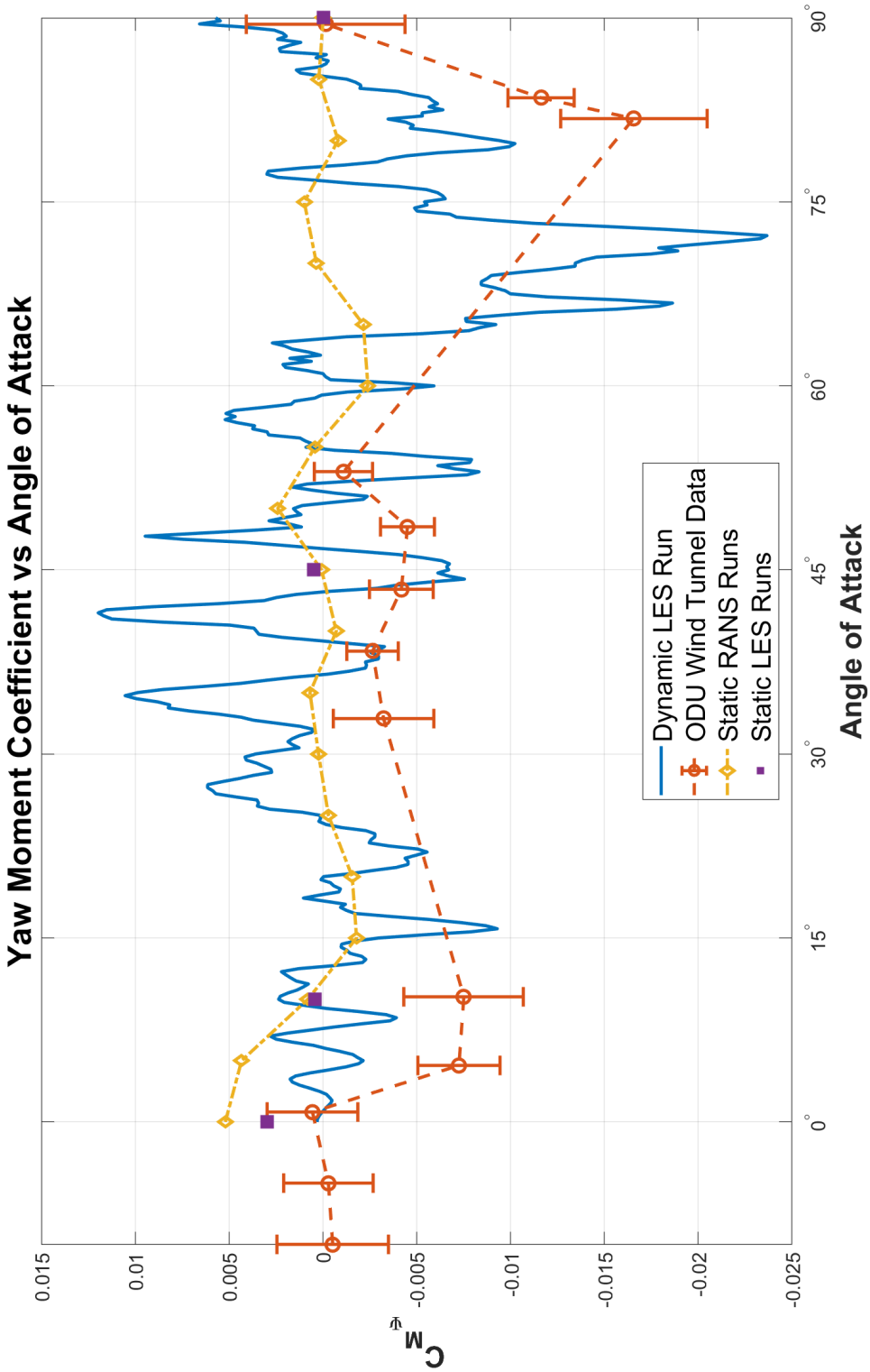

D.6 ROLLING MOMENT COEFFICIENT

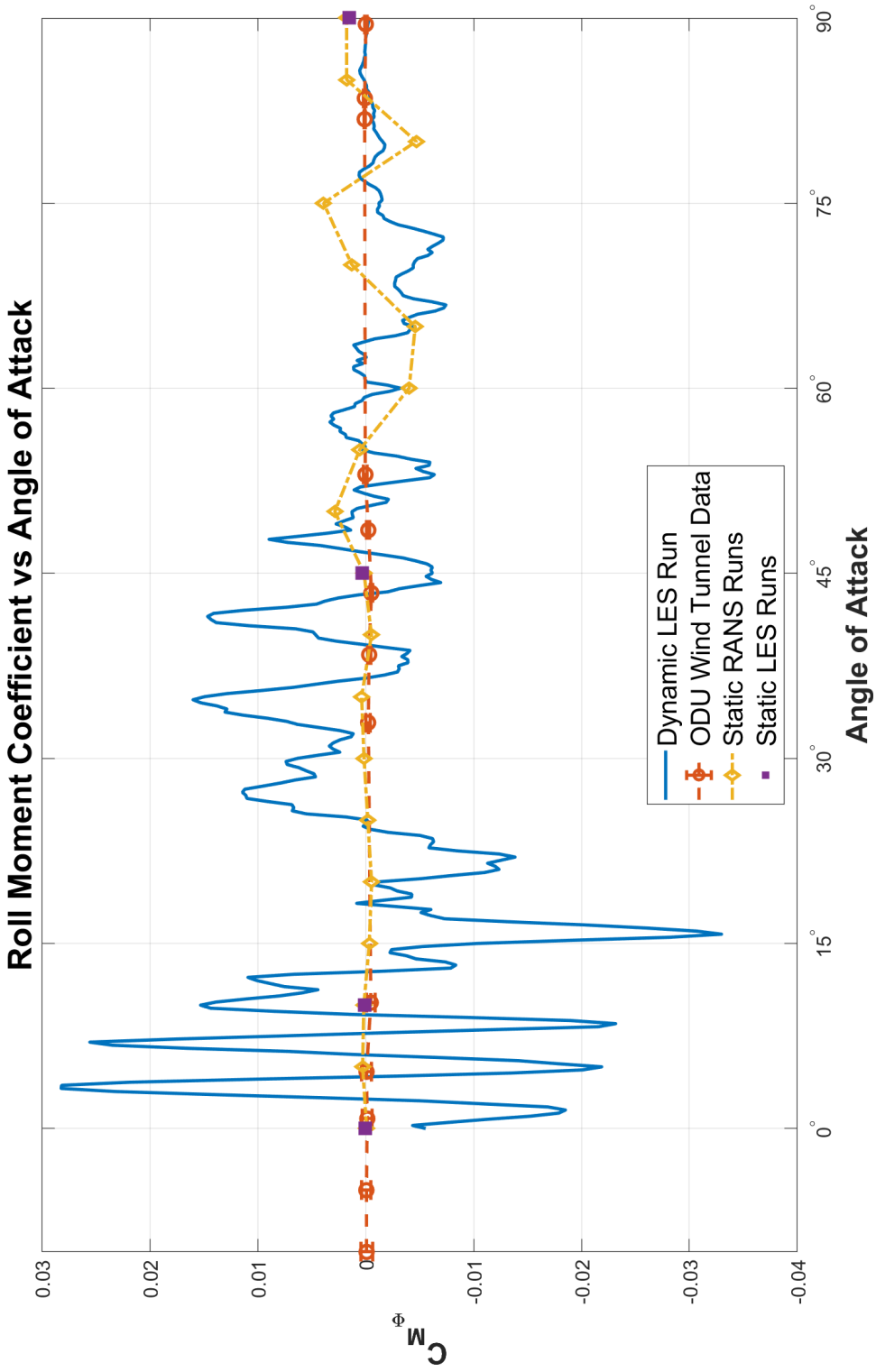

VITA

Forrest Miller
Department of Aerospace Engineering
Old Dominion University
Norfolk, VA 23529

EDUCATION

Master of Science: Aerospace Engineering August 2023 (Expected)
Old Dominion University, Norfolk, VA

Bachelor of Science: Physics August 2018
Old Dominion University, Norfolk, VA

Bachelor of Science: Mechanical Engineering August 2018
Old Dominion University, Norfolk, VA

SELECT PUBLICATIONS

2022 F. A. Miller and C. P. Britcher, "Effects of Separation Region Reattachment on the Dynamic Motion of Low-Fineness Ratio Cylinders," AIAA SciTech 2023 Forum, 23-27 January 2023, Washington, DC.

2021 F. A. Miller, "A Brief Update to the Aerodynamic Study of an Axially Oriented Low-Fineness Ratio Cylinder," International Conference on Flow Dynamics, 28 October 2021, online. Conference Presentation.

F. A. Miller, "Wake Structure Analysis of a Pitching Blunt Body Using Particle Image Velocimetry and Computational Fluid Dynamics," AIAA 2021 Region 1 Student Conference, 09 April 2021, online. Conference Presentation.

2020 F. A. Miller and C. P. Britcher, "Studies of Unsteady Aerodynamics of Axially Oriented Low Fineness Ratio Cylinders," International Conference on Flow Dynamics 2020, 28 October 2020, online. Conference Presentation.

F. A. Miller, "Computational Studies of Axially Oriented Low Fineness Ratio Cylinders," AIAA Young Professionals, Students, and Educators Conference, 15 October 2020, online.

PROFESSIONAL EXPERIENCE

Engineering Consultant November 2022 - Present
Miller Computational Services LLC Virginia Beach, VA

- Develops MATLAB based graphical user interface improvements based on client feedback and performance metrics.
- Leverages experience with numerical methods and algorithm development to assist engineers in designing solutions to image and signal processing problems in MATLAB.

Research and Development Team Lead April 2021 - November 2022

Antech Systems Incorporated Chesapeake, VA

- Utilized physics and aerospace background to approach innovative digital signal processing research effectively.
- Prepared a NASA Small Business Innovative Research Phase I grant proposal to acquire funding for proof-of-concept development of non-destructive testing methods, resulting in a 2022 award.
- Supervised a multi-disciplinary team in research, experimentation, and software development to meet grant goals and requirements.

UNDERGRADUATE PROJECTS

Physics Bachelor's Thesis August 2018

Topic: "MATLAB code for Spectrometer Calibration for Plasma Spectroscopy Applications"

Mechanical Engineering Bachelor's Capstone Project August 2017

Topic: "Model Jet Engine Afterburner Test Stand"

HONORS AND AWARDS

AIAA Region I Student Conference - Masters Division, 1st Place April 2021

AIAA Hampton Roads Section Service Award 2019-2020

AIAA National Section-Student Branch Partnership Award, 3rd Place 2019-2020

AIAA National Section-Student Branch Partnership Award, 3rd Place 2018-2019

EXTRACURRICULAR ACTIVITIES

ODU American Institute of Aeronautics and Astronautics, President 2019 - 2021

ODU American Society of Mechanical Engineers, President 2015 - 2017

ODU VEXU Robotics, Founding Member 2012 - 2018

CERTIFICATIONS

MathWorks Certified MATLAB Professional October 2022

MathWorks Certified MATLAB Associate June 2018

TECHNICAL SKILLS

Scripting Languages: MATLAB, Bash, Python

Programming Languages: R, C++, Wolfram

CAD Tools: Catia V5, AutoDesk Inventor

CFD Tools: scFLOW, SU2, OpenFOAM, Gmsh, Paraview, Tecplot

Other Tools: Simulink, Wolfram Mathematica, LabVIEW

Typeset using LaTeX.